

Master thesis

**Wobbe meter**

**A calorific measurement system on chip**

M.G. Pap

August 24, 2011

Faculty of Electrical Engineering,  
Mathematics and Computer Science  
Chair of Transducers Science and Technology

*Examination committee:*

Prof. dr. ir. G.J.M. Krijnen  
Dr. ir. R. Wiegerink  
Dr. ir. J.C. Lötters  
Ir. A.J. Mouris  
M.J. de Boer



---

# Contents

<b>Abstract</b>	<b>1</b>
<b>Nomenclature</b>	<b>3</b>
<b>1 Introduction</b>	<b>5</b>
<b>2 Calorific measurement methods</b>	<b>7</b>
2.1 Bomb calorimetry . . . . .	9
2.2 Combustion in an open flame . . . . .	9
2.3 Combustion on a catalyst . . . . .	10
2.4 Stoichiometric combustion . . . . .	11
2.5 Analytical methods . . . . .	11
2.6 Correlation methods . . . . .	11
2.7 Conclusion . . . . .	12
<b>3 Physics</b>	<b>13</b>
3.1 Thermodynamics . . . . .	13
3.1.1 Basics . . . . .	13
3.1.2 Dimensionless numbers . . . . .	14
3.2 Fluidics . . . . .	16
3.2.1 Gas kinetics . . . . .	16
3.2.2 Flows . . . . .	16
3.2.3 Combustion . . . . .	17
3.3 Mechanics . . . . .	20
3.4 Conclusion . . . . .	22
<b>4 Design</b>	<b>23</b>
4.1 Bio-gas . . . . .	24
4.2 Fluidics . . . . .	26
4.2.1 Mixers . . . . .	27
4.2.2 Network model . . . . .	31
4.3 Heaters . . . . .	35
4.3.1 Heat transfer . . . . .	35
4.3.2 Electrical heating . . . . .	37
4.4 Core . . . . .	39
4.4.1 Mechanics . . . . .	41
4.4.2 Thermal loss . . . . .	42
4.4.3 Temperature measurement . . . . .	44
4.5 Process flow . . . . .	45
4.6 Mask design . . . . .	50
4.7 Conclusion . . . . .	54

---

<b>5</b>	<b>Fabrication</b>	<b>57</b>
5.1	Masks . . . . .	57
5.2	SiRN deposition . . . . .	57
5.3	Access-holes . . . . .	58
5.4	Channels . . . . .	60
5.5	Core by KOH etching . . . . .	62
5.5.1	MX5020 Lithography . . . . .	62
5.5.2	SiRN etching . . . . .	64
5.5.3	KOH pit . . . . .	66
5.6	Platinum on SiRN . . . . .	67
5.7	Release etch . . . . .	68
5.8	Conclusion . . . . .	68
<b>6</b>	<b>Measurement set-up</b>	<b>73</b>
6.1	Set-up . . . . .	73
6.2	Measurement protocol . . . . .	74
6.3	Conclusion . . . . .	77
<b>7</b>	<b>Conclusion</b>	<b>79</b>
<b>8</b>	<b>Recommendations</b>	<b>81</b>
<b>Appendices</b>		
<b>A</b>	<b>Material properties</b>	<b>85</b>
<b>B</b>	<b>Clewin scripts</b>	<b>87</b>
<b>C</b>	<b>Processing</b>	<b>95</b>
C.1	Process flow . . . . .	95
C.2	Wafer allocation . . . . .	106
<b>D</b>	<b>Set-up blueprints</b>	<b>109</b>
<b>Bibliography</b>		<b>116</b>



---

# Abstract

With help of MEMS technology a new approach was created for the realization of an on-chip Wobbe-index metering solution. The use of MEMS technology for a metering solution gives a reduction in size and costs which can be a huge benefit for the (bio-)gas industry. The metering solution requires the integration of two devices: the micro-coriolis flow sensor and a calorific measurement sensor. The goal of this project was to do a feasibility study for a proof-of-concept of an on-chip calorific sensor which can be integrated with the existing micro-coriolis flow sensor. There were two chips designed with in total seven variations to study the behaviour of combustion inside the chip. A measurement set-up was realized which provides a flexible test-environment for the characterisation of the chip. The project delivered two new process flows: using Dupont MX5020 polymer foil for lithography on structured surfaces and applying platinum on silicon-rich nitride without an adhesion layer for high temperature micro-heaters. All the problems which were encountered during the processing were solvable and led to alternative solutions for future processing. The production in the cleanroom was not finished due to time constraints and unforeseen circumstances which did not enable us to characterize the calorific sensor. Creating a calorific sensor is deemed feasible and with the developed process-flow an integration can be realized of the calorific sensor and the micro-coriolis sensor into one device: the wobbe-meter.



# Nomenclature

Symbol	unit	description
$A$	$m^2$	area
$\alpha_R$	$1/K$	thermal expansion coefficient of resistance
$\alpha_L$	$1/K$	linear thermal expansion coefficient
$\alpha_V$	$1/K$	volume thermal expansion coefficient
$\beta$	$1/K$	volumetric expansion coefficient ( $1/T$ )
$C_p$	$J/kg \cdot K$	thermal capacity at constant pressure
$C_v$	$J/kg \cdot K$	thermal capacity at constant volume
$D$	$m^2/s$	diffusion coefficient
$E$	GPa	Young's modulus
$\frac{\epsilon}{\kappa}$	K	potential parameter
$\epsilon$	-	surface emissivity
$g$	$m/s^2$	gravitational force
$h$	$W/m^2 \cdot K$	thermal transfer coefficient
$I$	$m^4$	Second moment of inertia
$k$	$W/m \cdot K$	thermal conductivity ( $k_f$ = fluid, $k_b$ = bulk)
$L$	$m$	characteristic length/ hydraulic diameter ( $L = \frac{V}{A}$ )
$\mu$	$Pa \cdot s$	dynamic viscosity
$\nu$	$m^2/s$	kinematic viscosity
$p$	Pa	pressure
$Q$	W	thermal flux
$\rho$	$kg/m^3$	density
$R$	$J/mol \cdot K$	universal gas constant (8.314,4621)
$S$	$J/K$	entropy
$\bar{\sigma}$	Å	collision diameter in Angström
$\sigma$	$W/m^2 \cdot K^4$	Stefan Boltzmann constant ( $5.670400 \cdot 10^{-8}$ )
$r$	$m$	radius
$Tq$	$N \cdot m$	torque
$T$	K	temperature in degree Kelvin
$T_{inf}$	K	the ambient temperature far away from the surface
$T^*$	$\frac{\kappa T}{\epsilon}$	reduced temperature
$\tau$	$N/m^2$	torsion stress
$\vec{v}$	$m/s$	flow speed
$V$	$m^3$	volume
$\varphi_V$	$m^3/s$	volumetric flow
$W$	$g/mol$	mean molar weight
$W_k$	$g/mol$	molar weight of species $k$
$x$	$m$	distance
$\Omega^{(i,j)}$	-	collision integral

Table 1: Symbols and constants



# Chapter 1

## Introduction

The world runs on energy and most of it is provided by combustion of fuels such as oil and gas. The measurement of the energy content in fuel is done by determination of its calorific value. The first measurement method for obtaining the calorific value of fuel sources was developed in 1760 by Black [1]. Over time many different methods [1, 2] were developed for determining the calorific value in solid/liquid/gaseous fuels but accurate measuring of gaseous fuels was always the hardest to achieve. In 1927, Goffredo Wobbe, a physicist in Bologna, Italy, came up with a method to compare natural fuel gasses with each other with a unified scale: the 'Wobbe-index'. Since then it became a standard in the industry to work with the Wobbe-index for comparison of the calorific value of gaseous fuels.

The calorific value of natural fuel gasses is important for the industry as the composition of the gas fluctuates with the source. The natural gas delivered from the distribution networks can vary in its energy content as the networks are interconnected across country borders. The natural gas from Russia differs from the Dutch gas in composition as the amount of alkanes (methane, ethane, propane, etc.), nitrogen and carbon dioxide is different per location.

The fluctuation in the composition of natural gasses asks for a method which accurately determines the calorific value and the delivered flow for the billing of the costs per unit of energy and not per cubic meter of unknown gas. For this purpose calorimeters are used which accurately measure the gas and relate it to the calorific value or the Wobbe-index. The Wobbe-index is a measure for the interchangeability of gas mixtures: a constant Wobbe-index of the fuel gas ensures that at combustion the energy flow of the fuel gas is constant at a constant pressure. In the Netherlands the Wobbe-index is maintaining between the 43.46-44.41 MJ/nM<sup>3</sup> for fuel gasses supplied by the network, this is done by blending of streams of various gas sources.

There are a wide variety of systems on the market but on average they have the size of a medicine cabinet and a price around €25,000. An example of a Wobbe-index measurement system is shown in figure 1.1.



Figure 1.1: An example of an industrial Wobbe-meter by Hobre Instruments b.v.[3]

Nowadays even farmers produce their own bio-gas [4] by fermentation of manure or agricultural waste. Most farmers use it as local energy supply but the bio-gas can also be supplied back to the gas-distribution network or can be converted on location to electrical energy for distribution to the electrical network. The operators of the gas distribution grids have strict admission criteria [5] for supplying of biogas to the grid. The Wobbe-index should be within the range of 43.46-44.41 MJ/nM<sup>3</sup> and must be monitored continuously. For small-scale bio-gas projects this means investment costs for analytical equipment which are excessive in comparison with the costs for the bio-gas production and purifications systems. These large investments form a high threshold for the small-scale bio-gas industry.

Over the years no real improvements were achieved on the terrain of calorimetry of gaseous fuels but with help of the MEMS (Micro Electro Mechanical Structures) domain a new approach can be taken for an on-chip Wobbe-index metering solution. Implementation of calorimetry on the MEMS-scale would given a reduction in size and costs which can be a huge benefit for the (bio-)gas industry. An on-chip implementation would require measuring of the calorific value, mass flow and the relative density. There is already an on-chip solution for measurement of the relative density and the mass flow within the department of Transducer Science and Technology (TST) at the University of Twente: the micro-coriolis flow sensor [6]. The goal of this project is to do a feasibility study for a proof-of-concept of an on-chip calorific sensor which can be integrated with the micro-coriolis flow sensor. The result of this integration gives a sensor with which the Wobbe-index of a gas can be measured.

In this thesis we will discuss the development of the calorific sensor which is done in the following layout of the thesis:

In chapter 2 the origin and the basics of calorific determination are described. Furthermore an overview is given of the conventional calorific measurement methods that are available.

In chapter 3 the physics will be presented that are used for the designing of the calorific sensor.

In chapter 4 the design of the calorific sensor is created with the specifics of the fluidic heaters, thermal losses, mixing structures, the cleanroom process flow and the masking plates.

In chapter 5 the details of the fabrication steps of processing in the cleanroom are discussed.

In chapter 6 the designed measurement set-up and measurement protocol will be discussed.

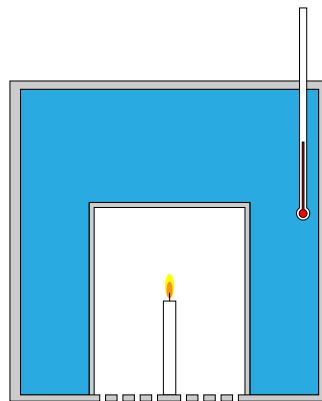
In chapter 7 the conclusions are given and the thesis is concluded with in chapter 8 some recommendations for future work.

## Chapter 2

# Calorific measurement methods

This chapter will give a summary of the different methods which are used to determine the calorific value of fuels [2]. These methods can be separated in a direct and indirect methods where the direct method measures the flow of energy and the indirect method the composition of the fuel which relates it to pre-measured calorific values. For determination of the Wobbe-index for industrial purposes ISO standards were developed: ISO6976 [7] and ISO15971 [8]. These ISO standards standardize not only the measurement (ISO6974) and calculation (ISO6976) methods but also the measurement conditions like the fuel temperature and pressure. For the metric system the standard temperature is defined at 0°C, 5°C, 10°C, 15°C, 20°C or 25°C at a pressure of 1013.25 mBar.

The basic method of measuring the calorific value of a combustion is measuring the temperature increase of a material that absorbed the energy of the combustion. A simple set-up for measurement of the calorific value is shown in figure 2.1. The burning candle is the energy source which heats the water that surrounds the compartment of the candle. With a thermometer we can measure the temperature of the water. The water has a thermal capacity ( $C_p$ ) with a given mass ( $\rho \cdot V$ ) and with the begin and end temperature the thermal energy flux ( $Q$ ) that was released during the combustion can be calculated with equation 2.1. Measurement system are insulated to minimize the heat flux from the water to the outside world as this influences the accuracy of the measured calorific value.

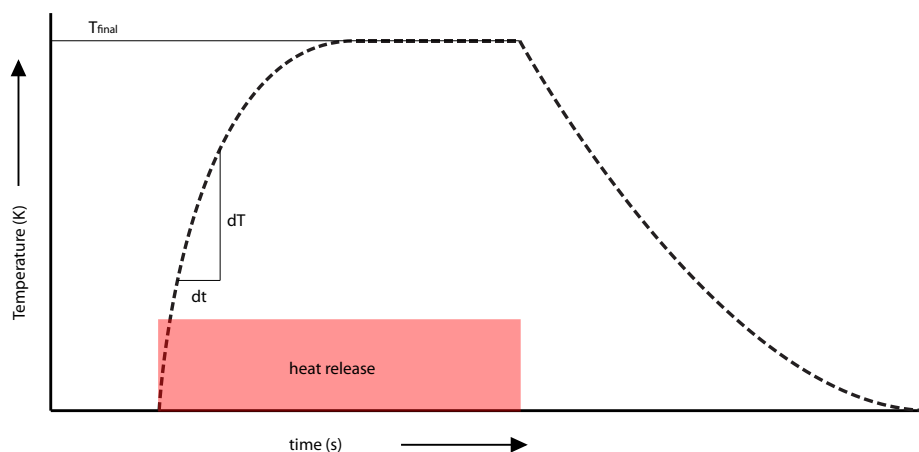


**Figure 2.1:** A simple calorific energy measurement method. The temperature rise of the water gives the energy released by burning of the candle.

$$\frac{dT}{dt} = \frac{Q}{\rho \cdot V \cdot C_p} [K/s] \quad (2.1)$$

Another measurement method is measuring the energy release within a timeslot which gives the

energy per time instance. This method is faster as the former method as the temperature in the measurement medium increases with  $1 - \exp^{-Q \cdot t}$ . The exact end temperature is reached at the moment that the temperature drops again. The energy per time instance is limited to the sampling resolution and sample time but gives also extra information about the reaction kinetics which takes place during combustion. Both methods are graphically shown in figure 2.2.



**Figure 2.2:** Measurement of the combustion energy by measurement of the final temperature  $T_{final}$  or by sampling the energy flow  $\frac{dT}{dt}$ .

There are two underlying principles for measuring with a calorimeter [1]: measurement of the heat exchanged by compensation of a temperature change and measurement of the heat exchanged by measurement of a temperature difference.

Compensation of the temperature change can be done by:

- phase transition and measurement of the mass of the reacted substance: uses the latent energy of the transition from solid to fluid or fluid to gas,  $Q = C_t \cdot \Delta m$  where  $C_t$  = the specific heat of transition and  $\Delta m$  the measured mass difference.
- electrical heating (Joule effect) or cooling (Peltier effect) and measuring of the electrical energy:  $\int U(t) \cdot I(t) dt = C \cdot \Delta m$  where  $C$  = the specific heat of solution,  $\Delta m$  the measured mass difference and  $U(t) \cdot I(t)$  the electrical power.
- chemical heat of a known reaction: heat is added through a chemical reaction to achieve an equilibrium,  $C_{sample} \cdot \Delta m_{sample} = C_{calorimeter} \cdot \Delta m_{calorimeter}$  where  $C$  = the specific heat of reaction and  $\Delta m$  the measured mass difference.

The measurement of the temperature difference can be done by:

- measuring a time-dependent temperature difference and a heat capacity:  $c_{sample} \cdot (T_{initial} - T_{final}) = c_{calorimeter} \cdot (T_{final} - T_{initial})$
- measuring a local temperature difference and a calibration factor: simultaneous measurement of the temperature at two positions,  $C_{reaction} \cdot \Delta m_{reacted} = K \cdot \Delta T$  or  $Q_{generated} = K(T) \cdot \int \Delta T(t) dt$  where  $K$  = the calibration factor.

There are a variety of measurement set-ups available which use these principles for determination of the calorific-value. In the coming sections some examples of these measurement set-ups will be discussed.



## 2.1 Bomb calorimetry

In bomb calorimetry (figure 2.3) a caloric bomb is used as measurement device. The caloric bomb is composed of a cylindrical or spherical shell with within it the fuel, oxygen and ignition device. The bomb or vessel is thermally isolated from the surrounding environment by means of a water or polystyrene jacket with an air-gap in between to reduce the heat conductivity. The temperature rise as result of the combustion is proportional to the calorific value. The temperature can be measured by means of the conventional way or the dry way [9]. In the conventional way the wall of the bomb is in contact with a water shell of which the temperature is measured, the exact volume of water and the container are part of the effective thermal capacity. The dry way uses a high thermal conductive aluminium jacket which is shrunk under high-pressure over the vessel where between the layers temperature sensors are placed. This jacket has a constant thermal capacity in comparison with the water jacket as the water volume can vary due to evaporation.

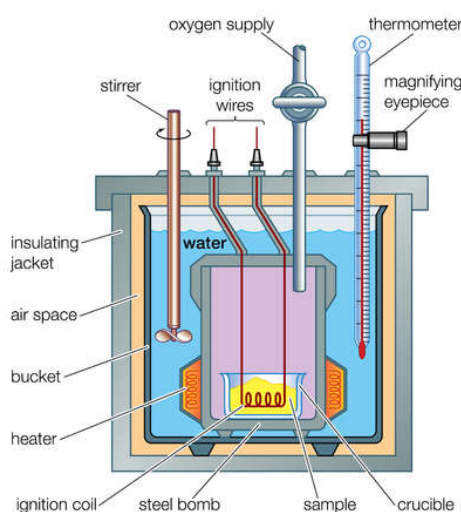


Figure 2.3: A schematic sketch of a bomb calorimeter [10]

Solid fuels are placed in the middle of the bomb where the fuel burns at the contact area with the oxygen after ignition. The energy of the burning keeps the reaction going on. Gaseous fuels are mixed in the vessel and on ignition a thermal wave expands from the centre outwards. As the gas is cooler at the interface with the wall the combustion energy has to overcome this. In case of a too steep thermal gradient an incomplete combustion will occur which is called quenching. The process of combustion in a bomb calorimeter is isochoric (constant volume) and isoperibolic (near-isothermal).

## 2.2 Combustion in an open flame

The combustion of fuel in an open flame (figure 2.4) is the oldest principle in the field of calorimetry. A specific amount of fuel and air is fed to a burner which delivers the energy for the combustion. Combustion with too much air will result in heating the surplus air which results in a lower combustion temperature. A too lean mixture will result in an incomplete combustion with at the exhaust combustion radicals like CO or fuel. The heat that is released is absorbed in the thermal capacity of the water jacket which acts as heat exchanger with the combustion chamber. The temperature rise in the water jacket gives measure for the thermal energy of the fuel which has to be corrected for the energy of the open flame. The process of combustion in an open flame is isobaric (constant pressure) and isothermal.

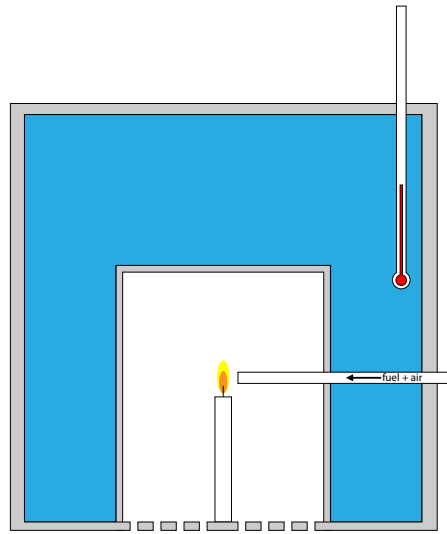


Figure 2.4: A schematic sketch of an open flame calorimeter.

Another implementation of burning fuel in an open flame is by creating a heat balance [11]. The fuel is fed to a burner which is located in a heat pipe, additional to the burner an electrical element is also used for extra heating. The pipe is cooled by means of a Peltier-element so that the temperature which is measured at top of the heat pipe is regulated to a constant value. A high calorific fuel needs less electrical heating for a constant temperature than a low calorific fuel. The amount of power fed to the electrical heater is the measure for the calorific value.

## 2.3 Combustion on a catalyst

The reaction between gaseous fuel and oxygen can also be done at low temperatures by oxidation on a catalyst which is shown in figure 2.5. The resulting heat from the reaction heats the catalyst which can be taken as measure for the calorific value. The catalyst needs to be on an optimal temperature for the reaction, this can be achieved by using an electrical heater and measuring the energy balance to keep the temperature constant. The relation between the temperature and the electrical power can be used for the derivation of the calorific value. The most common used catalytic materials are: platinum, nickeloxide and alumina or calcium/magnesium aluminates [12]. The catalyst can be in form of a porous medium which is deposited in the flow channel or in the form of catalytic pellets which are inserted as a packed bed inside a capillary. This process is isobaric and isothermal.

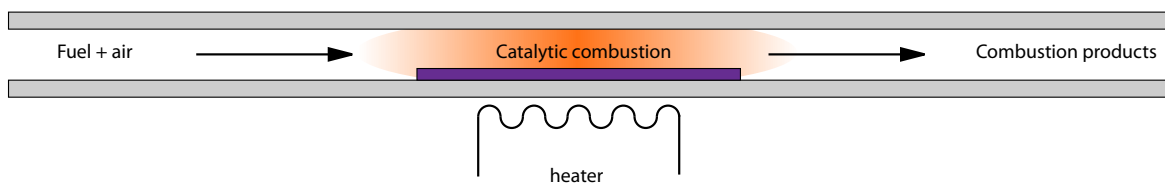


Figure 2.5: A schematic sketch of a catalytic calorimeter.

## 2.4 Stoichiometric combustion

Stoichiometric combustion or theoretical combustion is the ideal combustion process where the fuel is burned completely, a sketch is shown in figure 2.6. The ratio of fuel/air that is needed for the combustion is regulated where the excess oxygen or excess fuel vapour is measured with a zirconiumoxide Nernst cell which is also called a lambda probe. The resulting ratio of fuel/air, also named the CARI (combustion Air Requirement Index), that is needed for the combustion can be linear related to the Wobbe-index. This process is isobaric and isothermal.

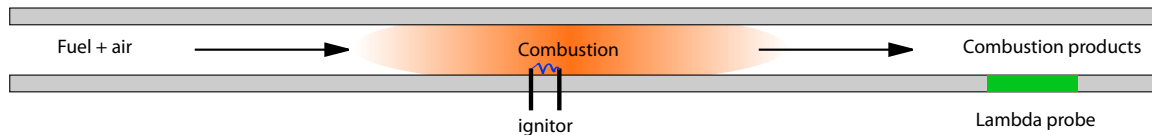


Figure 2.6: A schematic sketch of a stoichiometric calorimeter.

## 2.5 Analytical methods

The indirect methods analyse the composition of the gas and extrapolates the calorific value. The analysis can be done with gas-chromatography (figure 2.7) where the composition of the fuel is measured by separating the gas into individual components in a separation capillary. As each component of the gas has its own travel speed through the separation capillary it will arrive at different times at the exit where the concentration is measured with spectrography or thermal conductivity. The travel speed is distinct for the component and with the determined concentration the calorific value can be calculated from a reference table like the one which is supplied in the ISO6976 standard [7]. The summation over the reference values of all measured components gives the calorific value of the gas.

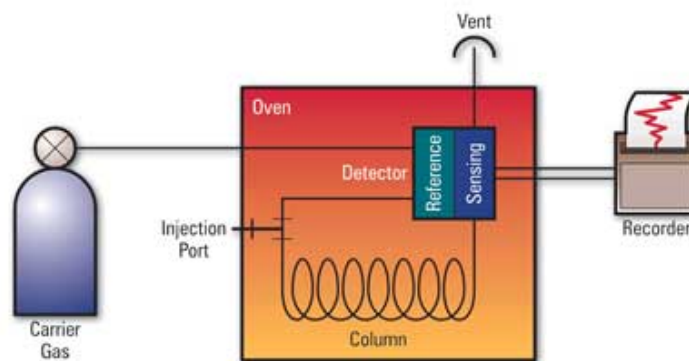


Figure 2.7: The composition of a gas can be determined by means of gas-chromatography. The heating value of the gas is calculated out of reference tables.[13]

## 2.6 Correlation methods

Another indirect method is determination by correlating the physical parameters of the fuel with reference calorific values. There are many physical parameters that can be used to derive the correlation such as:

- Viscosity and/or pressure and/or density [14, 15, 16, 17, 18, 19, 20, 21]
- The velocity of sound [15, 22, 23, 19, 24, 25, 26, 27, 28]
- Neutron/radiation absorbance, spectral scattering of CO<sub>2</sub> and N<sub>2</sub> or flame ionization detection [29, 30, 27, 28]
- Thermal capacity at constant volume/pressure ( $C_v/C_p$ ) or thermal conductivity [31, 32, 33, 34, 35, 25, 30, 27, 36, 37]
- Relative permittivity [28]

The first four parameters are temperature dependent so variation in temperature would give an extra correlation factor. The correlation is found by means of regression analysis between the found values and the reference. The downside of this method is that the composition of the gas cannot be an unknown, only the concentration of the components may vary. The upside of this method is that there is no combustion and the fraction of gas which is sampled can be returned in the pipeline.

## 2.7 Conclusion

From the above described methods is chosen for an adjusted combustion in an open flame. This method is the easiest to integrate with the already existing micro-coriolis technology and gives a direct relation between the combustion energy and the measured temperature. The open flame is replaced by electrical pre-heating of the gas to obtain auto-ignition. The measurements will be preformed with a continuous flow of gas where the end temperature of the chip will be a measure for the thermal balance between the combustion energy of the gas and the thermal losses of the chip.

## Chapter 3

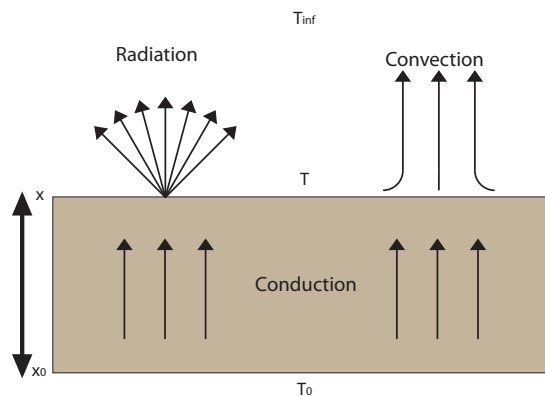
# Physics

In this chapter we will present the physical models which form the tools for calculating the thermodynamic, fluidic and mechanical properties of the design which will be presented in chapter 4.

### 3.1 Thermodynamics

#### 3.1.1 Basics

There are three basic principles in the domain of thermodynamics for heat transfer in solids and fluids: conduction, convection and radiation, these are shown in figure 3.1.



**Figure 3.1:** The heat transfer through a medium with conduction and from the medium by radiation and free convection.

Conduction happens due to the transfer of kinetic energy between the interfaces of the atoms or molecules with their neighbouring atoms or molecules. The density of a material relates to the conductive property of the material, a more dense material like a metal conducts heat better than a not so dense material like air. The heat conduction can be described by equation 3.1.

Convection is caused by movement of fluids and gasses along a surface. Heating of the fluid or gas at the surface causes a change in the temperature of the gas which causes a variation in the density according to the gas-law. In the case of natural convection the change of density causes the hot gas/liquid to rise. Next to natural convection there is also forced convection which consists of fluids and gasses passing forced along a heated surface. The convective heat transfer along a surface can be described in linear situations by equation 3.2.

Radiation is the emission of electromagnetic waves (photons) in the infra-red region of the spectrum. Every object emits radiation due to the random movement of the atoms but it becomes a more dominant factor in heat transfer as the temperature rises. The radiative heat transfer can be described by equation 3.3.

$$Q = \frac{k \cdot A}{x} \Delta T \cdot [W] \quad (3.1)$$

$$Q = h \cdot A \cdot (T_{\text{inf}} - T) [W] \quad (3.2)$$

$$Q = \epsilon \cdot \sigma \cdot A \cdot (T_{\text{inf}}^4 - T^4) [W] \quad (3.3)$$

The heat transfer coefficient  $h$  for the natural convection of air is a complex process but the average behaviour can be described with the model given in equation 3.4 [38] for a  $Ra < 10^9$ .

$$\begin{aligned} h_{ave} &= 0.56 F_{lam,air} \left( \frac{\Delta T}{L} \right)^{0.25} [W / (m^2 \cdot K)] \text{ [vertical wall]} \\ h_{ave} &= 0.54 F_{lam,air} \left( \frac{\Delta T}{L} \right)^{0.25} [W / (m^2 \cdot K)] \text{ [Horizontal area upside]} \\ h_{ave} &= 0.25 F_{lam,air} \left( \frac{\Delta T}{L} \right)^{0.25} [W / (m^2 \cdot K)] \text{ [Horizontal area downside]} \\ F_{lam,air} &= k \left( \frac{Ra}{L^3 \Delta T} \right)^{\frac{1}{4}} = 6.3126 - 1.4322 \log_{10}(T) \end{aligned} \quad (3.4)$$

Heating of a material changes its density which influence other material properties such as the thermal expansion coefficient of resistance (equation 3.5), the volume thermal expansion coefficient (equation 3.6) and the linear thermal expansion coefficient (equation 3.7).

$$\frac{dR}{dT} = \alpha_R \cdot R_0 \quad (3.5)$$

$$\frac{dV}{dT} = \alpha_V \cdot V_0 \quad (3.6)$$

$$\frac{dL}{dT} = \alpha_L \cdot L_0 \quad (3.7)$$

### 3.1.2 Dimensionless numbers

The thermal energy transfer in fluids and gasses has no clear boundary between the region of convection and conduction. Therefore dimensionless numbers were introduced which gave a possibility for determining the dominant factor in the heat transfer.

#### Reynolds

The Reynolds number (equation 3.8) defines the ratio between the inertial and the viscous forces in a flow. A Reynolds number below the boundary of 2000-3000 describes a laminar flow and a number above the boundary gives a turbulent flow. The Reynolds number is used in the case of forced flows along surfaces, in case of natural convection the Grashof number is used.

$$Re = \frac{\rho \cdot \vec{v} \cdot L}{\mu} \quad (3.8)$$

#### Grashof

The Grashof number (equation 3.9) defines the ratio between the internal driving force (buoyancy force) and the viscous force acting on the fluid/gas in the case of natural convection. A Grashof number in

the region  $10^8 - 10^9$  is the boundary between laminar and turbulent flow. The Grashof number is used to estimate the effect of free convection in comparison with pure heat conduction. The amount of free convection can be reduced by using a vacuum and small distances. Free convection can be neglected with  $Gr \leq 1000$  and with a  $Gr > 2000$  the convection term accounts for a 5% of the conductive flux.

$$Gr = \frac{g \cdot \beta \cdot \Delta T \cdot L^3}{(\mu/\rho)^2} \quad (3.9)$$

### Prandtl

The Prandtl number (equation 3.10) gives the ratio between the viscous diffusion and the thermal diffusion. A small Prandtl number gives an indication for conductive heat transfer as the heat flows quicker through the fluid/gas than the velocity of the gas/fluid. A high Prandtl number indicates convective heat transfer in the gas.

$$Pr = \frac{C_p \cdot \mu}{k} \quad (3.10)$$

### Rayleigh

The Rayleigh number (equation 3.11) gives the ratio between the convection and conduction. It is the multiplication of the Grashof and the Prandtl number. Convection occurs in the region of  $Ra > 1000 - 2000$  and below that the heat transfer mainly occurs by conduction. The Rayleigh number has a transition from laminar convection to turbulent convection at  $10^9$ .

$$Ra = Gr \cdot Pr = \frac{g \cdot \beta \cdot \rho \cdot C_p \cdot \Delta T \cdot L^3}{\nu k} \quad (3.11)$$

### Nusselt

The Nusselt number (equation 3.12) represents the ratio of the convective to conductive heat transfer across the surface where the fluid flows along. At a  $Nu=1$  convection and conduction play an equal part. At a Nusselt number in the range of 100-1000 a turbulent flow occurs due to the convection.

$$Nu = \frac{h \cdot L}{k_f} \quad (3.12)$$

### Biot

The Biot number (equation 3.13) gives the relation between the thermal conductivity within the material and the convective heat transfer along the boundary. A  $Bi < 0.1$  is generally used as a measure of one-dimensional heat flow and gives an indication of an absence of temperature gradient along the cross-section  $L$  of the material. In that case the heat conduction inside the material is much faster as the convective cooling on the surface. If  $Bi > 1$  the thermal gradient within the material becomes important and the body may not be evaluated as one with a uniform temperature.

$$Bi = \frac{h \cdot L}{k_b} \quad (3.13)$$

## 3.2 Fluidica

### 3.2.1 Gas kinetics

The behaviour of gasses can be described by the gas law which is in the ideal case given by equation 3.14. In reality no natural gas obeys this ideal description as the interaction between the molecules and volume of the molecules is neglected. The correction for these effects is given by the 'van der Waals' equation 3.15 where  $a$  corrects the attraction of the particles and  $b$  the average excluded volume. For the purpose of simplification in the industry the non-ideal correction is expressed with a single variable: the compression factor  $Z(T,p)$  (equation 3.16) [39].

$$V_{ideal} = \frac{n \cdot R \cdot T}{P} \quad (3.14)$$

$$k \cdot T = \left(p + \frac{a}{V^2}\right)(V - b) \quad (3.15)$$

$$V_{real} = Z(T, p)_{mix} \cdot V_{ideal} \quad (3.16)$$

For a mixture of  $N$  perfect gasses the total pressure is the sum of the partial pressures which is given in equation 3.17. The mass fraction  $Y_k$  is the mass of the gas  $k$  divided by the total mass of all gasses. The mean molecular weight for a mixture is given by equation 3.18.

$$p = \sum_{k=1}^N \rho_k \frac{R}{W_k T} [Pa] \quad (3.17)$$

$$\frac{1}{W} = \sum_{k=1}^N \frac{Y_k}{W_k} [mol/g] \quad (3.18)$$

The basics transport characteristics of gasses are defined by the diffusion, viscosity and thermal conductivity. These coefficients can be described by an equation based on the molecule collision diameter, molecule mass, temperature and pressure [40]. These coefficients can be described for a pure gas by equation 3.19. We can assume for atmospheric, non-dense gasses the approximation  $(\Omega^* \cdot T^*) = 1$  which is known as the Chapman-Enskog theory. Binary gasses can be described with the use of  $W$  as the mean mass and  $\bar{\sigma}$  as the mean collision diameter. The values for the used gasses are shown in table A.1.

$$\begin{aligned} D &= 2.6280 \cdot 10^{-7} \frac{\sqrt{T^3/W}}{\frac{p}{101.325} \cdot \bar{\sigma}^2 \Omega^{(1,1)*}(T^*)} [m^2/s] \\ \mu &= 2.6693 \cdot 10^{-6} \frac{\sqrt{TW}}{\bar{\sigma}^2 \Omega^{(2,2)*}(T^*)} [kg/m \cdot s] \\ k &= 1.9891 \cdot 4.184 \cdot 10^{-2} \frac{\sqrt{T/W}}{\bar{\sigma}^2 \Omega^{(2,2)*}(T^*)} [W/m \cdot K] \end{aligned} \quad (3.19)$$

### 3.2.2 Flows

The Hagen-Poiseuille equation [41] describes the hydraulic resistance (equation 3.20) of a laminar gas/liquid flow through a channel. The pressure drop over the channel is given by the flow speed through the channel multiplied by the hydraulic resistance. For laminar flows with a  $Re < 2000$  the hydraulic resistance can be described by equation 3.21.



$$R_h = 128\mu \cdot \frac{L}{\pi D^4} [Pa \cdot s/m^3] \quad (3.20)$$

$$\Delta p = R_h \cdot \varphi_V [Pa] \quad (3.21)$$

### 3.2.3 Combustion

#### Wobbe-index

The calorific value which is also known as the heating value (HV) of a gas is measured on industrial level with the Wobbe-index and is defined in the ISO 6976 standard [7]. The Wobbe-index is the heating value, the energy per cubic meter of gas in  $J/m^3$ , per square root of the relative density of the gas and is shown in equation 3.22. The Wobbe-index is temperature dependent as the density scales with the temperature and is therefore compensated with a factor  $\frac{T_{standard}}{T_{fuel}}$ .

$$'Wobbe - index' = HV_m \cdot \varphi_{relative} = \frac{HV}{\sqrt{\frac{\rho_{gas}}{\rho_{air}}}} \frac{T_{standard}}{T_{fuel}} [J/m^3] \quad (3.22)$$

The Wobbe-index gives the relation between heating value and the volume flow of a gas relative to air through an orifice at a constant pressure. The expression for a volume flow through the orifice is given in equation 3.23, with  $C$  the orifice constant,  $A$  the orifice area,  $p_1$  the pressure before the orifice,  $p_2$  the pressure behind the orifice. At a constant pressure drop the volume flow scales with the density and the volume flow relative to volume flow of air results in the scalar given by equation 3.24.

$$\varphi_V = C \cdot A \sqrt{\frac{2(p_1 - p_2)}{\rho}} [m^3/s] \quad (3.23)$$

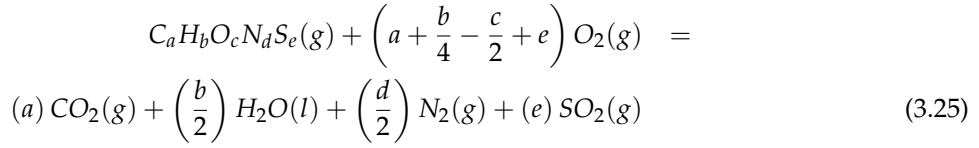
$$\varphi_{relative} \approx \frac{\varphi_{V-gas}}{\varphi_{V-air}} \approx \frac{\sqrt{\frac{1}{\rho_{gas}}}}{\sqrt{\frac{1}{\rho_{air}}}} \approx \frac{1}{\sqrt{\frac{\rho_{gas}}{\rho_{air}}}} [-] \quad (3.24)$$

The heating value is divided in a High Heating Value (HHV) and a Low Heating Value (LHV). Stoichiometric combustion results in the products  $H_2O$  and  $CO_2$  with the water in vapour phase. The condensation of the water vapour to liquid releases the latent heat of the water vapour which gives combined with the combustion heat the HHV or superior calorific value of the gas. If the water stays in the vapour phase there is no release of the latent heat which results in the LHV.

The fuel gas used in industry is of the type 'dry-gas' which means that there is less than  $5 \cdot 10^{-5}$  parts per mole of water vapour in the fuel gas. Combustion of 'wet-gas' results in a lower heating value. Also the extra components in the fuel like carbon dioxide and nitrogen influence the Wobbe-index negatively as they make the gas less energy dense.

#### Combustion of gas flows

Combustion is a chemical reaction between fuel and oxidizer which results in combustion products. The general formula for the stoichiometric breakdown of the gas ( $C_a H_b O_c N_d S_e$ ) into its combustion products is given in equation 3.25 where the indices  $a$  to  $e$  are zero or non-negative integers.



The stoichiometric mass ratio ( $s$ ) and the equivalence ratio ( $\phi$ ) are given in equation 3.26 in which  $\varphi_{F,O}$  are the mass-flow rates of the fuel and oxidizer.

$$\phi = \left(a + \frac{b}{4} - \frac{c}{2} + e\right) \cdot \frac{W_O}{W_F} \cdot \frac{Y_F}{Y_O} = s \cdot \frac{Y_F}{Y_O} = s \frac{\varphi_F}{\varphi_O} \quad (3.26)$$

The thermodynamic potential function for the combustion of gasses and liquids is given by equation 3.27 [1] in which  $S$  (entropy) and  $V$  (volume) are the independent variables and where  $\sum_i \mu_i \cdot dN_i$  represents the chemical energy of the reaction. By manipulation with Legendre transformations we can obtain other notations with independent variables such as the enthalpy ( $S, p$ ) (3.28), Gibbs free energy ( $T, p$ ) (3.29) and the Helmholtz function ( $T, V$ ) (3.30). The thermal capacity at fixed volume or fixed pressure can be calculated with equation 3.31 out of the energy and enthalpy. For combustion with a constant volume ( $dV = 0$ ) or a constant pressure ( $dp = 0$ ) the heat released by the chemical reaction gives the variation in heat of the system. The relation between the energy and enthalpy is given by  $E = H - p/\rho$ .

$$dE = T \cdot dS - p \cdot dV + \sum_i \mu_i \cdot dN_i \quad (3.27)$$

$$dH = T \cdot dS + V \cdot dp + \sum_i \mu_i \cdot dN_i \quad (3.28)$$

$$dG = -S \cdot dT + V \cdot dp + \sum_i \mu_i \cdot dN_i \quad (3.29)$$

$$dF = -S \cdot dT - p \cdot dV + \sum_i \mu_i \cdot dN_i \quad (3.30)$$

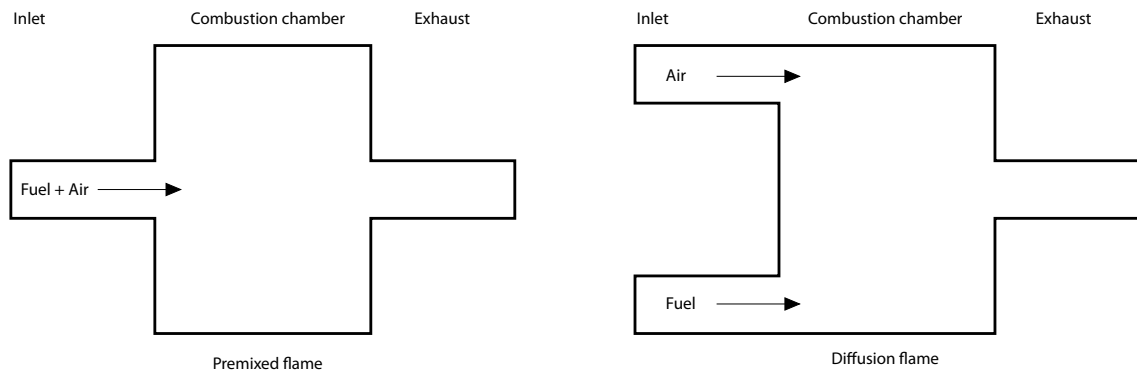
$$\left(\frac{\partial E}{\partial T}\right)_V = C_V$$

$$\left(\frac{\partial H}{\partial T}\right)_p = C_p \quad (3.31)$$

The relation between the  $C_p$  and  $C_v$  is given by  $C_p - C_v = R/W$  and in a system with multiple gasses the total  $C_v$  or  $C_p$  is the summation over the value of the gasses multiplied with its mass fraction. The total energy and enthalpy of a combustion are described by equations 3.32 [42]. The first term describes the energy stored in the system, the second term given the chemical energy of the reaction where  $\Delta h_{f,k}^0$  is the mass formation enthalpy and the third term is the three dimensional velocity field which gives the kinetic energy. When the energy and enthalpy are combined with expressions for conservation of momentum, conservation of mass and species and conservation of energy this can be used in a simulation to obtain numerical results. As a three dimensional velocity field only exists in the simulation environment we can exclude this term for the further calculations in this report. From the enthalpy and energy we can conclude that the heat that is already present in the system is added to the heating value generated by the combustion. The energy measured with the calorific sensor has to be compensated for this effect to derive the correct calorific value of the burned gas. The enthalpy can also be corrected for non-ideality effects [7] but as these are typical not bigger than 50 J/mol (0.005%) these are neglected at the industrial level but it has to be researched if these effects influence the calorific sensor.

$$\begin{aligned}
 E &= \left[ \int_{T_0}^T C_V dT - \frac{RT_0}{W} \right] + \left[ \sum_{k=1}^N \Delta h_{f,k}^0 Y_k \right] + \left[ \frac{\mu_i \cdot \mu_i}{2} \right] \\
 H &= \left[ \int_{T_0}^T C_p dT \right] + \left[ \sum_{k=1}^N \Delta h_{f,k}^0 Y_k \right] + \left[ \frac{\mu_i \cdot \mu_i}{2} \right]
 \end{aligned} \tag{3.32}$$

There are four different domains which can describe the formation of flames at combustion. These four categories are divided in two types: premixed and diffusion combustion. The difference between these types is shown in figure 3.2 and each of these types can be divided into two regimes: laminar and turbulent flows.



**Figure 3.2:** Combustion comes in two forms: premixed and diffusion combustion.

Combustion of premixed or laminar diffusion flows give the same combustion temperatures but the distribution and position of the heat are different. In figure 3.3 a sketch is shown which is a representation of the heat distribution in laminar diffusion flows. The distribution differs in the fact that the combustion has an offset to the side of the oxidizer where the stoichiometric mixture has the favourable mixing ratio. Far away from each side of the flame the gas mixture is either too lean or too rich to burn. The representation that is shown is only valid in the case of strained flames or with other words at the interface of colliding gasses. In case of an unstrained flame, where the two laminar flows do not collide, the flame gets choked in its combustion products and the reaction rate drops to zero. The strain influences the rate of chemistry and thereby also the resulting maximum combustion temperature. The introduction of turbulence in the feed streams results in an increase of the reaction rate of the combustion [42].

In the case of diffusion flames the flamelet stays stationary at the place of the collision of both flows as the flamelet is unable to propagate towards the fuel side due to lack of oxidizer or towards the oxidizer stream due to lack of the fuel. The maximum temperature  $T_{ad}$  inside the burner does only depend on the inlet stream temperature ( $T_F^0, T_O^0$ ), equivalence ratio  $\phi$ , the fuel mass fraction  $Y_F^0$  and the combustion energy  $Q$  and is described in equation 3.33. The temperature in other parts of the mixture is dependent of the fuel/air fraction.

$$T_{ad} = \frac{T_F^0 + \phi T_O^0}{1 + \phi} + \frac{Q Y_F^0}{C_p (1 + \phi)} [K] \tag{3.33}$$

There is usually no interaction between the flame and the wall. Due to the large temperature gradient the reaction quenches a few micrometer before the wall as the low temperature of most walls inhibit the chemical reactions. This large temperature gradient causes a large heat flux through the walls. In the

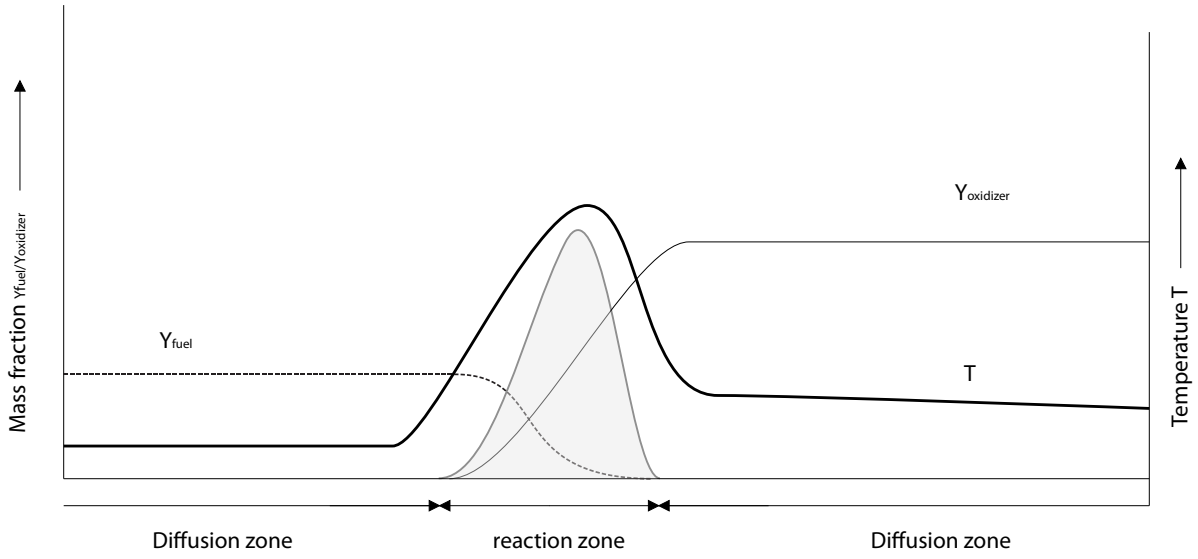


Figure 3.3: The combustion takes place in the region towards the oxidizer. The shaded area is the heat release.

case of a tube with cold side walls a propagating pre-mixed laminar flame can even be confined inside the tube if the radius is smaller than the quenching distance. The consequence of quenching and the resulting heat transfer for the combustion inside buried channels is something that has to be researched.

### 3.3 Mechanics

A shared load hanging at the end of beams results in a deflection of the beams. The deflection of beams due to a point load at its end ( $x = L$ ) can be described by equation 3.34.

$$\begin{aligned} w &= \frac{FL}{2EI} x^2 \left(1 - \frac{x}{3L}\right) \\ w_{mass} &= \frac{FL^3}{3EI} [m] \end{aligned} \quad (3.34)$$

The second moment of inertia is used in the deflection of the beams and can be described for a buried channel with equation 3.35 and 3.36. In this model the tube is described by a simple combination of a cylinder with a slab on top of it, a more sophisticated model [43] could be used but the difference in result for the  $I_{xx}$  would only be a factor of two and for  $I_{yy}$  a 4% which can be neglected for our purpose as this only further stiffens the beams. The axis of the model are shown in figure 3.4.

$$\begin{aligned} \bar{I}_{xx} &= (I_{xx} + A \cdot d_y^2)_a + (I_{xx} + A \cdot d_y^2)_b [m^4] \\ I_{xx(a)} &= \frac{1}{3} h^3 b \\ I_{xx(b)} &= \frac{\pi}{4} (R_o^4 - R_i^4) \\ X_{neutral-axis} &= \frac{(2 \cdot R_o) - R_o}{1 + \frac{A_b}{A_a}} + R_o \\ A_a &= bh \\ A_b &= \pi(R_o^2 - R_i^2) \end{aligned} \quad \begin{aligned} d_{y(a)} &= 2R_o - X_{neutral-axis} \\ d_{y(b)} &= X_{neutral-axis} - R_o \end{aligned} \quad (3.35)$$

$$\begin{aligned}
 \bar{I}_{yy} &= (I_{yy})_a + (I_{yy})_b \\
 (I_{yy})_a &= \frac{h_a b_a^3}{12} \\
 (I_{yy})_b &= \frac{\pi}{4} (R_o^4 - R_i^4)
 \end{aligned} \tag{3.36}$$

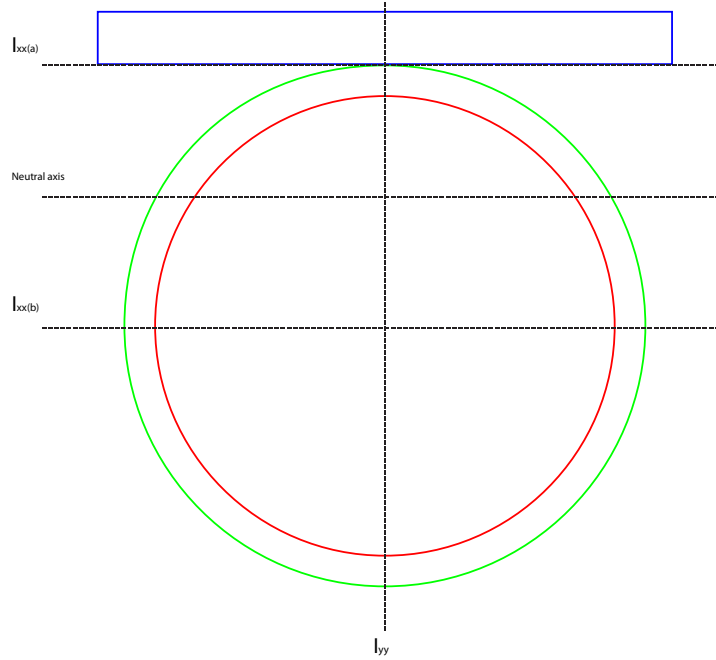


Figure 3.4: Simple model for the second moment of inertia.

The torsion stress of a beam can be described with (3.37):

$$\tau = \frac{Tq \cdot r}{J_z} = \frac{Tq \cdot r}{I_{xx} + I_{yy}} [N \cdot m] \tag{3.37}$$

The change of temperature on a wafer induces stress due to the difference in volumetric expansion coefficients of the materials (3.6). The deflection of two stacked layers due to layer stress is given by the radius of the curvature which can be described by  $\rho$  in equation 3.38. In this equation  $\nu$  is the poisson ratio.

$$\begin{aligned}
 \alpha_T &= \frac{\partial \epsilon_x}{\partial T} = \frac{\partial \frac{\Delta L}{L}}{\partial T} \\
 \tilde{E} &= \frac{(\frac{E_1}{1-\nu}) \cdot L_1 + (\frac{E_2}{1-\nu}) \cdot L_2}{L_1 + L_2} \\
 M &= \int_{-\frac{L_1}{2}}^{\frac{L_1}{2}} W \cdot z \cdot \alpha_{T1} \cdot \Delta T \frac{E_1}{1-\nu} dz + \int_{\frac{L_1}{2}}^{\frac{L_1}{2} + L_2} W \cdot z \cdot \alpha_{T2} \cdot \Delta T \frac{E_2}{1-\nu} dz \\
 I &= \frac{W \cdot (L_1 + L_2)^3}{12} \\
 \rho &= \frac{\tilde{E} I}{M} [m]
 \end{aligned} \tag{3.38}$$

### **3.4 Conclusion**

With the physical models described in this chapter the values for the design in the coming chapter can be found. With the temperature dependent properties of the gasses the heat transfer to and from gasses can be calculated. The combustion energy of the gas can be calculated which gives the thermal flux to the chip and from the chip by thermal losses. These thermal losses can be calculated with which the energy balance inside the chip can be found. This energy balance gives the temperature of the chip where thermal expansion of sections from the chip will result in deflection of the surface and stresses. This all will be put in practice in the coming chapter where the design will be discussed.

## Chapter 4

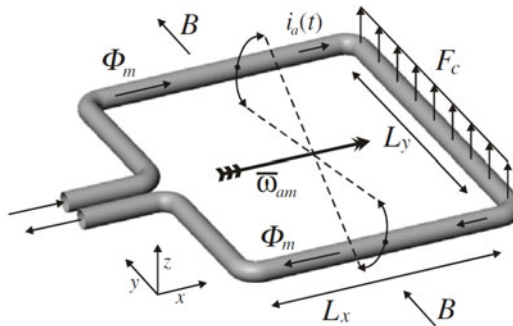
# Design

As was stated in the introduction the design needs to be compatible with the process of the micro-coriolis flow sensor [6] for future integration of both products. This requires that only minor adjustments can be made in the production process which do not influence the functioning of the micro-coriolis sensor.

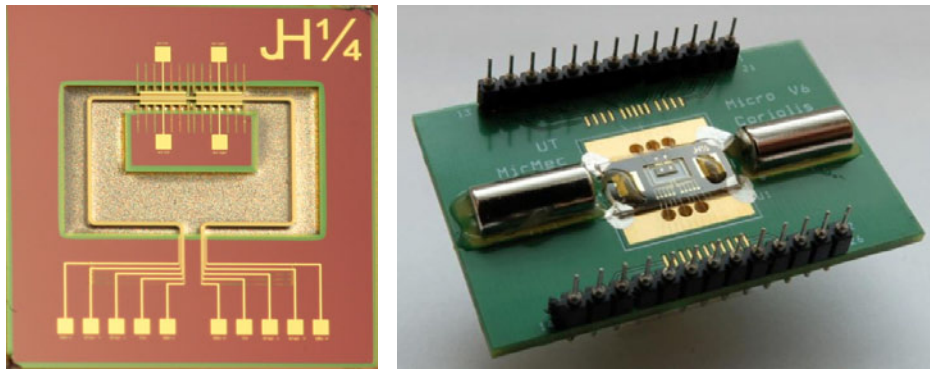
The main trademark of the micro-coriolis process are the buried channels which are used to transport to transport fluids/gasses across the chip. The fluids are introduced in the buried channels by means of access-holes on the backside of the wafer, these run from the back to the front of the wafer. The micro-coriolis sensor (figure 4.1) is designed for measuring the mass-flow ( $\phi_m$ ) and density of the liquids that flow through the sensor. The sensor is actuated which results with feedback in resonance at the resonance frequency ( $\omega_{am}$ ) with a displacement amplitude at the end of the structure caused by the Coriolis effect  $F_c$ . The Coriolis effect is a force resulting perpendicular to the flow cause by the mass flow through and the rotation of the buried channel in the plane of the chip. The tube is actuated with the oscillating current ( $i_a(t)$ ) which runs through the metal tracks on top of the tube. This creates a force perpendicular to the external magnetic field ( $B$ ) and the current.

The measurement range of the micro-coriolis sensor is for mass flows in the region of 1-1000 mg/h. The flow can be regulated when the flow measurement capabilities are combined with a feedback controlled valve. This can be used for regulating the total combustion energy in and pressure-drop over the calorific sensor.

The micro-coriolis chip is build on a silicon wafer where the SiRN deposited layers form the buried channels. On top of the SiRN a metal layer is placed which is made of gold with as adhesion layer chromium. A bare chip is shown in figure 4.2(a) in which the mass flow channel can be recognized as the rectangular with gold feature. The displacement of the channel due to the coriolis force is measured with a comb structure at the top of the tube. A packaged micro-coriolis sensor with external magnets for the magnetic field is shown in figure 4.2(b).



**Figure 4.1:** The rectangle-shaped Coriolis flow sensor ( $\omega_{am}$  is the actuation-mode angular velocity;  $F_c$  indicates the Coriolis force as a result of mass flow) [6].



(a) A bare micro-coriolis chip. The rectangular gold coloured structure is the nets for creating the magnetic field over the chip. The displacement due to the coriolis force is measured with the comb structure at the top of the channel.

Figure 4.2: (Author: Jeroen Haneveld)

The essential materials for the functioning of the micro-coriolis are the silicon wafer and SiRN. The type of metal layer can be replaced by another suitable metal and the thickness of the wafer can also vary as long as the access-holes can run through the wafer.

With the boundaries formed by the design of the micro-coriolis sensor an idea of an on-chip calorific sensor can be formed. The buried channels will be used for the transport and heating of the gas inside the chip where the heat will be provided at the outside of the buried channels. The already existing metal layer could be used as heater but we will discuss the possibilities in section 4.3. For measuring of the heating value we need to transfer the energy of the combustion into an iso-thermal medium. We can do this by creating a bulk around the channel in which the heat is transported, by measuring the temperature of the bulk and calibrating for the thermal losses we can derive the heating value. A chip with an area of a few square centimetre has a large thermal capacity which gives a lower temperature than a chip with a smaller thermal capacity for the same heating value. By reducing the area and isolating it from the outside world we can achieved a high resolution of the temperature increase per joule of heating value. The isolation can be achieved by suspending the core with beams in the air. The temperature of the bulk can be measured on the beams that connect the bulk with the outside world or directly on the bulk. Measuring the temperature on the beam requires a known relation between the location and the bulk temperature. A schematic integration of the micro-coriolis flow sensors and the calorific sensor is shown in figure 4.3. The outer dimensions of the chip will be 10mm x 20mm, this allows space between the in- and outlets of the chip which simplifies the alignment in the chip holder as the connecting ports can be larger. There will be two designs of the chip with different suspensions for the cores, the specifications of the designs will be discussed in the coming sections. The material properties of all materials mentioned in this report can be found in appendix A.

## 4.1 Bio-gas

The composition of bio-gas and other fuel gasses differs with the source. As fuel gasses we define liquifid natural gas (LNG) which is found below the earth's surface and is created from buried organic materials and the liquid petroleum gas (LPG) that is obtain by fractioning of oil. Bio-gas is gas obtain by the fermentation of bio-waste but each waste source gives another composition of the gas (table 4.1). Bio-gas has only a single alkane, methane, in its composition the rest are non-combustable gasses like CO<sub>2</sub> and N<sub>2</sub>. Higher alkane chains do not occur in the process of waste decomposition which classifies bio-gas as a low energy density gas. Bio-gas also contains a high percentage of water vapour which



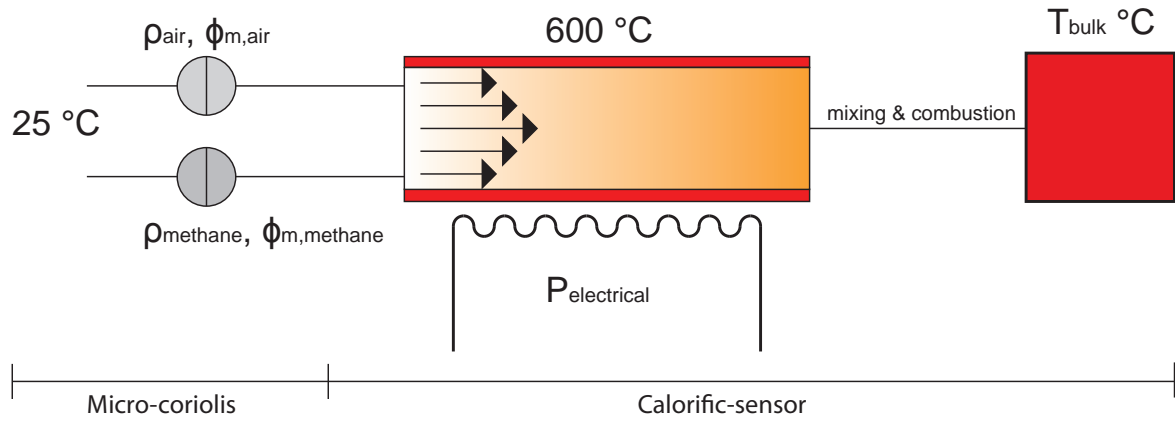


Figure 4.3: A basic design of the Wobbe meter.

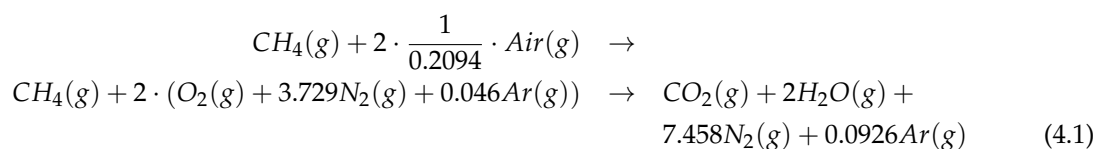
require the use of a condenser to obtain a more pure and energy dense gas. Liquified natural gas and liquified petroleum gas have higher alkane chains in the mixture with some non-combustable rest gasses, which gives these gasses a higher energy density than bio-gas.

Components	Household waste	Wastewater treatment plants sludge	Agricultural waste	Waste of agrifood industry	LPG	LNG
CH <sub>4</sub> (% vol.)	50-60	60-75	60-75	68	88.90	94.7
C <sub>2</sub> H <sub>6</sub> (% vol.)	-	-	-	-	5.34%	4.8%
C <sub>3</sub> H <sub>8</sub> (% vol.)	-	-	-	-	0.46%	0.4%
C <sub>4</sub> H <sub>10</sub> (% vol.)	-	-	-	-	0.05%	0.06%
C <sub>5</sub> H <sub>12</sub> (% vol.)	-	-	-	-	0.03%	0.01%
C <sub>6</sub> H <sub>14</sub> (% vol.)	-	-	-	-	0.02%	0.01%
CO <sub>2</sub> (% vol.)	38-34	33-19	33-19	26	0.5	-
N <sub>2</sub> (% vol.)	5-0	1-0	1-0	-	5.5	0.02
O <sub>2</sub> (% vol.)	1-0	< 0.5	< 0.5	-	-	-
He (% vol.)	-	-	-	-	0.2%	-
H <sub>2</sub> O (% vol.)	6 (@ 40°C)	6 (@ 40°C)	6 (@ 40°C)	6 (@ 40°C)	-	-
H <sub>2</sub> S (mg/m <sup>3</sup> )	100 - 900	1000 - 4000	3000 - 10,000	400	-	-
NH <sub>3</sub> (mg/m <sup>3</sup> )	-	-	50 - 100	-	-	-
Aromatic (mg/m <sup>3</sup> )	0 - 200	-	-	-	-	-
Organochlorinated / fluorated (mg/m <sup>3</sup> )	100-800	-	-	-	-	-

Table 4.1: Chemical composition of bio-gasses from different sources and the general values for LPG and LNG [44, 45].

All these gasses have in common that their main part consists out of methane, but for the purpose of testing industrial methane gas [46] will be used with a purity of 99.5% and a higher heating value of 50.72 MJ/m<sup>3</sup> at 15°C. This makes it easier to calculate and verify the resulting calorific value of the combustion inside the chip.

The stoichiometric combustion of methane with air according to equation 3.25 requires the composition of air which is given in table 4.2. For the process of simplification we only use the first three components from the table and increase the percentage of argon to 0.97% as most of the extra gasses are also noble gases and non-combustable. The resulting stoichiometric reaction is given in equation 4.1.

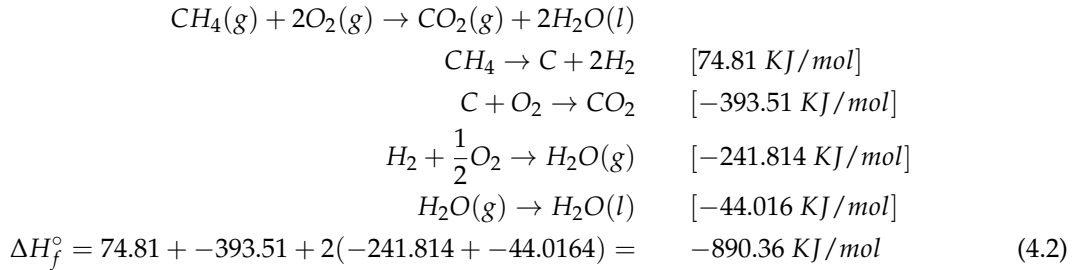


The energy balance of the methane combustion is given in equation 4.2, the summation over these

Components	Percentage (%)	Components	Percentage (%)
N <sub>2</sub>	78.09	Kr	$1.1 \cdot 10^{-4}$
O <sub>2</sub>	20.94	CH <sub>4</sub>	$1.77 \cdot 10^{-4}$
Ar	0.93	H <sub>2</sub>	$500 \cdot 10^{-7}$
CO <sub>2</sub>	$385 \cdot 10^{-4}$	Xe	$86 \cdot 10^{-7}$
Ne	$18 \cdot 10^{-4}$	Rn	$6 \cdot 10^{-18}$
He	$5.2 \cdot 10^{-4}$		

Table 4.2: The composition of air.

energies gives the higher heating value at  $T_0=293.15\text{K}$ . The negative numbers indicate an exothermic reaction. The reaction starts with an endothermic reaction for the breakdown of the gas into basic stable components, the energy to overcome this threshold has to be delivered by the ignition source, after that the reaction is exothermic. The adiabatic flame temperature in the ideal case of the combustion of methane at a constant pressure is  $1950^\circ\text{C}$ . The auto ignition temperature, which is the thermal energy needed to overcome the endothermic threshold, lies at  $580^\circ\text{C}$ .



The combustion of methane can also be described in a more complex manner by use of the GRI-mech database [47] which was designed to model natural gas combustion, including nitrogenoxide formation and reburn chemistry. This database can be used for computer-modelling of the combustion but for the sake of simplicity the four step decomposition given in (4.2) will be used. As a design choice the latent heat of the fourth step will not be retrieved. The condensation of the water vapour would require a significant long channel for cooling of the gasses towards room-temperature which would be difficult to realize on chip. This has as consequence that only the lower heating value can be measured with the calorific sensor.

In the design shown in figure 4.3 the methane and air are heated to  $600^\circ\text{C}$  which is above the auto-ignition temperature to ensure the a complete combustion. By using (3.32) the resulting enthalpic energy can calculated of the combustion with pre-heated gas. The gas flows will be regulated with mass-flow-controllers (MFC's) with a nominal flow for air of  $1 \text{ g/h}$  and a nominal methane flow of  $0.058 \text{ g/h}$  which results in an combustion energy of  $0.96 \text{ J/s}$  at a continuous flow. Without preheating and by using an alternative ignition source such as an electrical spark the same stoichiometric mixture would produce  $0.8 \text{ J/s}$ . The mass fractions for the fuel and oxidizer stream are  $Y_F=1$  and  $Y_O=0.231$  with a stoichiometric mass ratio of 4 and an equivalence ratio of 17.23 (3.26) which gives a maximum flame temperature of  $2832\text{K}$  (3.33). The maximum flame temperature looks high but the energy flow is low with the channel wall as a good conductor. Furthermore the temperature at other parts of the gas is mass fraction dependent where at the wall the temperature drops due to the quenching.

## 4.2 Fluidics

For the transport of gasses inside the chip the buried channels technology is used. The goal is to keep the pressure-drop over the fluidic network below the 5 bar (500,000 Pascal) at the nominal flow speed of  $1\text{g/h}$  for air and  $0.058\text{g/h}$  for methane.

The pressure-drop can be reduced by placing multiple channels in parallel or by combining them into a single large channel. Also decreasing the overall length reduces the pressure-drop. The parallel placement of the channels reduces also the flow-speed through the channels. It is essential that the flow speed is low enough for proper convective heat transfer into the fluid as will be shown in the model of the gas-heater in the next section. The flow speeds through different channel types can be found in table 4.3.

Channel type	cross-section area [m <sup>2</sup> ]	≈ diameter [m]	air flow [m/s]	Reynolds air	methane flow [m/s]	Reynolds methane
Single	$1.09 \cdot 10^{-9}$	$3.72 \cdot 10^{-5}$	212.90	560.91	22.60	53.71
Double	$2.07 \cdot 10^{-9}$	$5.13 \cdot 10^{-5}$	112.00	406.84	11.89	38.96
Triple	$3.04 \cdot 10^{-9}$	$6.23 \cdot 10^{-5}$	75.99	335.11	8.07	32.09

Table 4.3: Nominal flow speed through different channel types with their Reynolds numbers.

The exact reaction rate of the combustion at the point of introduction in the combustion channel is unknown and by introducing some variations in the length and structure of the combustion chamber we can further investigate this phenomenon. A research question would be if the length of the reactor is as dominating factor for a complete combustion inside the channel, or creates the reaction a steady flamelet at the point of the colliding flows as was stated in [42]?

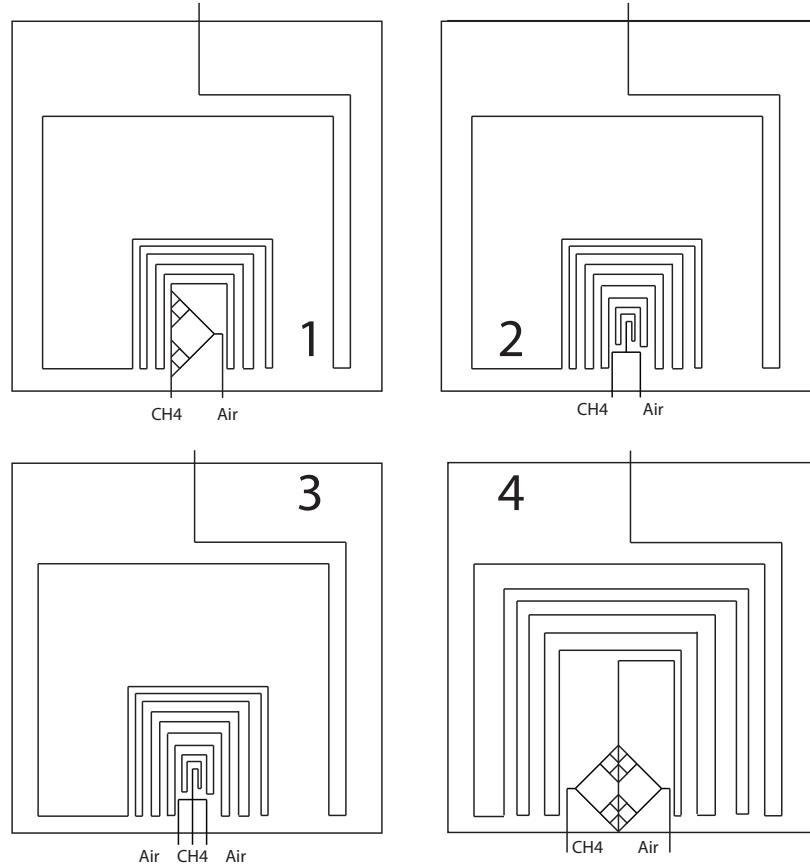
#### 4.2.1 Mixers

The velocity of the air flow is a factor 5.2 bigger than the methane flow. Both flows are laminar in the channels and by introduction them into the combustion channel these will continue as a laminar flow where the layers are stacked on top of each other. Due to the difference in flow velocity the air wants to reduce its hydraulic resistance and tries to achieve this by pressing the methane flow as a thin layer against the channel wall until the resistance of both flows are equal. This all has as consequence that the diffusion of the methane into the air will have to occur over a longer distance in the cross-section and that far from the combustion contact area an unused fraction of oxygen will remain.

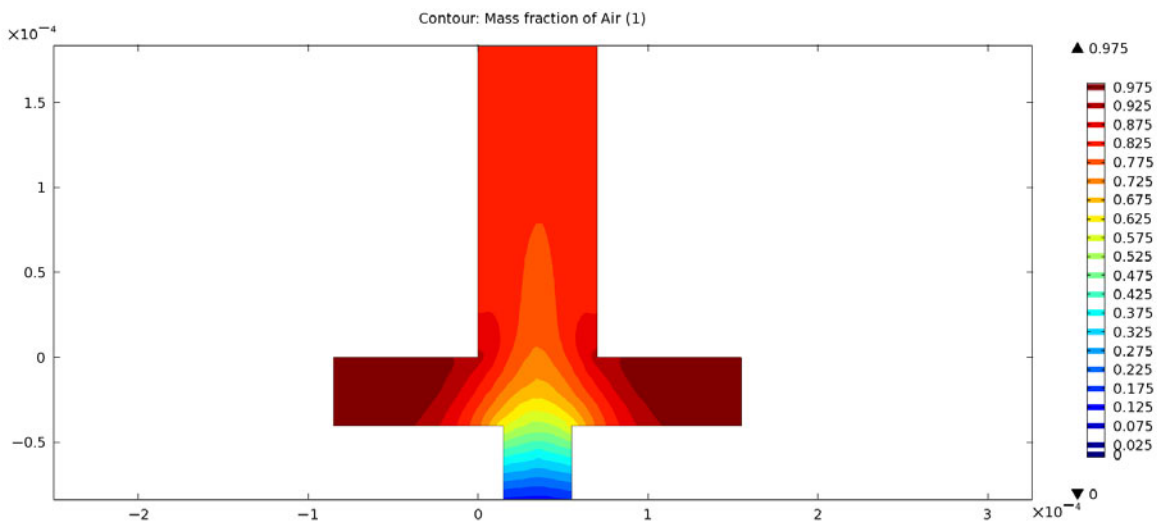
An effective way of increasing the contact area between methane and air and thereby improving the mixing by diffusion would be creating a multi-layered alternating sheet of air and methane with the use of T-mixers [48], this maximizes the contact area and diffusion of both gasses. The downside of this form of mixing is that a double-layer of buried channels are needed which makes the processing more complex and more than doubles the cleanroom production-time. An alternative for the double-layer would be making all the fluidic crossings outside the chip but this increases the size and complexity of the packaging.

Multiple mixing structures were investigated but almost all are dominated by the sheets formation of methane against the channel wall due to the velocity difference. A solution is provided by using a sheet mixer [49] which is shown as option 3 in figure 4.4 which laminates a single layer methane between two layers of air in the centre of the channel. The air inlet on the chip will be split into two sections which will be routed around the air inlet. A simulation of a sheet mixing between air and methane with the mass fraction of air gives the result shown in figure 4.5 where the velocity field given by figure 4.6.

In section 3.2.3 was stated that creating a turbulent gas flow increases the interface area between the two gasses which shortens the combustion length. The increase of the interfaces between the gasses can be achieved by introduce them into a combustion channel with mixer structures [50]. As the buried channels are closed structures it is not possible to introduce a pillar in the centre of the channel. An approach to create mixing structures with pillars in buried channels is by merging of multiple channels into one large channel. Obstacles in the channel can be created by selectively creating interruptions in the channel pattern. A buried channel is build out of spherical etched cavities with a diameter of 40  $\mu\text{m}$ , these cavities are etched through slits which are spaced every 3  $\mu\text{m}$  in the SiRN. With three parallel slit rows that are spaced 30  $\mu\text{m}$  from each other and an insertion of an interruption of 5 slits in the centre channel creates a pillar with a dimension of 10  $\mu\text{m}$  thick and 20  $\mu\text{m}$  wide.



**Figure 4.4:** Different kinds of mixing structures for mixing of air with methane. All design except number 3 create a layer of methane against the wall of the channel.



**Figure 4.5:** A simulation of the mass fraction within a sheet mixer. The ideal mass fraction mixing ratio for combustion is given at the position  $Y_o = \frac{\phi}{1+\phi} = 0.945$ .

To gather some information about how such a pillar would influence the flow inside the channel simulations were made in Comsol Multiphysics 3.5. The settings used in the simulation are; the top half of the inlet at the left side has a flow speed of 50 m/s, the bottom half has a flow speed of 5 m/s, fluid inside the model is air and a laminar flow simulation model is used. As high velocity computations create a

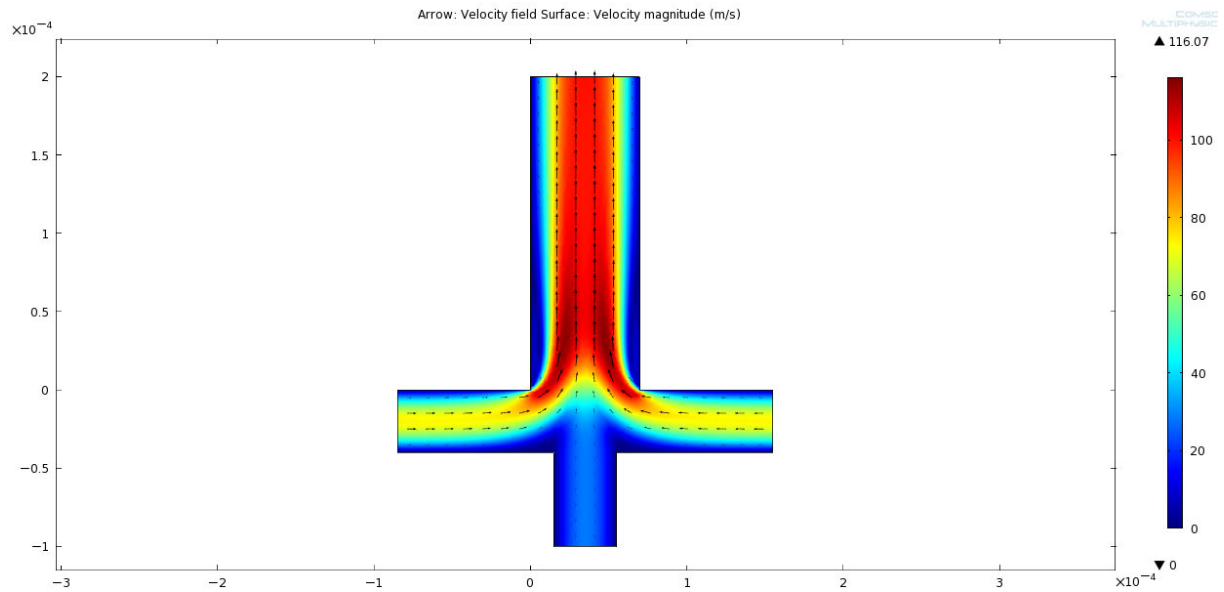


Figure 4.6: The velocity field inside the sheet mixer.

diverse array of problems we did not use the velocities found in table 4.3. All the figures show the air velocity. The simulation model shows pointy corners as it is build out of circles with a diameter of  $40\text{ }\mu\text{m}$  but in the real world these will be more rounded due to the etching process, the pointy surfaces have more contact area during the etching which increases the etch rate of the etchant.

Figure 4.7 shows multiple pillars behind each other with a spacing of  $40\text{ }\mu\text{m}$ . As the flow collides with the first pillar a large fraction is directed to the top and a small part is directed to the bottom part of the channel, between the pillars circulation zones are created.

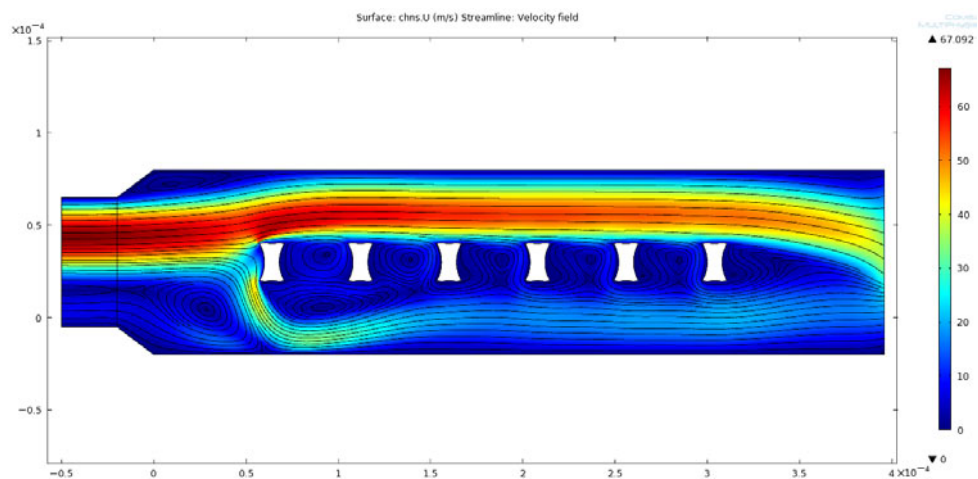
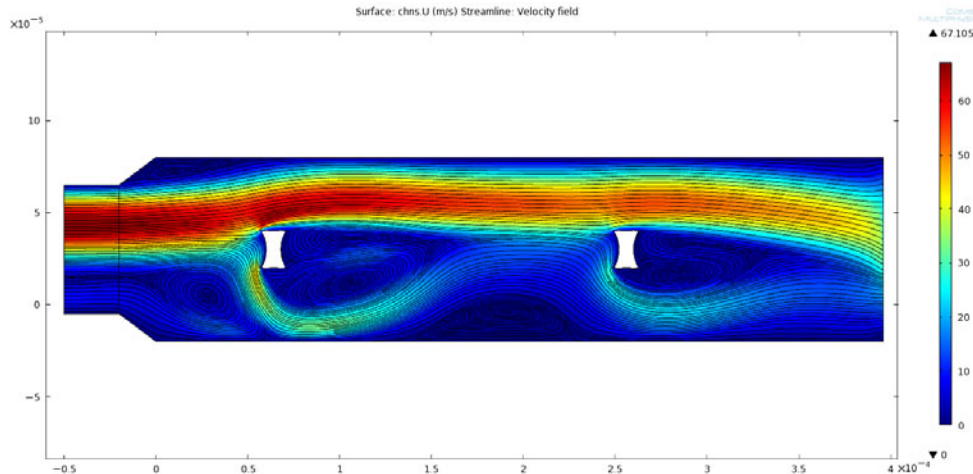


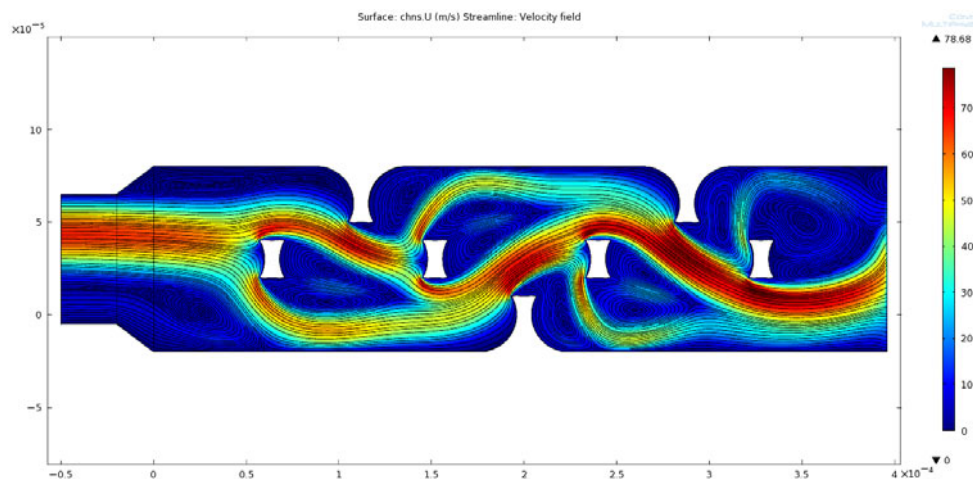
Figure 4.7: This figure shows the velocity of the flow in a buried channel mixer with a minimum distance of  $40\text{ }\mu\text{m}$  between the pillars. The majority of the flow is routed to the top of the channel.

Figure 4.8 shows two pillars behind each other with a spacing of  $140\text{ }\mu\text{m}$ . As the flow collides with the first pillar a large fraction is directed to the top and a small part is directed to the bottom. We can see that the flow wants to focus itself again into the centre of the channel after an  $80\text{ }\mu\text{m}$  and collides again with the next pillar. With smaller distances between the pillars the flow keeps to the edges of the channel.

To improve the mixing interruptions are added in the outer channels which results in figure 4.9. By alternating the pattern of interruption in the top and the bottom the flow can be folded.



**Figure 4.8:** This figure shows the velocity of the flow in a buried channel mixer with a distance of  $140\ \mu\text{m}$  between the pillars. The majority of the flow is routed to the top of the channel. The flow tries to focuss itself after  $80\ \mu\text{m}$  and collides against the next pillar.

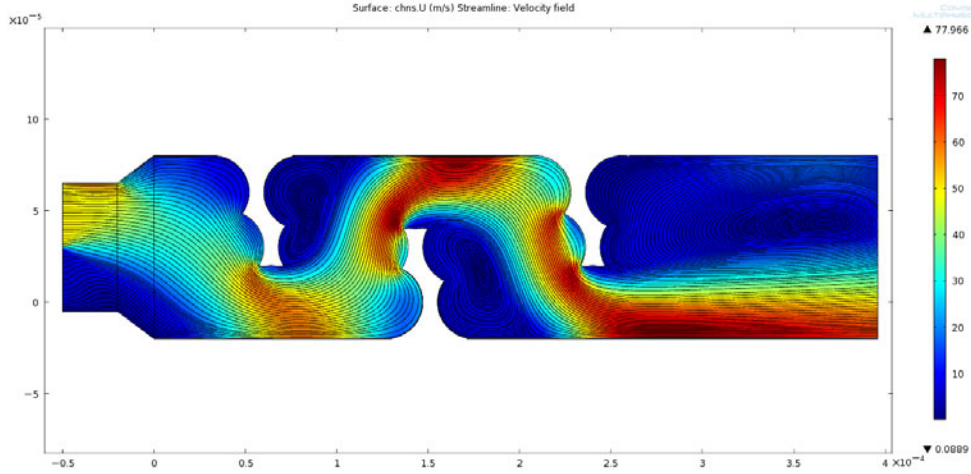


**Figure 4.9:** This figure shows the velocity of the flow in a buried channel mixer with a distance of  $80\ \mu\text{m}$  and repeating obstacles at the wall. The flow is forced to mix by folding of the streams into each other.

Another option was creating a giant maze as is shown in figure 4.10. We can see disturbances in the flow velocity due to the pointy edges. Behind the wall circulation zones are occurring. This method is ideal for increasing the path length but will not significantly improve the mixing of the fluids.

The mixing pattern of figure 4.9 seems the most promising and with extra simulations the influence of the spacing in an  $1\ \text{mm}$  long section is researched. In these simulation a concentration is introduced into the lower half of the inlet with a gas diffusion coefficient of  $D = 1 \cdot 10^{-5}\ \text{m}^2/\text{s}$ . Simulations show that the obstruction placement does not significantly influence the diffusion of the concentration over a length of  $1\ \text{mm}$  but compared with no blockage in the channel the diffusion with a mixer is faster. The spacing may not matter for gasses due to their high diffusion rate but the spacing can be of influence for mixing of liquids.

By choosing correct slit sequences we can create mixing structures like the pattern that is shown in figure 4.11. The figure is created with the pattern shown in table 4.4 which creates the folding structure of figure 4.9. The shortest repeating mixing pattern that can be creates is 16 slits long (appendix B) as the pillars cannot stand any closer to each other without losing pillars in the centre or at the sides. As



**Figure 4.10:** This figure shows the velocity of the flow in a buried channel mixer which is build as a maze to create the longest flow path. Recirculation zones are created behind the obstacles.

simulations turned out that the spacing did not influence the mixing we make a 250  $\mu\text{m}$  long mixing pattern which is shown in table 4.4. The length is arbitrary but we want to keep sections that act as wide combustion chambers which also gives a lower hydraulic resistance than shorter sections.



**Figure 4.11:** On the left is shown a normal channel and on the right a mixing structure based on table 4.4.

pattern-length = 32	
pattern <sub>[1]</sub>	= 1,1,1,1,1,1,1,1,1,1,1,1,1,1,0,0,0,0,0,1,1,1,1,1,1,1,1,1,1,1
pattern <sub>[2]</sub>	= 1,1,1,1,1,1,0,0,0,0,0,1,1,1,1,1,1,1,1,1,0,0,0,0,0,1,1,1,1,1
pattern <sub>[3]</sub>	= 0,0,0,1,0,0

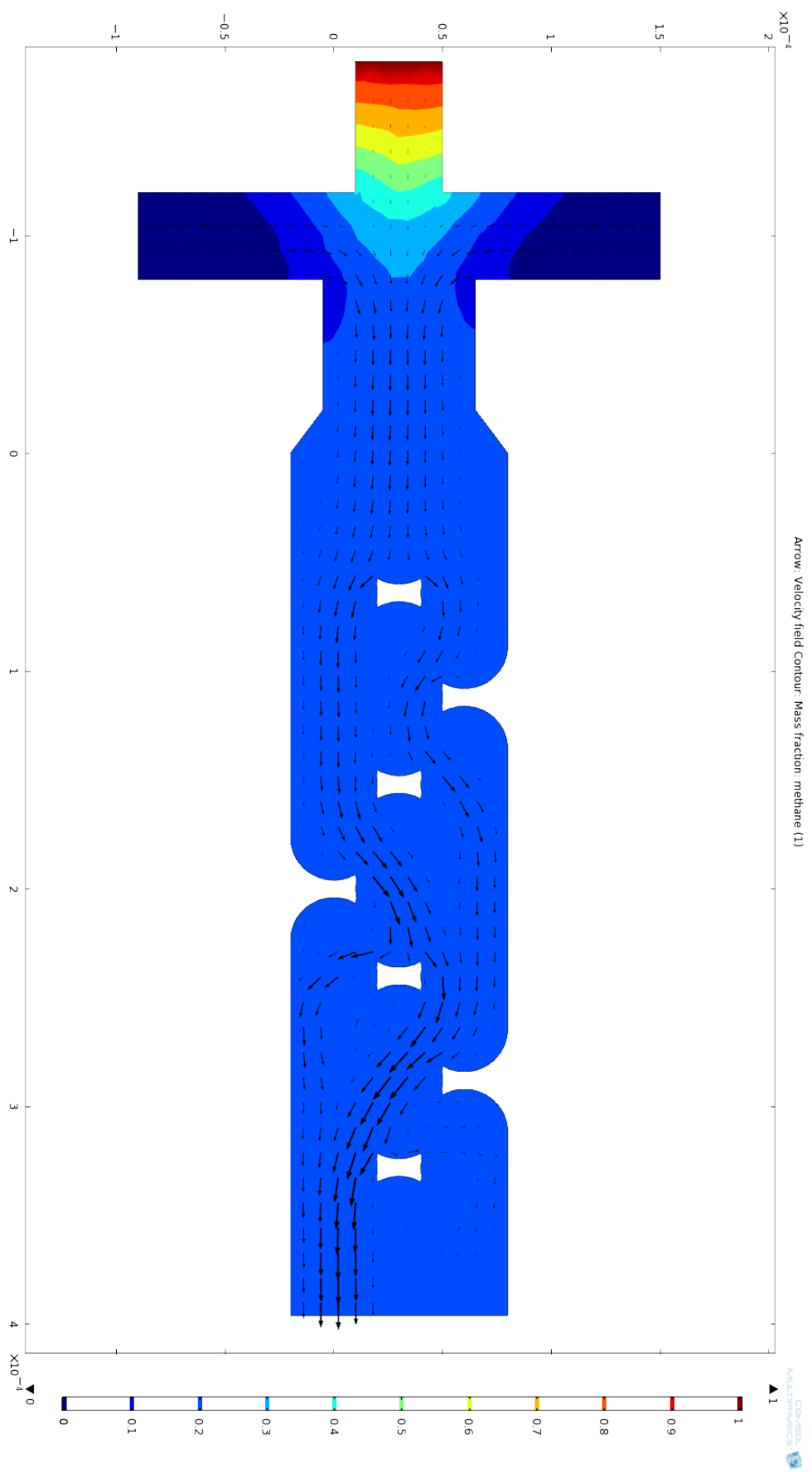
**Table 4.4:** A repeating coding pattern with a length of 32 slits for the mixers. In this pattern the width of the channel is 20 times  $51.3 \cdot 10^{-6} \mu\text{m}$  and 12 times  $62.3 \cdot 10^{-6} \mu\text{m}$  which gives an average width per section of  $55.4 \cdot 10^{-6} \mu\text{m}$

By combining the sheet flow inlet and the mixing structure we obtain figure 4.12. The middle inlet introduces the methane and the side inlets the air. The mass fraction of methane is shown and as calculated the stoichiometric mixture has an optimum at a  $Y_f=0.055$ . The mass fraction of 0.055 can be found at the air inlets which shows that there is a possibility that the combustion happens at that place and that there are no mixing section needed. However the simulation does not simulate the combustion and to be sure that the combustion of the fuel will happen inside the chip some variations are designed with different lengths and structures in the combustion channel.

## 4.2.2 Network model

Figure 4.13 gives the design of the basic fluidic network in the calorific chip.

When the pressure drop over the network is within the specifications of the MFC's then the gas-source can be seen as a flow source with a constant flow. After the point of combustion in the fluidic network the flow speed increases due to the thermal expansion and the different combined density of the combustion products  $\text{H}_2\text{O}$  and  $\text{CO}_2$ . With the increase of flow speed also the pressure drop increases. To calculate the total pressure drop the network has to be divided into sections, which is shown in figure 4.13. The



**Figure 4.12:** The combination of a sheet flow inlet and a mixing structure. The velocity field is shown by the arrow plot and the fuel mass fraction is shown in the contour plot where  $Y_f=0.055$  gives the position of possible combustion.



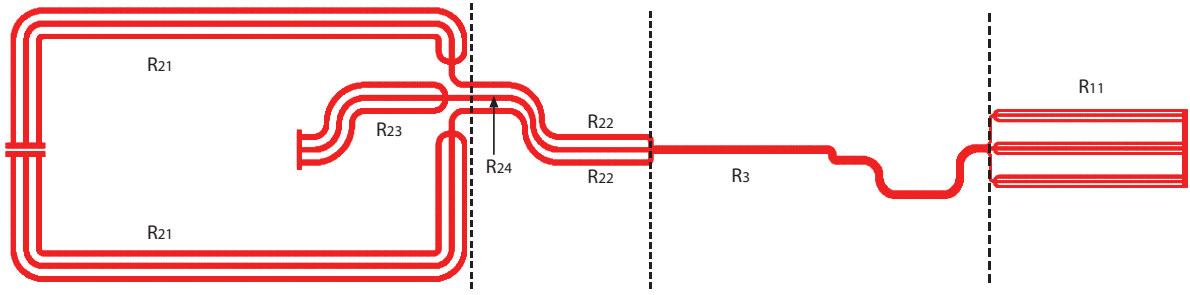


Figure 4.13: An overview of the on-chip fluidic network.

gas flows see each other at the mixer and when in the worst case the methane MFC cannot overcome the pressure drop of the network a pulsed flow of methane will occur due to the periodic build up of pressure inside the methane channel. In the ideal case we can use superposition of the flows to calculate the pressure-drops in the sections of the network.

The sections of figure 4.13 are specified in table 4.5 and with these values the pressure drops can be calculated for the network with (4.5). We take in account that the volume expands during the heating and combustion and therefore a flow speed increase factor is introduced so that we can keep the nominal flow in the equation. When the flows meet each other they create an unified pressure-drop in  $R_3$  and  $R_{11}$  which gives a  $\Delta P_{air}$  of  $1.69 \cdot 10^6$  Pa and  $\Delta P_{methane}$  is  $1.54 \cdot 10^6$  Pa at nominal flow during operation. In case that no combustion would happens due to the failure of the heaters the pressure drop  $\Delta P_{air}$  would be  $1.28 \cdot 10^5$  Pa and  $\Delta P_{methane}$  would be  $0.81 \cdot 10^5$  Pa.

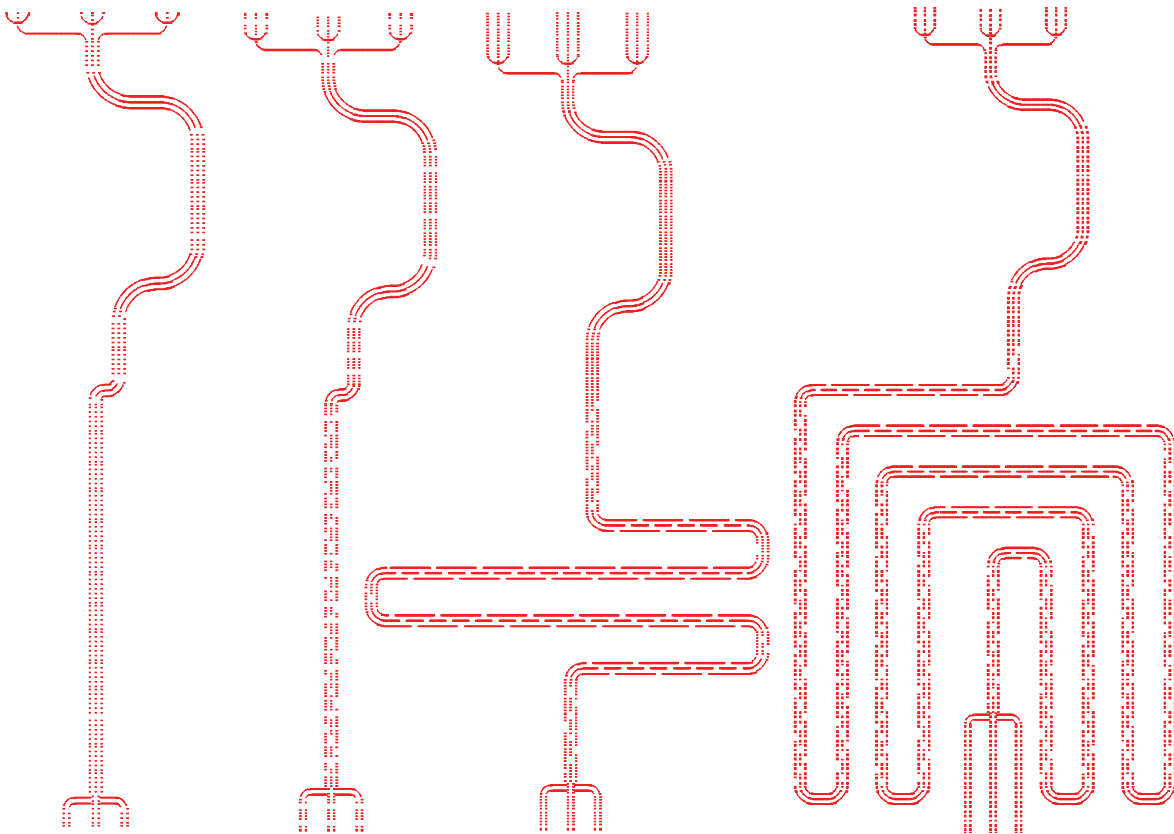
$$\begin{aligned}
 \Delta P_{air} &= \left(\frac{1}{6} R_{21} \cdot \varphi_V\right) + \left(\frac{1}{2} R_{22} \cdot \varphi_V\right) + (R_3 \cdot \varphi_V) + \left(\frac{1}{9} R_{11} \cdot \varphi_V\right) \\
 &= \left(\frac{1}{6} 5.82 \cdot 10^{11} + \left(\frac{1}{2} 4.49 \cdot 10^{11} \cdot 2.978\right) + (7.52 \cdot 10^{11} \cdot 7.583) + \left(\frac{1}{9} 3.26 \cdot 10^{12} \cdot 7.583\right) \cdot \varphi_V\right. \\
 &= 1.55 \cdot 10^6 \text{ [Pa]} \\
 \Delta P_{methane} &= \left(\frac{1}{3} R_{23} \cdot \varphi_V\right) + (R_{24} \cdot \varphi_V) + (R_3 \cdot \varphi_V) + \left(\frac{1}{9} R_{11} \cdot \varphi_V\right) \\
 &= \left(\frac{1}{3} 1.27 \cdot 10^{11} + (3.412 \cdot 10^{11} \cdot 2.978) + (7.52 \cdot 10^{11} \cdot 7.583) + \left(\frac{1}{9} 3.26 \cdot 10^{12} \cdot 7.583\right)\right) \cdot \varphi_V \\
 &= 1.69 \cdot 10^5 \text{ [Pa]}
 \end{aligned} \tag{4.3}$$

Section	Length [m]	diameter [m]	gas	Temperature [°C]	$\varphi_V$ increase	viscosity [Pa · s]
R <sub>11</sub>	$2.2 \cdot 10^{-3}$	$37.2 \cdot 10^{-6}$	H <sub>2</sub> O, CO <sub>2</sub> , N <sub>2</sub> , Ar	1950	7.583	6.96338E-05
R <sub>21</sub>	$6.7 \cdot 10^{-3}$	$54.5 \cdot 10^{-6}$	Air	20	1	1.87E-05
R <sub>22</sub>	$3.0 \cdot 10^{-3}$	$54.5 \cdot 10^{-6}$	Air	600	2.978	3.24E-05
R <sub>23</sub>	$2.1 \cdot 10^{-3}$	$54.5 \cdot 10^{-6}$	CH <sub>4</sub>	20	1	1.30E-05
R <sub>24</sub>	$3.0 \cdot 10^{-3}$	$54.5 \cdot 10^{-6}$	CH <sub>4</sub>	600	2.978	2.25E-05
R <sub>3</sub>	$5 \cdot 10^{-3}$	$65.9 \cdot 10^{-6}$	H <sub>2</sub> O, CO <sub>2</sub> , N <sub>2</sub> , Ar	1950	7.583	6.96E-05

**Table 4.5:** The hydraulic resistance parameters of the network. The speed increase is the increase from 20°C to the given temperature for the flow speed due to the expansion of the volume.

From this can be concluded that in the worst case during a combustion a huge pressure drop of 16.9 bar over the chip will occur and that for operation below the 5 bar pressure drop the nominal flow has to drop by a factor of 3.4. As the exhaust gas will cool the flow speed will decrease and the expansion factor assume that the gas is uniform heated but that is mass-fraction dependent. This causes us to believe that the pressure-drop over the combustion will be lower than calculated, measurements have to turn out what the resulting pressure-drop due to combustion will be.

As was mentioned earlier the complete combustion length is an unknown factor in the design and for further research four different designs are introduced which are shown in figure 4.14. The fourth design uses the maximum area that is available in the bulk of the chip and as the 3 variations are used to find the limit of the combustion length the flows have to be scaled to obey the maximum pressure drop of 5 bar. These designs vary the length of the hydraulic resistance  $R_3$ , for the first design we calculated in the previous part the pressure-drop and with this method we can find for the other designs the pressure-drops (table 4.6). It can be seen that the nominal flow would give excessive pressure-drops and that for design 4 the flow has to drop even with a factor 25 to give a pressure-drop of 5 bar which is well within the flow regulation range of 1/50 of the MFC's.



**Figure 4.14:** The four variations in the length of the fluidic network, the first one has a normal channel structure and the rest has a mixer pattern.

Design	Length $R_3$ [m]	$\Delta P$ Air [Pa]	$\Delta P$ Methane [Pa]
1	$5 \cdot 10^{-3}$	$1.69 \cdot 10^6$	$1.54 \cdot 10^6$
2	$5 \cdot 10^{-3}$	$2.97 \cdot 10^6$	$2.82 \cdot 10^6$
3	$11 \cdot 10^{-3}$	$5.74 \cdot 10^6$	$5.59 \cdot 10^6$
4	$25.5 \cdot 10^{-3}$	$12.43 \cdot 10^6$	$12.28 \cdot 10^6$

**Table 4.6:** The hydraulic resistance for the nominal flow of the network variations. For design 2-4  $R_3$  the mixing structure has an average width of  $55.4 \cdot 10^{-6} \mu\text{m}$ .

### 4.3 Heaters

For getting over the endothermal threshold of the decomposition of the methane gas energy is needed which can be delivered to the gas in a few ways: electrical, optical and thermal. The electrical manner transfers the energy by means of an electrical field. A high frequency oscillating field can create a plasma of the gas. A DC field can accelerate electrons and ions which will collide with the gas or even create an electron avalanche at short distances which results in a spark. The gas can optical be ignited by energy transfer with a focused laser where the photons bombard the gas particles and absorption leads to an increased energy level of the particles. There are multiple ways for delivering thermal energy to the gas. This can be done by indirectly heating the gas with energy transfer by convection and conduction. The material which surrounds the gas can be heated with infra-red or broad-spectrum (white light) radiation. The material can also be heated by Joule-heating or with conduction from an external Joule heater.

Electrical ignition of the gas will be difficult as the gas is encapsulated in the buried channel. This would require introducing electrodes in the closed channel but this is not feasible within the production process. The use of a focused high power laser would increase the price and the size of the packaging of the product. Also the encapsulation of the gas would result in heating of the material with the laser instead of the gas. An external radiation source like infra-red light can be a cheap solution but this would increase the size of the packaging. Joule heating is easy to integrate on the chip as the basic production process already includes a conductive metal layer. Using the SiRN as a conductor for Joule heating would pose a problem as SiRN is an isolator with  $10^{14} \Omega \cdot m$ . However the underlying silicon with  $1 - 10 \Omega \cdot m$  is an excellent conductor. By using silicon as conductor every metal path on the bare silicon would create a short to the ground. A solution for this problem would be using an isolation layer like silicon dioxide or SiRN between the silicon and the metal layer where only the heating areas would have no isolation. The current through the silicon would not only flow the shortest way to the ground but also between potential differences on the chip which introduces leakage currents.

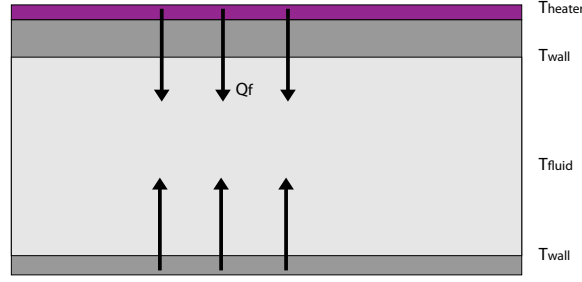
The current process of the micro-Coriolis already uses a metal layer which lies on the SiRN surface, with this layer ohmic heaters can be created that can heat local areas. This has no extra costs and it does not increase the size of the packaging therefore it will be used in the design.

#### 4.3.1 Heat transfer

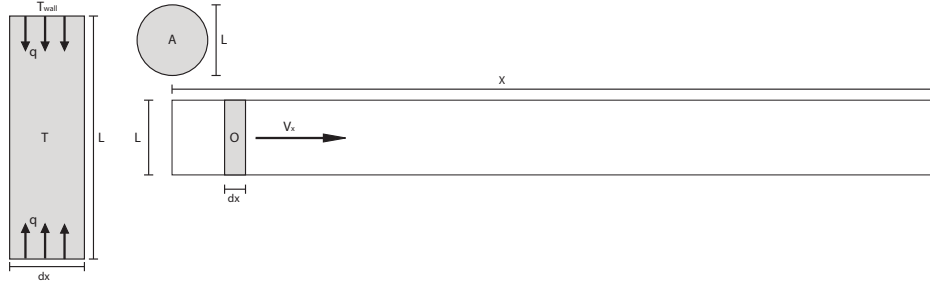
The heat generated by the electrical heating element has to be transferred to gas that is flowing through the tube beneath it. We assume that the heat generated in the heater creates a uniform temperature in SiRN channel walls which is transferred by convective heat transfer to the gas as the Biot number for the walls where the methane flows along is  $8.34 \cdot 10^{-5}$  and for the walls with the air flow  $1.14 \cdot 10^{-4}$ . With this assumption we can approximate the model of the tube as a circular fluid heater and we assume that all the heat flux from the heater at the top of the tube is equally distributed over the walls of the channel (figure 4.15). The heat of inside the air and methane is distributed by conduction through the gasses as the Prandtl number  $\approx 0.7$ .

The fluid flow along the wall of the tube creates a thermal and physical boundary-layer, the heat from the wall is transferred by means of convective heat transfer into the fluid which can be described by (3.2) as the Prandtl number is. The model parameters for heating of gas in a tube are given in figure 4.16, the figure shows a gas plug with the volume  $A \cdot dx$  which is travelling in the heater with a length of  $X$  with a travel speed of  $V_x$ . The heat transfer coefficient is given by (4.4) where the Nusselt number for circular pipes with a uniform surface temperature is  $Nu=3.66$  [51].  $O$  is the area with the width  $dx$  along circumference of the channel.

The heat flux  $Q_f$  is the heat flux to the fluid and is described in equation 4.5. As we made the assumption that the heat flux through the wall was equally distributed we use for the thermal resistivity of the SiRN layer also for the area  $O$ . The thermal resistance of the convection is a factor  $10^5$  bigger than the thermal resistance of the SiRN layer. By combining equation 4.4, 4.5 and 2.1 we get 4.6 with  $r$  the radius of the channel.



**Figure 4.15:** The heat flux  $Q_f$  which is generated in heater is carried through the SiRN to the fluid inside the channel. As the thermal conductivity of the SiRN is much higher than the convective heat transfer we can assume an equal heat flux distribution from the heater over all the channel walls.



**Figure 4.16:** Parametric description of gas heating in a tube. On the left is a model gas heated by the walls and on the right the tube with the gas model in it. On the top the cross-section view of a tube can be seen.

$$h = \frac{k_f}{L} Nu \left[ W/m^2 \cdot K \right] \quad (4.4)$$

$$Q_f = \left( \frac{1}{\frac{1}{h \cdot O} + \frac{x_{SiRN}}{k_{SiRN} \cdot O}} \right) (T_{heater} - T_{fluid}) [W] \quad (4.5)$$

$$\begin{aligned} \frac{dT_{fluid}(t)}{dt} &= \frac{Q_f}{\rho \cdot V \cdot C_p} [K/s] \\ \frac{dT_{fluid}(t)}{dt} &= \frac{\frac{1}{\frac{1}{h} + \frac{x_{SiRN}}{k_{SiRN}}} \cdot dx \cdot 2\pi r (T_{heater} - T_{fluid}(t))}{\rho_f \cdot A \cdot dx \cdot C_{p,f}} [K/s] \\ \frac{dT_{fluid}(t)}{dt} &= \frac{\frac{1}{\frac{1}{h} + \frac{x_{SiRN}}{k_{SiRN}}} (T_{heater} - T_{fluid}(t)) \cdot 2}{\rho_f \cdot r \cdot C_{p,f}} [K/s] \end{aligned} \quad (4.6)$$

We are interested in the temperature of the gas as it exists the heater. This temperature can be calculated by assuming that the tube has a uniform temperature and that the time for heating the gas is given by  $t = \frac{X}{V_x} = \frac{X \cdot A}{\varphi_V}$ . This makes the heating of the plug flow position independent and transforms the gas plug into a stationary object that is heated over the time  $t$ , the temperature can be found by rewriting (4.6) to (4.7) with  $c_1$  as constant. We can find  $c_1$  by defining the boundary condition at  $T(0)$ . Equation 4.8 gives a time independent description and shows that decreasing the radius of the tube results in faster heating of the fluid. As expected with an increase of the volumetric flow speed  $\varphi_V$  the time-constant decreases which results in a slower heating of the fluid.

$$T_{fluid}(t) = T_{heater} - (T_{heater} - T_{fluid}(0)) \exp \left( - \frac{2 \cdot \frac{1}{\frac{1}{h} + \frac{x_{SiRN}}{k_{SiRN}}} \cdot t}{\rho_f \cdot C_{p,f} \cdot r} \right) [K] \quad (4.7)$$

$$T_{fluid} = T_{heater} - (T_{heater} - T_{fluid}(0)) \exp \left( - \frac{2\pi r \cdot X \frac{1}{\frac{2r}{3.66k_f} + \frac{x_{SiRN}}{k_{SiRN}}}}{\rho_f \cdot C_{p,f} \cdot \phi V} \right) [K] \quad (4.8)$$

By using equation 4.8 the nominal air flow gas temperature can be calculated through 2 parallel double buried channel. It will reach the auto-ignition temperature of 853.15K with a wall temperature of 873.15K in 1.0 mm. This requires a thermal flux of 934,257 W/m<sup>2</sup> m through the surface of the cylindrical channel which results in a heating power of 0.17W for the cold gas at the inlet. For a single double buried channel with a nominal methane flow a length of 0.35mm is required with a thermal flux of 1,280,409 W/m<sup>2</sup> through the surface of the cylindrical channel which results in a heating power of 0.08W. Channel lengths longer than the calculated above further increase the gas temperature but to achieve 873.15K inside the gas with the same wall temperature an infinite long length is needed as the heat transfer is described by an exponential function. The thermal flux through the SiRN gives a  $\Delta T$  of 0.1K over the SiRN layer which makes it negligible in comparison with the temperature drop caused by the convection.

### 4.3.2 Electrical heating

As we are going to use electrical heating we also need a material that is suitable for acting as heater. Due to the high operating temperature range (873.15K-1100K) many materials are not suitable for the design but there are a few choices that have a high melting point, a low specific resistance and a low oxidation rate. The metal platinum (Pt) is a suitable candidate and has a positive temperature coefficient which makes it ideal for temperature sensing. The semiconductor tin dioxide doped with antimony (SnO<sub>2</sub>:Sb) can also be used as a heater [52]. The platinum and tin dioxide show a high temperature stability where platinum starts to fail at 1100K and tin dioxide at 1300K. The process for creating the semiconductor requires a doping implantation which means a few extra steps in the processing as this was not included in the original micro-coriolis process flow, this makes the choice for the tin dioxide less favourable.

The adhesion of noble metal like gold and platinum onto a substrate requires most of the time an adhesion layer to improve the poor adhesion caused by the chemical inertness. These adhesion layers have a typical thickness of 10-20 nm and have as downside that these layers start to melt at the high temperatures. There are a few combinations know that can endure these high temperatures such as Ti/Pt which has a linear thermal resistivity up to 973.15K [53] and Ta/Pt which goes up to 1073.15K [54]. There is also a possibility to adhere platinum on SiRN without an adhesion layer by roughing of the SiRN surface, this roughing also removes the contamination that is on the SiRN surface and is suitable up to a temperature of 1223.15K [54, 55, 56].

Platinum presents it self as a suitable material for our working range and is easy to incorporate into the existing process flow and will be deposited without an adhesion layer with only roughed SiRN as adhesion promoter.

Heating of SiRN with a heater on top of it will induce thermal stress between the layers. This stress will result in a deflection in the case of proper adhesion between the layers. The deflection for a 150 nm platinum layer on top of a 2200 nm SiRN layer will give downwards curvature as the platinum has an thermal expansion coefficient which is a factor 2.67 larger than SiRN. Calculating the resulting curvature with (3.38) gives a radius of  $1.6 \cdot 10^{-3}$ m at a temperature of 873.15K with compressive stress in the silicon nitride layer. The buried channels have a larger second moment of inertia than a plane SiRN layer which results in an approximate curvature radius of 2.5 m.

### Power without losses

Heating with an ohmic heater requires a current for the energy transport to the heater. The maximum current transported through the heater is given by the current density in  $A/cm^2$  and is given in (4.9) with  $\rho_{ohm}$  as the specific electrical resistance of the metal. A current density in the range of  $10^5$ - $10^7$   $A/cm^2$  will form hill-locks and structural damage caused by electromigration. The electromigration effect is highly structure and metal dependent and measurements have to prove the threshold value of electromigration inside the designed platinum heaters.

$$\phi_\rho = \frac{i}{A \cdot 10^4} = \sqrt{\frac{P}{\rho_{ohm} \cdot l \cdot w \cdot h}} \frac{1}{10^4} \left[ A/cm^2 \right] \quad (4.9)$$

To prevent the electromigration effect the heaters have to be designed with the maximum current density below the threshold. By rewriting (4.9) to the required heater height as function of the current density gives the value in table 4.7 for a heater that delivers 0.17W and covers 50% of a channel with a length of 1 mm and a width of 80  $\mu m$ . This shows that the electromigration effect probably starts at a layer thickness of 40.4  $\mu m$ . However deposition such thick layers is not practical, another solution would be increasing of the resistance of the tracks through increase of the length but that only scales with  $\sqrt{1/l}$  or steering the heater with a voltage where the current is limited as the power is given by  $P = U \cdot I$ .

Current density [ $A/cm^2$ ]	platinum layer height [ $\mu m$ ]
$10^4$	$4.047 \cdot 10^{-3}$
$10^5$	$4.047 \cdot 10^{-5}$
$10^6$	$4.047 \cdot 10^{-7}$
$10^7$	$4.047 \cdot 10^{-9}$

**Table 4.7:** The required platinum layer height for the given current density for an 1 mm by 40  $\mu m$  heater with a power of 0.17W.

The metal layer thickness used for the micro-coriolis is around the 150nm, this would give for a track width of 8  $\mu m$  the current densities shown in table 4.8. By steering with 20V and limiting the current to 8.5 mA a power of 0.17W is delivered to the heaters which gives a current density of  $7 \cdot 10^5$ . This is far from ideal and tests have to show if the electromigration will pose a problem. The origin of why this is used for the design will be further evaluated in the discussion.

Design	Length [mm]	Resistance [ $\Omega$ ]	Current density [ $A/cm^2$ ]	Current needed for 0.17W [mA]
Square	5	430	$1.6 \cdot 10^6$	19.7
Circular (2)	10	875	$1.1 \cdot 10^6$	13.9
Circular (3)	15	1312	$9.4 \cdot 10^5$	11.3

**Table 4.8:** The specification of the heaters for the square core design and the circular core with 2 and 3 heaters in series.

### Power with losses

With (3.1),(3.2), (3.3), (3.5) and the relation  $P = i^2 R$  we can derive the energy balance for a heater which is given in equation 4.10. The power needed for the heating of air had the highest value of all heaters with 0.17W. The thermal resistance of the platinum layer is a factor 80 smaller than the underlying SiRN layer so we can assume a constant temperature inside the material of the heater and the thermal resistance of the SiRN wall can be neglected. The SiRN top has an area  $A$  of  $8.0 \cdot 10^{-8} m^2$  at top of the buried channel, for more realistic results the total outside area of the channel has to be used. For  $T_{inf}$  we use 298.15K and  $A=8.0 \cdot 10^{-8} m^2$  with  $h_{gas}=1708.42 W/m^2 \cdot K$  and  $A_{channel} = 1.67 \cdot 10^{-7} m^2$ . This results for a temperature of 873.15K in a current of 19.5mA at 8.5V which is again 0.17W of power which is

dissipated. The current increases for compensation of the losses but the resistance increases also with the temperature which results in nett the same power as with no-losses.

$$P(1 + \alpha(T - T_0)) = h_{gas}(T_{inf} - T)A_{channel} + A \cdot (h_{ave} \cdot (T_{inf} - T) + \epsilon \cdot \sigma(T_{inf}^4 - T^4)) \quad (4.10)$$

The relation of the temperature versus the power is shown in figure 4.17 which shows a linear power to temperature relation. For the design the current was limited for the heater, regulating the heater with the voltage will give also a linear relation with the temperature as is shown in figure 4.18.

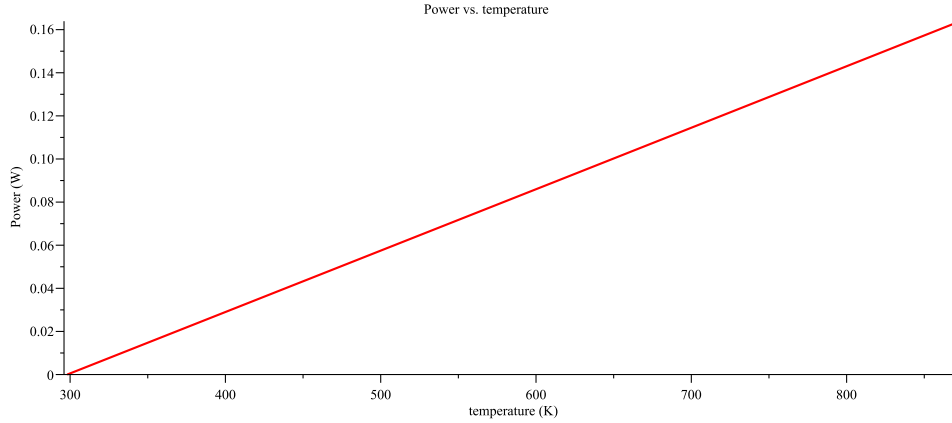


Figure 4.17: The temperature versus the needed power.

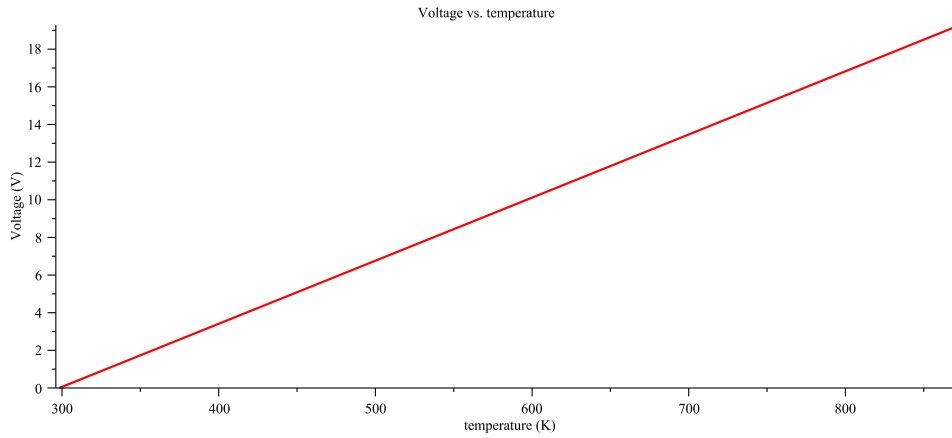


Figure 4.18: The temperature versus the needed voltage at fixed current of 8.5 mA.

## 4.4 Core

A cross-section of the chip is shown in figure 4.19. The core in the centre of the figure is thinned out to a value of 100  $\mu\text{m}$ . With this thin core we can obtain a high heating resolution of the heating value and this also prevents a possible collapse of the core on the underlying structure due to thermal expansion. The core is isolated from the rest of the wafer by a trench with a width of 1 mm. The only connections to the core are the suspension beams and the fluid channels. The suspension beams are made of SiRN channels as silicon beams would conduct the heat 5.5 times faster than the SiRN. Furthermore the cylindrical structure of the channels have a higher second moment of inertia in comparison with rectangular silicon beams with the same cross-sectional area.

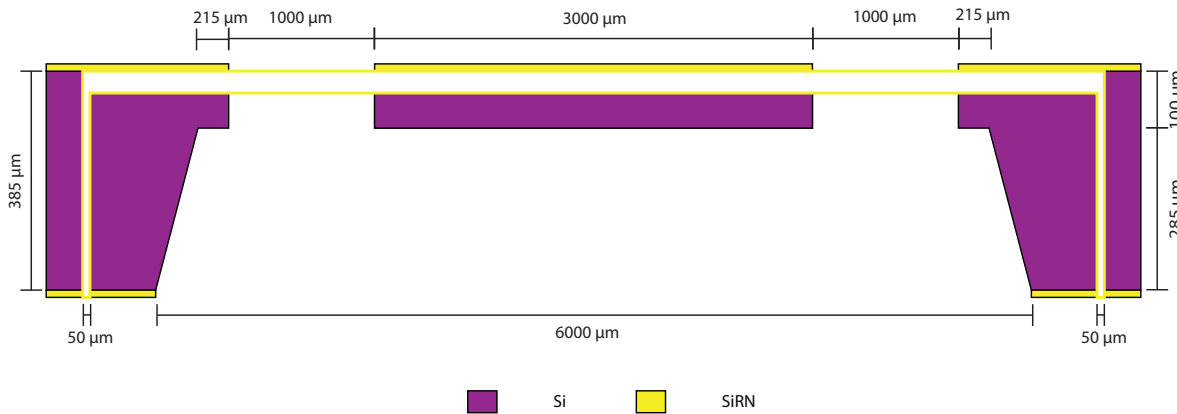


Figure 4.19: A cross-sectional view of the chip.

The process of creating a straight trench through the whole wafer is more difficult to realize in comparison with thinning of the wafer and trenching it afterwards. Choosing for 380  $\mu\text{m}$  thick wafers instead of the standard 525  $\mu\text{m}$  reduces the production time of thinning and wafer through etching with a factor 1.5.

The core of the chip consist of a silicon bulk with buried channels in its top and a layer of SiRN with platinum heaters on it. By using silicon as bulk material an iso-thermal core can be created. Due to the small dimensions the core will react quickly with a small time-constant to heat changes. The area of the core was defined by the thermal loss through radiation as that is the most dominating heat loss at operating temperature. The dimensions are shown in table 4.9 for both designs. An extra heater is added on the top of the core which enables the possibility for doing thermal calibrations and calorific measurements through thermal balancing. The heater has build out of 8 parallel tracks with a width of 10  $\mu\text{m}$  with each a length of 37.5 mm. This gives for a 1 J/s dissipation a current density of  $4.6 \cdot 10^5 \text{ A/cm}^2$  with a current of 55 mA at a voltage of 18.1 V. With voltage control at 20V and a fixed current of 50mA a current density is reached of  $4.1 \cdot 10^5 \text{ A/cm}^2$ .

Property	Square	Circular
Dimensions	$3 \cdot 10^{-3} \cdot 3 \cdot 10^{-3} \cdot 100 \cdot 10^{-6}$	$\pi \cdot (1950 \cdot 10^{-6})^2 \cdot 100 \cdot 10^{-6}$
Mass	2.2 $\mu\text{g}$	2.8 $\mu\text{g}$
Top area	9 $\text{mm}^2$	11.9 $\text{mm}^2$
Joule for 1K increase [J]	$1.49 \cdot 10^{-3}$	$2.0 \cdot 10^{-3}$
Temperature increase at 1J [K]	669.11	488.65

Table 4.9: The thermals of the cores of the two designs.

The SiRN channels are grown into the silicon bulk which fixes the channels in the silicon. Thermal heating will create layer stress at the boundary of the SiRN and silicon. The channels are entangled with the top 35  $\mu\text{m}$  silicon of the bulk which makes it impossible to calculate the stresses in the core without the use of simulations. The linear thermal expansion coefficients between the silicon and SiRN differ  $0.81 \cdot 10^{-6} \text{ m}/(\text{m} \cdot \text{K})$  which results for a heated core of 1100K SiRN in a length difference of 649  $\mu\text{m}/\text{m}$ . From the magnitude of the number we can conclude that at the temperature of 1100K the 3 mm width bulk with SiRN top layer will have a length difference of 1.9  $\mu\text{m}$  which results in a compressive stress in the silicon bulk. The thermal expansion coefficient has also a temperature dependency which decreases with the increase of the temperature, this will influence the expansion and results in a smaller length difference.



#### 4.4.1 Mechanics

For the purpose of thermal isolation the core is connected with SiRN beams to the rest of the wafer. These beams act as springs which will deflect in the z-direction under influence of gravity acting on the mass of the core can be described with equation 3.34. The thermal heating of the beams will also result in expansion of the beams. There are two variates in the design of the suspension for the core of the chip. The first variety has four set of three parallel L-shaped beams, three double channel gas inlet channels and one triple channel outlet. The second variety has S-shaped beams which ends parallel with the surface of the core and wafer. This design has 18 beams which are equally radial distributed. The core has seven inlets and five outlets. All the beams in this design are single channels. The two designs are shown in figure 4.20 and the suspension beam dimensions are given in table 4.10.

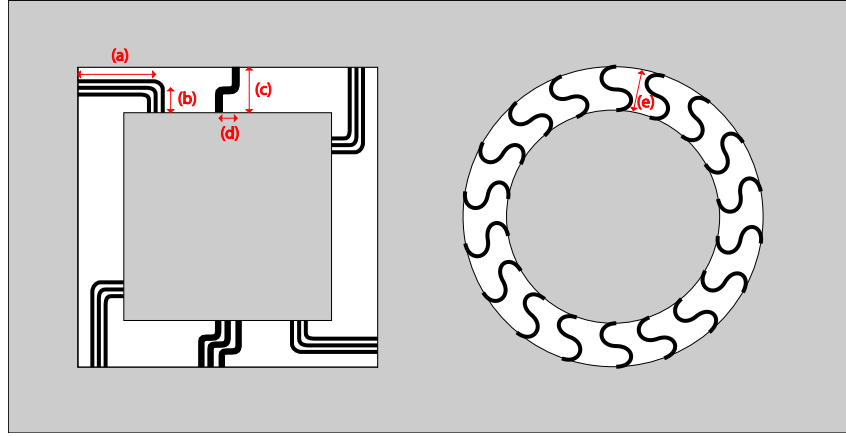


Figure 4.20: The suspension of the two chip variations with the values of (a)-(e) in table 4.10.

Design	(a) [ $\mu\text{m}$ ]	(b) [ $\mu\text{m}$ ]	(c) [ $\mu\text{m}$ ]	(d) [ $\mu\text{m}$ ]	(e) [ $\mu\text{m}$ ]	total length [ $\mu\text{m}$ ]
L-shape	1575	365	-	-	-	1825
L-shape gas in/outlets	-	-	1000	575	-	1320
S-shape	-	-	-	-	1000	1595

Table 4.10: Dimension of the suspension beams.

The L beams will experience a torsion stress which can be calculated with (3.37), however the displacement at the end of the arm (b) caused by torsion will be reduced by the parallel placement of the beams to a minimum, the exact value has still to be calculated.

An approximation of the deflection of the square core can be given by the bending over the average length (a) of the L-shaped beams and can be calculated with equation 3.34. The spring constant for the deflection can be modelled as 12 parallel beams with a shared load on the end of the beams which is formed by mass of the core. The inertia can be described with (3.35) where a single beam can be described by a  $2.2 \mu\text{m}$  thick slab with a width of  $80 \mu\text{m}$  on top of a cylinder with an external diameter of  $40 \mu\text{m}$  and an internal rim of  $1.4 \mu\text{m}$ . This gives an  $I_{xx}$  of  $6.65 \cdot 10^{-20}$  and an  $I_{yy}$  of  $12.55 \cdot 10^{-20}$  and a downwards deflection of  $119 \text{ nm}$ .

The L-beams and square core will also expand due to thermal heating where the expansion will cause a clockwise rotation of the core. As the beams are made of SiRN the compressional effect in the silicon layer of the core will bend the core upwards which reduces the deflection in the centre of the core. The thermal layer stress of the platinum heaters and tracks on the SiRN beams will deflect the beams with a maximum of  $0.6 \mu\text{m}$  downwards. The total deflection in the z-direction of the core with L-beams due to gravity and heating will be around the  $1 \mu\text{m}$ . This is without the influence of the spring constant of the gas in-/outlets which will further reduce the deflection of the core.

The deflection of the circular core with S-beam is a combination of torsional and linear bending. The deflection has to be simulated but we expect that the deflection will be of the same magnitude as the L-beams. The thermal expansion of the core and the beams will cause a minimal rotation as the expansion is minimized by the shape of the beams and the parallel entering into the surface of the core and the wafer.

#### 4.4.2 Thermal loss

The chip is a dynamic system as it is composed out of sources; heaters, combustion and losses; conduction, convection, radiation and heat storage; the thermal capacity of the material. We can find the end temperature of the dynamic system by modelling it with a finite element simulation but the small feature sizes of channels makes it almost impossible to do this. A more coarse approach would be dividing the different parts in lumped elements as is shown in figure 4.21.

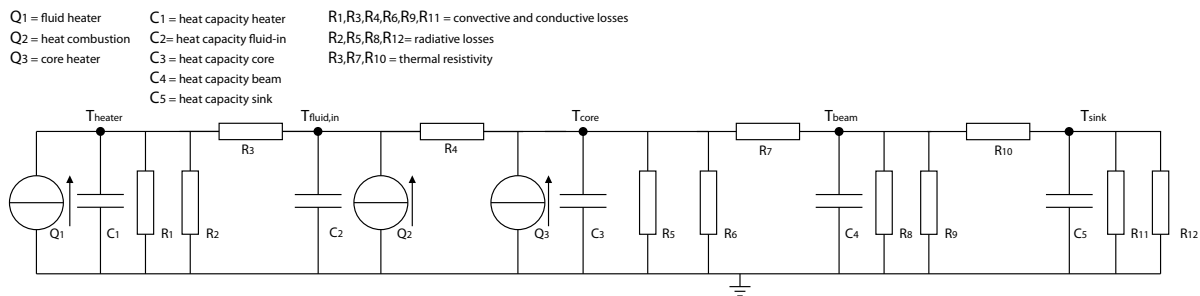


Figure 4.21: Network description of the thermodynamics.

The heat from the heater is transfer by convection to the fluid which flows towards the core. In the ideal case the combustion will cause an iso-thermal heat distribution in the core. The heat flux that is released from the combustion will be transferred by means of convection into the SiRN channel walls. The channel walls will give a negligible temperature drop and conduct the heat flux into the silicon bulk which surrounds the channels. In table 4.9 we gave the temperature increase of the core per joule of heat but the end temperature is determined by the total thermal loss. These losses are caused by conduction, convection and radiation and are drawn in a sketch of the core in figure 4.22. The wafer (sink) is connected to an external heat sink which is kept at ambient temperature due to its dimensions. The thermal contact resistance of the interface between the wafer and chip is for our purpose infinitesimal.

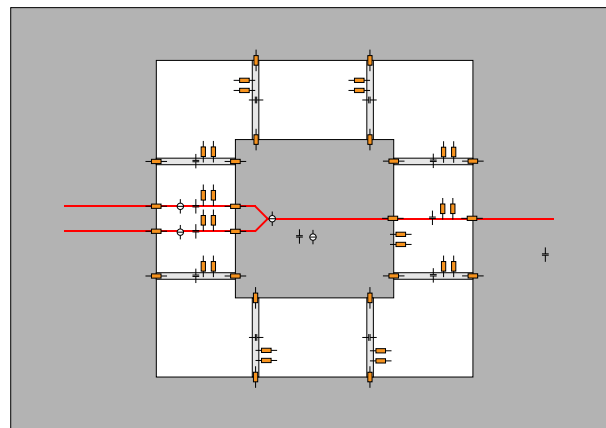


Figure 4.22: The chip with the thermal losses, thermal capacities and thermal sources.

Calculations made with (3.1),(3.2),(3.3) and (3.4) give for the core with L-shaped beams a thermal loss as shown is in figure 4.23. This gives for a total dissipation of 1 Joule in the core a temperature of 1081.49K.

The S-shaped design use 12 of the 18 beams for fluid transport which eliminate them for the pure purpose of heat flux transport from the core to the sink. This gives for a total dissipation of 1 Joule a temperature of 1014.8K. The S-shaped design losses more heat flux through radiation as the surface area of the core is 11.9mm<sup>2</sup> which is larger than the square core of 9mm<sup>2</sup>.

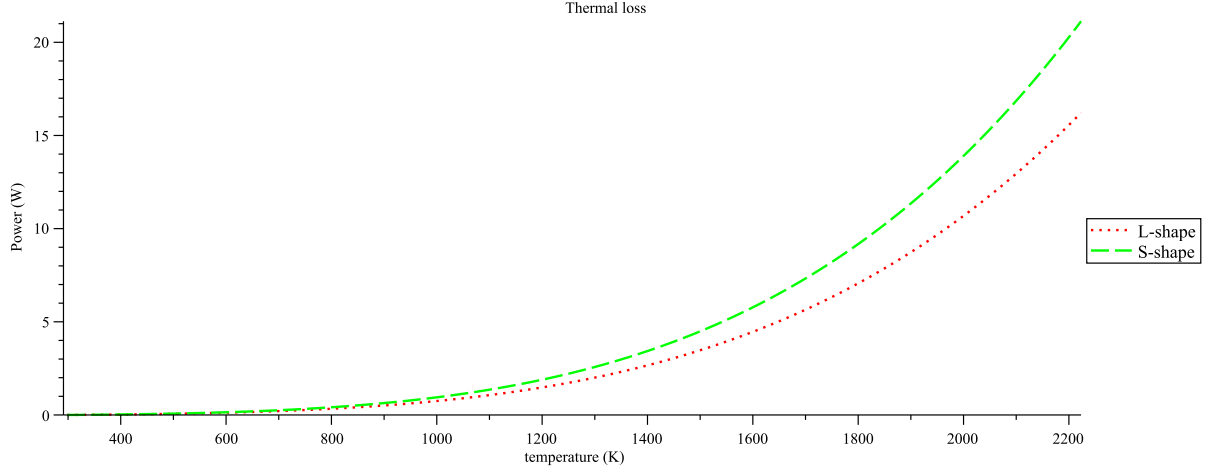


Figure 4.23: The thermal flux versus the temperature.

The core would not only loses thermal flux by means of conduction, convection and radiation but also through the transport of the gas out of the core. The cooling down of the combustion gas happens by convective heat transfer to the core and this transfer is dependent on the temperature gradient. This causes a dynamic relation between the heat flux out of the gas into the core (4.11) and the heat flux transport by gas out of the exhaust, this makes the heat flux position dependent. As the core will approach an iso-thermal temperature the heat transport from the gas to the core will approach a stable point where after the heat flux of the combustion products to the core and from the combustion products to the exhaust can be approached as a constant energy flux. However this is only valid for a continuous and stable combustion. An estimate of the heat transfer coefficient, calculated with (3.19), for the gas mixture of 78.09% N<sub>2</sub>, 0.97% Ar, 13.96% H<sub>2</sub>O and 6.98% CO<sub>2</sub> at 2232K gives  $h=17199 \text{ W}/(\text{m}^2 \cdot \text{K})$ .

$$\begin{aligned}
 Q_{\text{gas} \rightarrow \text{core}} &= \frac{1}{\rho_{\text{core}} \cdot V_{\text{core}} \cdot C_{p,\text{core}}} \frac{dT_{\text{core}}}{dt} + \text{convection} + \text{conduction} + \text{radiation} = \\
 &= h \cdot (T_{\text{gas}} - T_{\text{core}}) \\
 &= -\frac{1}{\rho_{\text{gas}} \cdot V_{\text{gas}} \cdot C_{p,\text{gas}}} \frac{dT_{\text{gas}}}{dt} \quad (4.11)
 \end{aligned}$$

The dynamic system of the heating fluxes and a steady heat source can also be described with a bond-graph which is given in figure 4.24. The resulting temperature of the simulation is given in figure 4.25, this shows that the system has a start-up time of 4 seconds and a final temperature of 1080K.

The reference standard for calorimetry states that the exhaust gasses need to be on the same temperature as the gas that goes into the system to prevent an energy flux which says that the thermal capacity of the gasses that go in the calorimeter has to be the same as the gas that goes out of the system to prevent an energy flux. The thermal energy stored in a mass can be obtained by rewriting (2.1). The thermal balance is given in (4.12) where we ignore the unchanged inert gasses that go in and out of the system and  $\frac{RT}{p} = \text{constant}$ .

$$\begin{aligned}
 E_{\text{CH}_4} + E_{\text{O}_2} &= E_{\text{H}_2\text{O}} + E_{\text{CO}_2} \\
 \frac{RT}{p} (\rho_{\text{CH}_4} \cdot X_{\text{CH}_4} \cdot C_{p,\text{CH}_4} + \rho_{\text{O}_2} \cdot X_{\text{O}_2} \cdot C_{p,\text{O}_2}) &= \frac{RT}{p} (\rho_{\text{H}_2\text{O}} \cdot X_{\text{H}_2\text{O}} \cdot C_{p,\text{H}_2\text{O}} + \rho_{\text{CO}_2} \cdot X_{\text{CO}_2} \cdot C_{p,\text{CO}_2}) \quad (4.12)
 \end{aligned}$$

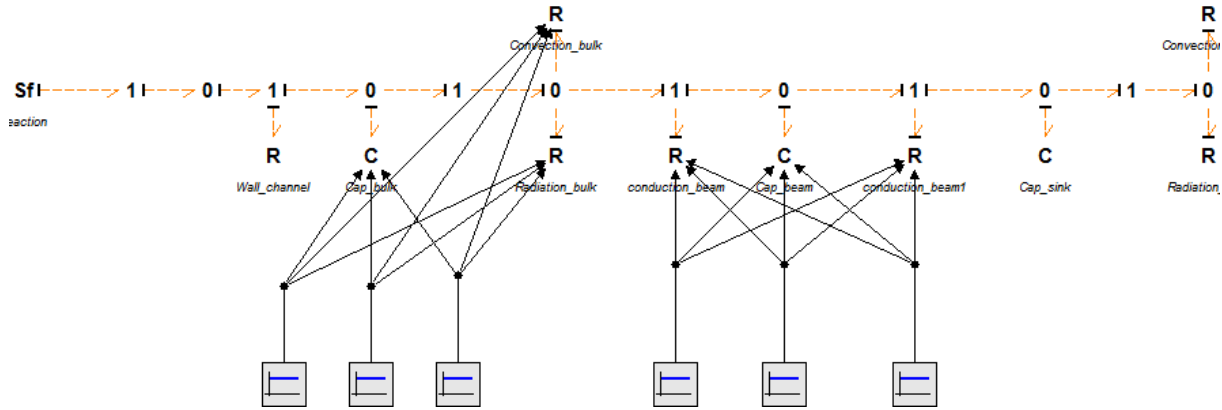


Figure 4.24: The bond-graph of the combustion which is modeled as a steady heat source.

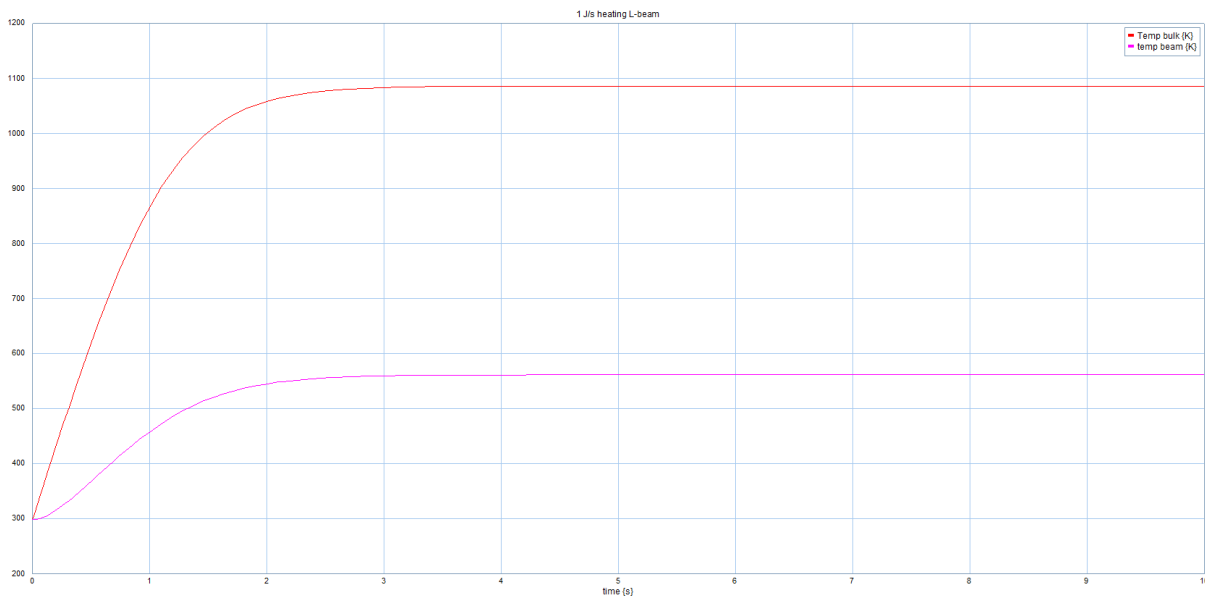


Figure 4.25: The simulated bond-graph combustion which shows the temperature of the core and temperature measured by the sensor.

By using the values out of table A.3 we get the result (4.13). This shows that the thermal energy that can be stored in the gas before the reaction is lower than after the reaction which causes a nett flux. To prevent a flux we have to add extra heaters at the exhaust to regulate the exit temperature or increase the temperature at the inlet. This can also be seen as a thermal loss which can be added in the thermal calculations.

$$0.656 \cdot \frac{1}{3} \cdot 2237 + 1.308 \cdot \frac{2}{3} \cdot 918 = 0.9970 \cdot \frac{2}{3} \cdot 1865.11 + 1.799 \cdot \frac{1}{3} \cdot 850 [J]$$

$$1289.65 \neq 1749.39 [J] \quad (4.13)$$

#### 4.4.3 Temperature measurement

The temperature of the core has to be measured to obtain the calorific value of the combusted gas. The surface of the core is covered with an additional heater which is used for creating a heat balance which leaves no room for a temperature sensor, this creates the necessity that the temperature is measured at a different spot. The thermal resistance of the suspension beam has a linear relation with the thermal

flux which results in a linear temperature drop over the beam with an minor loss due to the convective and radiative transfer from the surface of the beam. This linear relation can be used to measure the temperature of the core with the assumption that the core is iso-thermal. The temperature is given by the position with the relation:






$$T_{measured} = \frac{x}{beam_{end} - beam_{base}} \cdot (T_{core} - T_{base}) + T_{base} \quad (4.14)$$








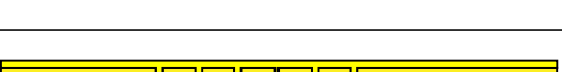
The sensing element covers a certain length on the beam which causes a gradient over the element and results in a measured temperature of  $T_{average} = \frac{T_{max} + T_{min}}{2}$ . This is the same temperature as the point in the centre of the element. By making use of the thermal resistance coefficient of platinum the temperature can be measured with the resistance change. The resistance change will be measured with a 4-point measurement where the steering current through the element will give a voltage drop over the sensing element which is linear related to the temperature as is given in equation 3.5.




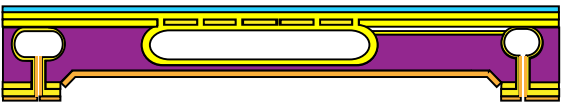
The sensing element is 200  $\mu m$  long and is located on 0.45 of the length the beam which gives an average measured temperature of  $T_{average} = 0.45 \cdot (T_{core} - T_{base}) + T_{base}$ . The element has a serpentine lay-out and is 4  $\mu m$  wide, 1644  $\mu m$  long and has a resistance of 287  $\Omega$  at 298.15K. The resistance change is a 1.07  $\Omega/K$  which gives a resolution of 1.07mV/K at a current of 1mA. In the case that the core reaches its maximum temperature of 1080K this results in a  $T_{measured}$  of 650K which gives  $\Delta V = 352mV$ . An increase in resolution can be achieved by use of a lock-in amplifier which is less sensitive to the thermal noise.




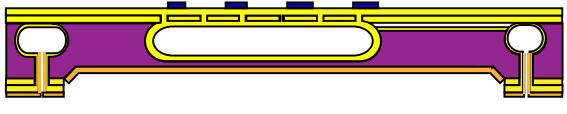

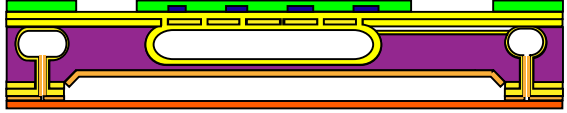


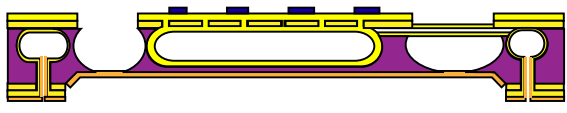
## 4.5 Process flow

For the realization of the chip inside the cleanroom a process flow is needed. This process flow determines the masks that are needed for creating the structures on the wafer. The following materials are needed for creating the structures: silicon as base material of the sink and bulk, SiRN as the base material for the channels and the platinum as the base material for the heaters. The fabrication of the chip design requires a process flow which stepwise describes the processes that have to be executed. A summary of the process flow is given in table 4.11 and the complete process flow can be found in appendix C.1.


Step	Process flow steps	Process description	Cross-section after process
<u>Wobbe part-1</u>		<u>Channel fabrication</u>	
0.	1	Bare <100> wafer	
1.	2-13	LPCVD of SiRN	
2.	14-22	Spinning backside SU8 2005 (neg) <b>Litho: Access-holes</b>	
3.	23	Etch through SiRN	
4.	24	DRIE (Dry reactive ion etch) etch through Si	

5.	25-39	SU8 removal with Piranha	
6.	40-48	Deposition TEOS	
7.	49-54	Dicing foil backside Removal frontside TEOS (BHF)	
8.	55-62	Sputtering Chromium	
9.	63-71	OiR 907-17 spinning (pos) <b>Litho: Channel</b>	
10.	72-76	Etch through Chromium (critical: slits $\leq 2.0 \mu\text{m}$ )	
11.	77-78	Etch through SiRN	
12.	79	Isotropic etch through Si	
13.	80-84	Removal OiR 907-17 Removal Chromium	
14.	85-88	Removal TEOS	
15.	89-99	Growing SiRN layer inside and outside channel (grow $1.7 \mu\text{m}$ SiRN)	

Wobbe part-2		Core	
16.	1	Apply MX 5020 litho foil backside (neg)	
17.	2	<b>Litho: KOH</b>	
18.	3	DRIE etch backside SiRN (~2.3 um)	
19.	4	Removal MX5020 foil	
20.	5-16	Backside KOH etch: 425-475 um deep	
21.	17	Growing TEOS masking layer (PCVD) (TEOS grows also in the channel)	
<b>Heaters</b>			
22.	18-20	backside dicing foil Etch TEOS frontside (BHF)	
23.	21-30	Roughing up the frontside SiRN layer with etching	
24.	31	Sputtering Platinum layer	
25.	32-33	Spinning frontside OiR (pos)	

26.	34-40	Litho: Metal mask	
27.	41	Oxidizing platinum	
28.	42	Removal OiR	
29.	43-51	Wet etching platinum	
<u>Isolation of the core</u>			
30.	52-54	Spinning frontside OiR (pos)	
31.	55-62	Apply MX5020 foil on backside <b>Litho: Front-release</b>	
32.	63-64	DRIE etch frontside SiRN	
33.	65-66	Isotropic etch frontside Si (TEOS is stopping layer) with on the backside MX 5020 foil Backup: Xef2 etching (gives roughness) with on the backside MX 5020 foil	
34.	67-69	Frontside OiR removal MX5020 foil removal	



35.	70-73	TEOS removal	
36.	74	Breaking of the wafer	

**Table 4.11:** A summary of the process flow which is given in appendix C.1.

The flow starts with a bare double side polished <100> wafer with a thickness of 385  $\mu\text{m}$ . It is also possible to start with a 525  $\mu\text{m}$  wafer but the decreased thickness saves time at creating the access-holes and the KOH pit. The doping of the wafer is not of importance for the device.

In step 1 a SiRN 500 nm layer is grown on the wafer which covers both sides of the wafer. This SiRN layer acts of masking layer for the buried channels.

In step 2 and 3 the pattern for the access-holes are created at the backside of the wafer by means of lithography on a 5.2  $\mu\text{m}$  layer of SU8-2005 photoresist. The choice for SU-8 2005 is based on its ability to resist cryogenic temperatures of  $-100^\circ\text{C}$ , its straight sidewalls and easy creation of thick layers for protection against the ion bombardment from the DRIE Bosch etching. As the processing is done at  $-100^\circ\text{C}$  the choice is made for SU-8 2005, other photoresists would crack at that temperature [57].

In step 4 the access-holes are created by etching with a DRIE Bosch process. The Bosch process creates vertical channel through the wafer with pulsed etching. The alternating between  $\text{SF}_6$  and  $\text{CHF}_3$  enables the etching of silicon with  $\text{SF}_6$  and the protection of the etched wall with  $\text{CHF}_3$ . This process creates a rippled channel until the SiRN layer at the frontside of the wafer is reached.

In step 5 the SU-8 2005 photoresist is stripped of the wafer with Piranha and the protective fluorocarbon layer in the access-holes is stripped with HF 1%.

In step 6 the access-holes are covered with a 1100 nm layer of TEOS to prevent an open connection between the back- and frontside of the wafer in the iso-tropic channel etching in step 12.

In step 7 the TEOS of the frontside is removed with BHF while the backside is protected by a layer of dicing foil.

In step 8 to 11 a 50 nm layer of chromium is applied on the frontside of the wafer. This chromium layer acts as patterning material for the channel slits. By using this chromium layer the channel slits will have the same size on the SiRN and the layer acts as protective layer against the isotropic etching, photoresist holes will increase in size during the etch where in comparison the chromium will retain the same size. The chromium is covert which an OiR 907-17 photoresist which is patterned with the channel mask and after the patterning the chromium is etched. It is important that the channel slits in the chromium are below the 2.1  $\mu\text{m}$  because larger slits require a longer SiRN growing time for a closed channel. When the layer of SiRN on top of the silicon gets to thick ( $>2.6 \mu\text{m}$ ) the stress between the silicon and SiRN layer increase which will result in broken chips.

In step 12 the isotopic etching of the silicon underneath the SiRN layer is done and by breaking of a dummy wafer the channel width and height can be verified.

In step 13 and 14 the chromium and the TEOS layers are removed. The chromium with a layer photoresist on it is stripped and after removal of the TEOS there is an open connection between the front- and backside of the wafer.

In step 15 the layer of SiRN is grown in the channels. The layer thickness is dependent on the final slits width after the stripping in step 14. The thickness is calculated by using half the slit width with 10% over-deposition. The over-deposition ensures the complete closure of the channels.

In step 16 Dupont MX5020 foil is used as masking layer for the KOH pit. The Dupont MX5020 foil was never used before in Mesa+ for lithographic processes. This requires the development of a new process-flow, this process flow will be described in the next section. With this foil the access-holes could be covered without spilling of photoresist inside the channels or creating thin spots at the corners of the access-holes when the photoresist flows in the channels. There are more polymer based masking foils available on the market with different material properties, however the Dupont MX5020 was chosen as it was available in the Mesa+ Nanolab. The KOH etch has to be done after the growing of the channels,

it could not be done as step 1 as the SU-8 2005 resist has to be spun on a flat wafer and as nothing is known about the thermal resistance against  $-40^{\circ}\text{C}$  of the spray-coated resist we do not use that method. The pit could not be etched after step 10 of the access-holes as KOH also etches TEOS at a slow rate.

In step 17 to 20 the masking pattern of the Dupont MX5020 foil is used for etching the SiRN and KOH pit. The patterns in the SiRN layer form the masking layer for the KOH pit. The KOH is etched along the  $\langle 100 \rangle$  and  $\langle 110 \rangle$  plane and will be stopped at the required depth. This etch will leave a pit with angled sidewalls.

In step 21 an 1100 nm layer of TEOS is grown to cover the pits. The TEOS will serve as etch stop at the release etch and will give extra rigidity and thermal conductivity until it is removed in the final step.

In step 22 the surface is prepared for the platinum by removing the TEOS from the frontside of the wafer.

In step 23 to 29 the platinum is deposited, patterned, oxidized and etched. The process of adhering platinum to SiRN without an adhesion layer needs to be verified which will be discussed in the coming section. This metal layer could not be included earlier in the process as metal layers are not allowed in the TEOS and SiRN furnace.

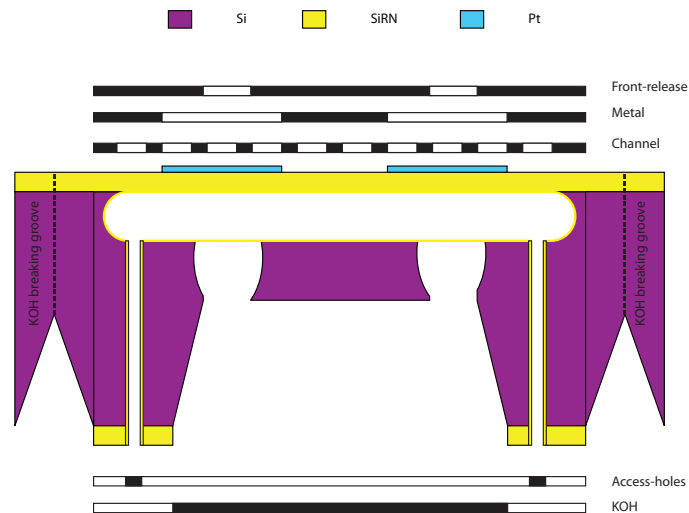
In step 30 to 34 the SiRN layer on the front side is patterned with OiR 908-35 and the release mask. The core is released with semi-isotropic etching, using anisotropic etching would result in silicon in the shade of the SiRN beams. The use of semi-isotropic etching results in a core with a smaller silicon bulk and the etching is stopped at the TEOS layer. If the semi-isotropic  $\text{SF}_6$  DRIE plasma etching would fail there is a back-up possibility of using  $\text{XeF}_2$ . The downside of etching with  $\text{XeF}_2$  is that the surface will have a rough grain structure. The trench around the core can also be etched from the backside of the wafer by patterning inside the pit. The patterning has to be done with a spray coated photoresist which is exposed by proximity lithography. This option allows the possibility to use anisotropic etching. Before the pit is etched the front SiRN layer has to be opened with a release mask which requires an additional masking plate in comparison with the semi-isotropic etching. This additional mask and the experimental state of the spray-coater is why this option is not used.

In step 35 to 36 the remaining TEOS layer is removed and the wafers are broken into single chips along the KOH V-grooves. We expect that dicing of the wafer would result in broken beams caused by the vibration of the dicing saw.

## 4.6 Mask design

For creating of the parts described in the foregoing section the features on the wafer have to be drawn as masks for the lithography. These masks are transferred by a mask writer to a glass with chromium plate. A positive mask will result in openings in the chromium at the drawn areas and a negative mask will be a transparent plate with chromium at the areas that were drawn. Each material layer needs one or more masks for creating these features, the resulting combination gives the chip shown in figure 4.26. There are five masks which are sorted in the order of production and have the following functions:

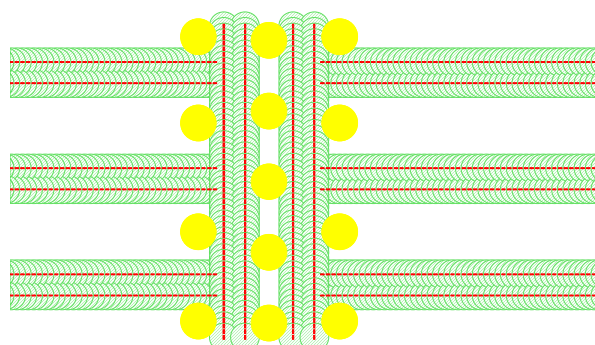
1. Access-holes: used for the DRIE etching of the access holes at the back of the wafer and is a negative mask
2. Channel: used for the buried channels pattern on the front of the wafer and is a positive mask
3. KOH: used for the KOH etch for thinning of the bulk at the back of the wafer and is a negative mask
4. Metal: used for the platinum layer on the front of the wafer and is a positive mask
5. Front-release: used for SiRN etching on the front of the wafer and releasing of the core and is a positive mask



**Figure 4.26:** A cross-section of the design.

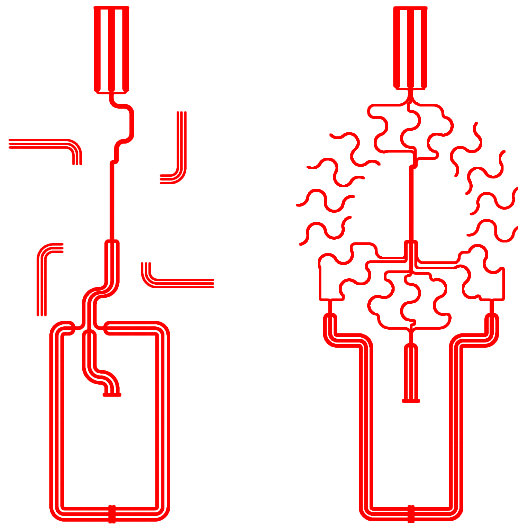
The first two masks are strongly related to each other; the access-hole facilitate the connections from the backside of the wafer to the channels that are in the frontside of the wafer. We use holes with a diameter of 50  $\mu\text{m}$ , the process of DRIE Bosch etching is already proven for these dimensions. To increase the total area we combined multiple holes for a single in-/outlet. The SiRN on the bottom side of the wafer is patterned with the access-holes mask and these are etched into the SiRN. With the SiRN etched the SiRN layer forms the pattern for the silicon DRIE bosch etching which is done until the SiRN layer on the frontside is reached.

The channel mask consists out of lines with repeating patterns of slits which have carefully to be aligned with the access-holes. No slits may lay on the access-holes, in the case this happens a slit will grow larger which complicates the closing of a channel. The average distance between the access-holes and the slits is 10  $\mu\text{m}$  with some exceptions of 8  $\mu\text{m}$ . In figure 4.27 an inlet with multiple access-holes is shown where the channels are connected to the access-holes. For creation of the channel slits patterns multiple LUA scripts for Clewin were written which automated the procedure, the scripts can be found in appendix B. The slits have a dimension of 1.5 by 5  $\mu\text{m}$ , a line width smaller than 1.5  $\mu\text{m}$  is almost impossible to write on the mask plates with the in-house maskwriter. The resulting channel design can be seen in figure 4.28.



**Figure 4.27:** The alignment of the access-holes relative to the channel-slits is critical. Access-holes are yellow, channel-slits are red and the fictive channels which are in a dummy layer are green.

The core is defined after etching and growing of SiRN for the channels by thinning of the wafer with the KOH mask. With the KOH mask openings are created in the SiRN layer of the backside of the wafer.



**Figure 4.28:** The channel patterns for both chip designs. The variations of the combustion channels are shown in figure 4.14.

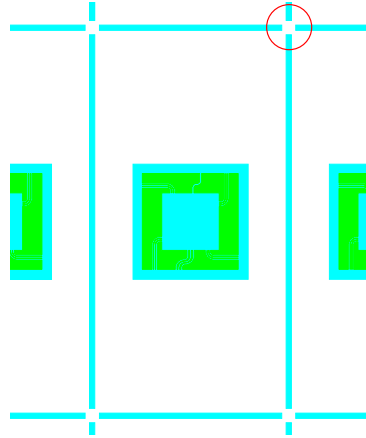
The etched SiRN patterns define the etching mask for the KOH pit as the KOH etchant will only etch the silicon layer. The pit is etched along the silicon crystal orientation under an angle of  $54.7^\circ$  from the surface to a depth of  $280\text{ }\mu\text{m}$ . To achieve the final dimensions of the thinned bulk area the etch pattern has to increase by adding an outer rim of  $198\text{ }\mu\text{m}$ .

The KOH mask is also used for defining breaking V-grooves with a width of  $260\text{ }\mu\text{m}$ . These V-grooves will be  $183.6\text{ }\mu\text{m}$  deep, this leaves still  $200\text{ }\mu\text{m}$  of silicon on a  $385\text{ }\mu\text{m}$  thick wafer which ensures the structural stiffness needed for further processing. The ends of the V-groove patterns may not contact each other and have a spacing of  $750\text{ }\mu\text{m}$  and are marked in figure 4.29. When the grooves touch each other we get a cross, that cross will become a square as the internal corners of the cross will etch diagonally along the exposed  $\langle 110 \rangle$  plane.

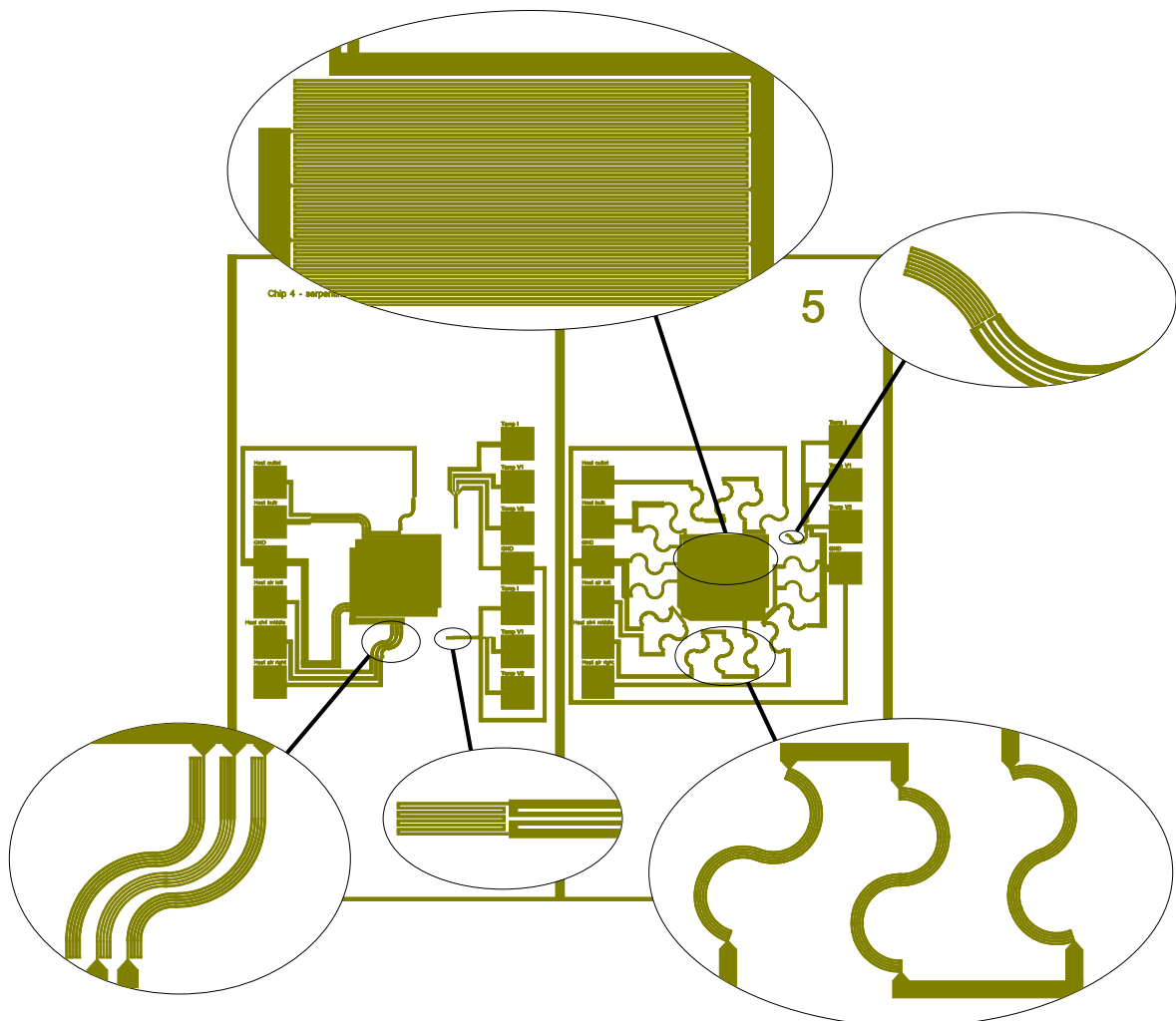
The crystal orientation of the  $\langle 100 \rangle$  plane may differ a few degrees per wafer from the wafer flats which results in rotation of the etched KOH pit. The orientation of the  $\langle 100 \rangle$  plane can be found by using the Vangbo alignment technique [58]. For our design the patterned area can also be increased with an outer rim of  $500\text{ }\mu\text{m}$  which results in a pit with a large thinned area. By using a large area the angle of the pit does not influence the placement of the trenches in the frontside of the wafer. This increased rim also keeps the mask compatible for the use with  $525\text{ }\mu\text{m}$  thick wafers, which require a rim of  $300\text{ }\mu\text{m}$  for reaching an etching depth of  $425\text{ }\mu\text{m}$ . The resulting patterns are shown in figure 4.29.

The metal is put at almost the end of the processing to prevent contamination of the cleanroom ovens and etchers. The patterned platinum can be removed by etchant or by lift-off of the layer, the section about the fabrication will give more insight in which method is the best to use. A minimum feature size of  $4\text{ }\mu\text{m}$  is used to prevent interruptions in the platinum surface caused by defects in the pattern transfer and etching/lift-off. The width of the temperature sensing tracks are  $4\text{ }\mu\text{m}$  and the heaters are  $8\text{ }\mu\text{m}$  wide. The rest of the tracks are larger than  $100\text{ }\mu\text{m}$  and lead to the bondpads which are  $1\text{mm}^2$ . The metal mask for both designs can be seen in figure 4.30.

The front-release mask is used for creating an  $1\text{ mm}$  wide trench to release the core from the wafer. The SiRN is patterned and is used as etch mask for the underlying silicon. The silicon is etched with a semi-isotropical etch because using an isotropical etching would create a shaded area beneath the channel tubes which result in unetched silicon beneath the channels. The shaded area would give an increase in thermal losses which is an unwanted product. The release mask for both designs can be seen in figure 4.31.

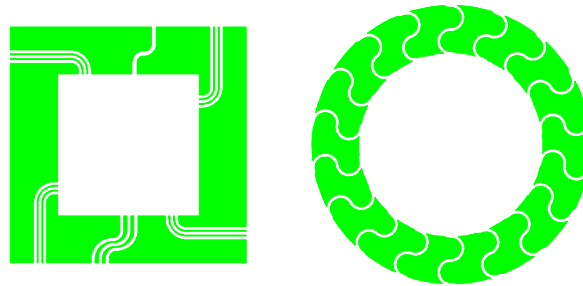


**Figure 4.29:** The KOH patterns in blue with the front-release mask in green. The area of the bottom of the KOH pit is larger than the area of the front-release mask which makes it possible to ignore the  $\langle 100 \rangle$  crystal offset. The area marked with the red circle are the V-grooves which have a spacing of  $750 \mu\text{m}$  between them.



**Figure 4.30:** The metal pattern with some magnifications of the heaters and sensing elements.

For each mask an alignment marker is needed to align the masks in reference to each other. The



**Figure 4.31:** The release mask which creates the trench in the silicon. The highlighted area are the spaced V-grooves.

alignment marks are specifically designed for the processing that is done with the mask. The first mask, access-holes, goes on the blank wafer, the size of alignment marks have to be kept below the  $50\text{ }\mu\text{m}$  to prevent a wafer through etch.

The second mask, channel, is aligned with a front to back alignment in the mask aligner to the access-holes mask and the virtual cross-hair has to be align with the access-hole markers. Front to back alignment uses a virtual cross-hair which is first aligned with the mask and after inserting the wafer the cross-hair is projected on the image of the wafer alignment marks. The markers on the channel mask have to be build of the slits that are used for the channels as larger feature size will result in open channels or even gaps which will fill with fluid during the processing.

The third mask, KOH, is aligned with the access-holes mask and the aligner features have to be square as they are etched in the KOH.

The fourth mask, metal, is aligned with the channel mask and as the metal mask is a positive mask we can see through the drawn area's. The open area's have to be big enough for the orientation on the underlying wafer and the smaller feature sizes are used for the alignment.

The fifth mask, release, is aligned with the metal mask. This is also a positive mask which requires open area's to see the underlying structure and small features for the alignment. As there is a possibility that the processing of metal layer will give smaller features due to the etching we anticipate this by creating mask features that 'stick-out' and will align in that case.

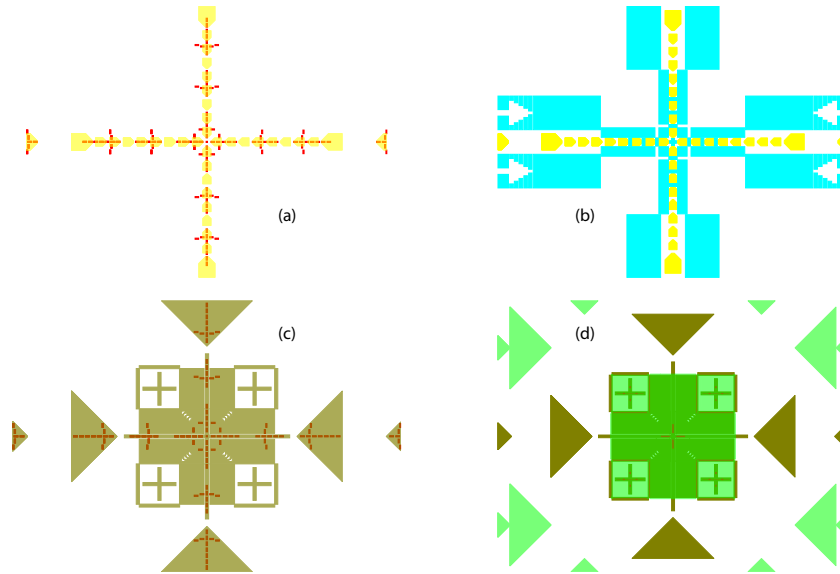
The steps mentioned here above are all shown in figure 4.32. All mask design have a name in the right corner, the backside masks have their name reversed and at the left side as they will be mirrored during production. When all these masks are combined in one view we obtain figure 4.33.

## 4.7 Conclusion

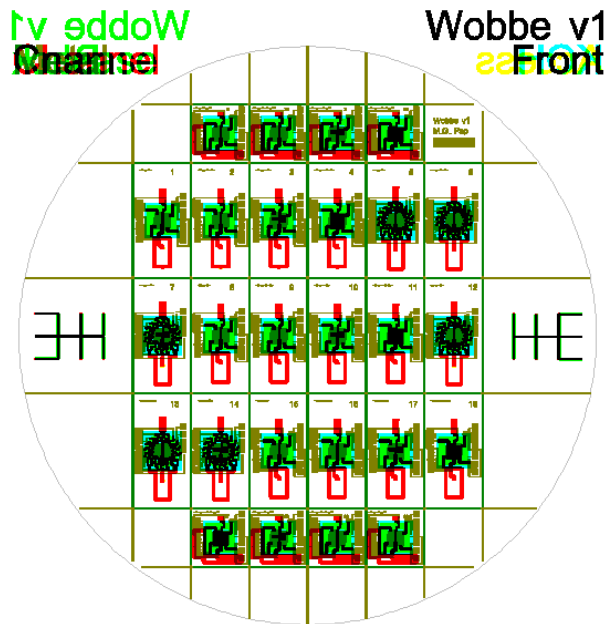
The fuel and oxidizer gasses are introduced to each other with a sheet mixer to optimize the diffusion of the fuel into the oxidizer. Research into a way for increasing the reaction area of combustion gasses delivered a new approach for creation of buried channels micro-mixers, which can be interesting for the research field of mixing liquids.

The combustion will increase the pressure-drop over the channels of the chip due to the thermal expansion and the temperature dependent viscosity. The pressure-drop will influence the flow delivered by the mass flow controllers in the case that the pressure-drop exceeds the specifications. Cooling of the combustion gasses and non-uniform temperatures will reduce the estimated pressure-drops and measurements have to show the real values.

The design phase of the chip started with the idea of a beam suspended core with an  $1\text{ J/s}$  dissipation however the designing of the chip should have been started with the high temperature micro-heaters. The design of the micro-heaters gets complicated due to the maximum current density. Most of the high-temperature heaters in other studies have a width of  $100\text{ }\mu\text{m}$  and have the length of a few centimetre in that case the current density is not a big issue. The amount of power that is needed for the heat flux into the gasses should be used as starting point which requires a description of the transfer of the heat in



**Figure 4.32:** The aligners of the processing steps overlaying each other, in (a) the channel mask is aligner with the access-holes mask, in (b) the KOH mask is aligned with the access-holes mask, in (c) the metal mask is aligned with the channel mask and in (d) the release mask is aligned with the metal mask.



**Figure 4.33:** The wafer with all the masking layers on top of each other. In total here are 26 chips with 2 designs with 4 variations for the square core and 3 variations for the circular core.

the gasses for a single buried channel. From there on the minimum track cross-sectional area should be calculate with the current to stay below the maximum electro-migration current density. With the found current we calculate the needed length of the heater track to achieve the needed amount of dissipated power. This track has to fit on top of the slab on buried channel, if this is not possible the dimensions of the surface have to be scaled to support the heater track. This can be done by increasing the length, by placing channels in parallel or by increasing the width of the slab of SiRN on top of the channel. For example by using a heater track with a width of  $80\text{ }\mu\text{m}$  which is the width of the design buried channel and a height of  $500\text{ nm}$  the current density can be reduced to  $21,250\text{ A/cm}^2$  which is below the limit of  $10^5\text{ A/cm}^2$ . This requires that all other connecting tracks need to much wider to avoid heating. By

placing multiple channel parallel for a single flow with the heaters in parallel the power is divided over the heaters which reduces the current through a single heater and the resulting current density.

Another way to reduce the amount of power in a heater is to increase the length of the gas inlet tubes. The increase in area of the channel walls requires a smaller heat flux for heating of the gas as the time to absorb the heat from the walls increases.

The unknown behaviour of combustion in the buried channels gives design difficulties as the heat flux transfer from the gas to the core is dependent on the temperature of the core, the mass-fraction of fuel and oxidizer and in the position over the length of the channel. We approached the combustion energy as a steady heat flux which is uniform released in the core but further research is needed to obtain a more complete model with focus on the combustion location inside the channel and the thermal losses through the exhaust.

With the developed process-flow and the designed masks the production can be done inside the clean-room which will be discussed in the coming chapter.



# Chapter 5

## Fabrication

In this chapter we describe the production of the chip inside the Mesa+ Nanolab. A summary of the step by step processing that is needed for creating the design was described in the previous section but it is a guideline for fabrication. The actual experience of the processing with the process-flow in the cleanroom is described in this section. The processing was started with 6 dummy and 6 production wafers. As dummy wafers were used 525  $\mu\text{m}$  <100> wafers, these dummies are used for verifying processing steps and to create cross-sections of the wafer. The wafer allocation is given in appendix C.2.

### 5.1 Masks

The structures on the wafers are defined with lithography which requires mask plates created from the mask designs which were shown in the previous section. It is critical for the production of the chip that the channel mask is conform the design specifications. Inspection of all the masks plates revealed that the channel mask was not within design specifications.

To ensure that the mask was within the critical limits we produced three mask plates with different exposure times and a fourth with a different feature size. These plates were inspected with an optical microscope and the slits were measured. The mask plates are covered with a positive photoresist which is exposed with a mask writer which uses lasers for the exposure. Decreasing the exposure results in a decrease slit size as less photoresist is exposed. The results can be seen in figure 5.1. The first run with an exposure of 20  $\text{mJ}/\text{cm}^2$  has a horizontal slit width of  $1.6 \mu\text{m} \pm 0.21 \mu\text{m}$  and a vertical slit width of  $2.2 \mu\text{m} \pm 0.07 \mu\text{m}$ . The second run with an exposure of 18  $\text{mJ}/\text{cm}^2$  has a horizontal slit width of  $2.04 \mu\text{m} \pm 0.09 \mu\text{m}$  and a vertical slit width of  $2.27 \mu\text{m} \pm 0.07 \mu\text{m}$ . The third run with an exposure of 16  $\text{mJ}/\text{cm}^2$  has a horizontal slit width of unmeasurable as the majority were not exposed enough and the vertical slits have a width of  $2.0 \mu\text{m}$ . The slits measurements were done with epi (top) and dia (back) light and with measurements on multiple places of the wafer. The second mask shows results against our expectation as the slits are wider than those with a higher exposure but the uniformity of these slits is better.

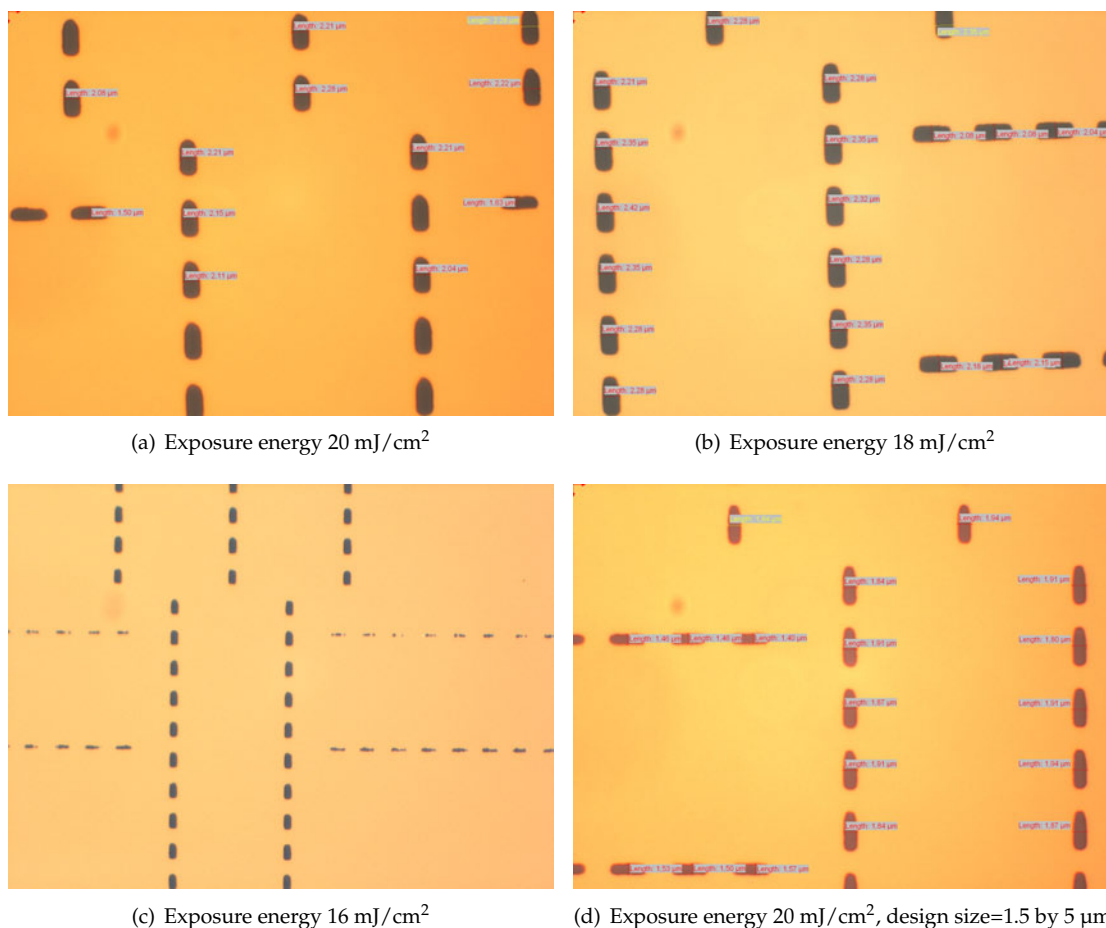
As the mask were still not within the specifications we produced a fourth mask with designed slits of 1.5 by 5  $\mu\text{m}$ . This feature size is the theoretical limit of the mask writer. This mask had an exposure of 20  $\text{mJ}/\text{cm}^2$  and has a horizontal slit width of  $1.49 \mu\text{m} \pm 0.1 \mu\text{m}$  and a vertical slit width of  $1.83 \mu\text{m} \pm 0.06 \mu\text{m}$  which is within specifications. An overview of the values is given in table 5.1

### 5.2 SiRN deposition

The first SiRN deposition run on the bare wafers introduced non-reacted silane particles on some of the wafers. The particles can only be seen by using floodlight under at angle to the surface. With the floodlight these particles appear as spots on the surface. The silane particles are a side-effect of the SiRN deposition method as with every run the tube is polluted with these particles. At the moment there is

	Horizontal slits		Vertical slits	
Mask	size [μm]	st.dev. [μm]	size [μm]	st.dev. [μm]
1: 2.0 μm 20 mJ/cm <sup>2</sup>	1.6	±0.21	2.2	±0.07
2: 2.0 μm 18 mJ/cm <sup>2</sup>	2.04	±0.09	2.27	±0.07
3: 2.0 μm 16 mJ/cm <sup>2</sup>	-	-	2.0	-
4: 1.5 μm 20 mJ/cm <sup>2</sup>	1.49	±0.1	1.83	±0.06

**Table 5.1:** The size and standard deviation of the slits of the different mask plates.

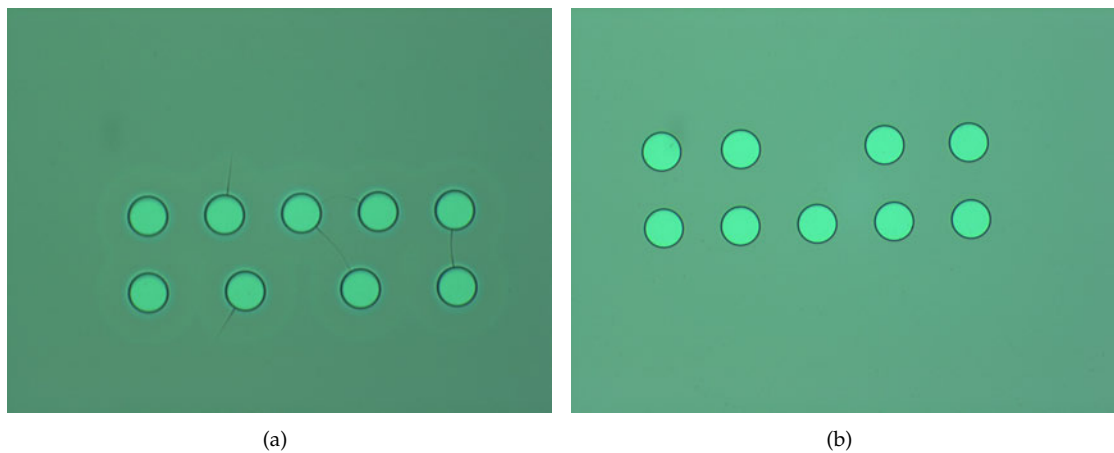


**Figure 5.1:** The Chromium mask plates exposed with (a) 20 mJ/cm<sup>2</sup>, (b) 18 mJ/cm<sup>2</sup> and (c) 16 mJ/cm<sup>2</sup>. It can be concluded from the figures that the mask writer is not symmetrical in the horizontal and vertical direction but an optimum in symmetry can be found at an exposure energy of 18 mJ/cm<sup>2</sup>. The mask of run 4 (a) is within the specifications but still has an asymmetry in the horizontal and vertical slits.

no time efficient method to clean the tube after every run. Fortunately others runs did not suffer from this problem. The sides of the wafer with the least particles were selected as the front side of the wafer as this side has the most critical structures on it: the channel-slits.

### 5.3 Access-holes

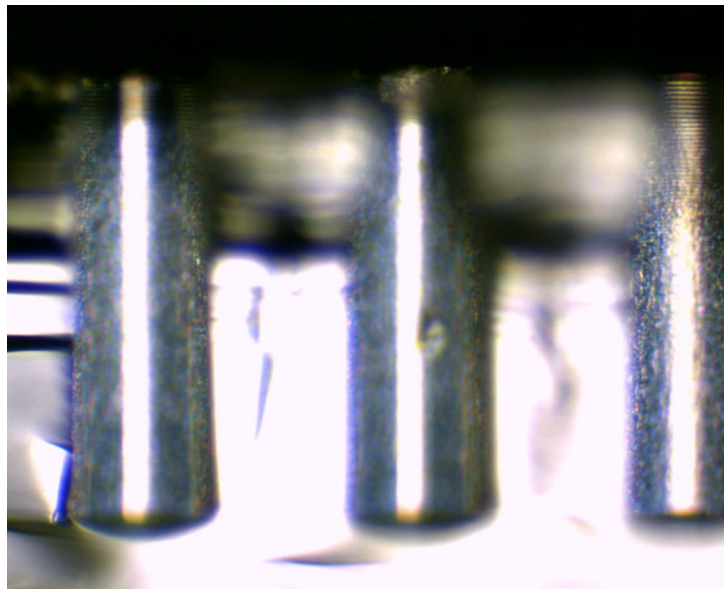
After applying the pattern in the SU-8 2005 a hard bake is needed to re-flow the cracks that appear after the post-exposure bake. The result of a hard bake can be seen in figure 5.2 where the holes have an average size of 49  $\mu\text{m}$ .



**Figure 5.2:** The hole pattern a post bake is given in (a) where the holes have cracks. By applying a post bake these cracks are gone as can be seen in (b).

The patterned layer of SiRN was opened with the process "Beuken met Robert" which took 130 seconds. Production wafer P2 had a hole in the resist which was closed with a piece of Kapton tape.

The access-holes were etched with the recipe "Pulsed CHF<sub>3</sub>-Goan". Dummies D1-D3 were sacrificed for tuning of the etch time and recipe. It took 34 minutes of etch time to reach the SiRN layer on the frontside of the wafer which gives an etch rate of 11.3  $\mu\text{m}/\text{min}$ . The hole size under the SiRN was verified with an optical microscope, the holes could be distinguished as purple spots on a light green surface. As the etching reaches the SiRN a notching effect occurs by reflection via the SiRN of the incoming ions to the silicon. The purple spots had an average size of 75  $\mu\text{m}$  and a solar ray pattern at the outer rim causes by this notching. The entrance holes at the backside of the wafer have an average size of 54  $\mu\text{m}$ . A cross-section of wafer D3 with three access-holes can be seen in figure 5.3.



**Figure 5.3:** Three test access-holes created by DRIE Bosch etching.

After the DRIE etching the SU-8 was stripped in Piranha and the wafers were put in a dry oxidation furnace for the removal of the fluorocarbon residue. Unloading of the wafer boat cracked production wafer P4 at the corner which was damaged earlier in the processing. The rest of the dry oxidized fluorocarbon was removed with HF 1%.

The holes were coated with an 1050 nm layer of TEOS in a 112 minutes run where the wafers were spaced 3 slots apart from each other.

## 5.4 Channels

The definition of the channel slits was tested on 4 extra chromium coated test wafers. The chromium mask on top of the SiRN layer acts as a high-definition slit window and was patterned with 1.7  $\mu\text{m}$  907-17 photoresist. Post-bake of the resist increased the width of the slits to 2.4  $\mu\text{m}$  and shapes them oval, therefore a post bake of the resist was left out of the lithography step. During the photoresist processing step wafers P3 and D6 were destroyed by misfortune. The chromium layer was etched for 40 seconds to open the slits.

The SiRN layer was etched in 130 seconds at  $-40^\circ$  by the process "Beuken with Robert" and an inspection after "Beuken with Robert" revealed that the slits still had the same size. The removal of the SiRN was followed by the semi-isotropic channel etch. The channel etch took 30 minutes at  $20^\circ$  which resulted in a channel cross-section for a double channel with a width of 68  $\mu\text{m}$  and a height of 32  $\mu\text{m}$  obtain by breaking D5 and is shown in figure 5.4. Only a thin layer of photoresist remained after the etching of the channels.

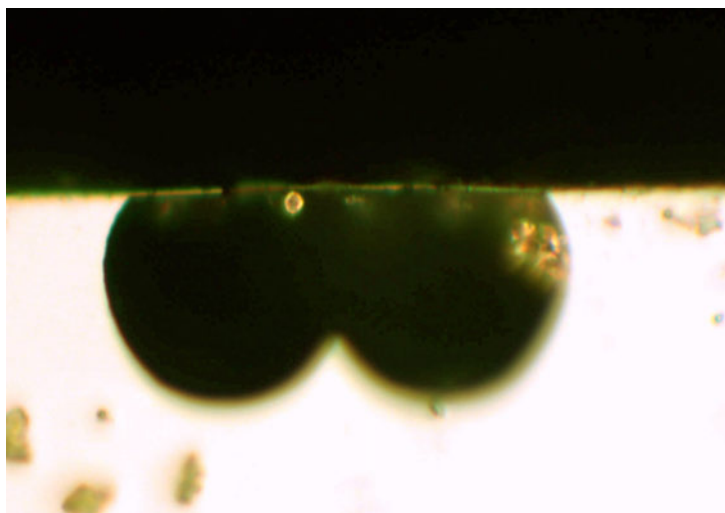
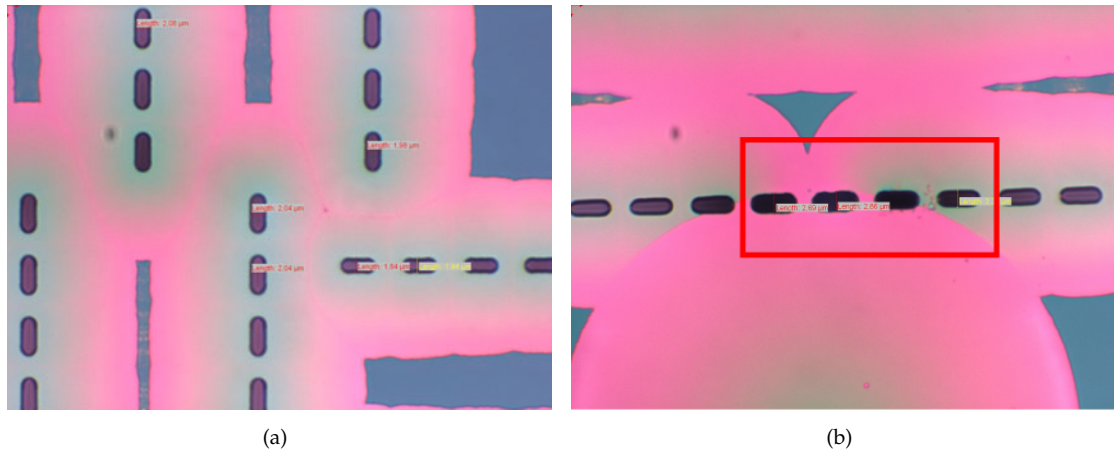


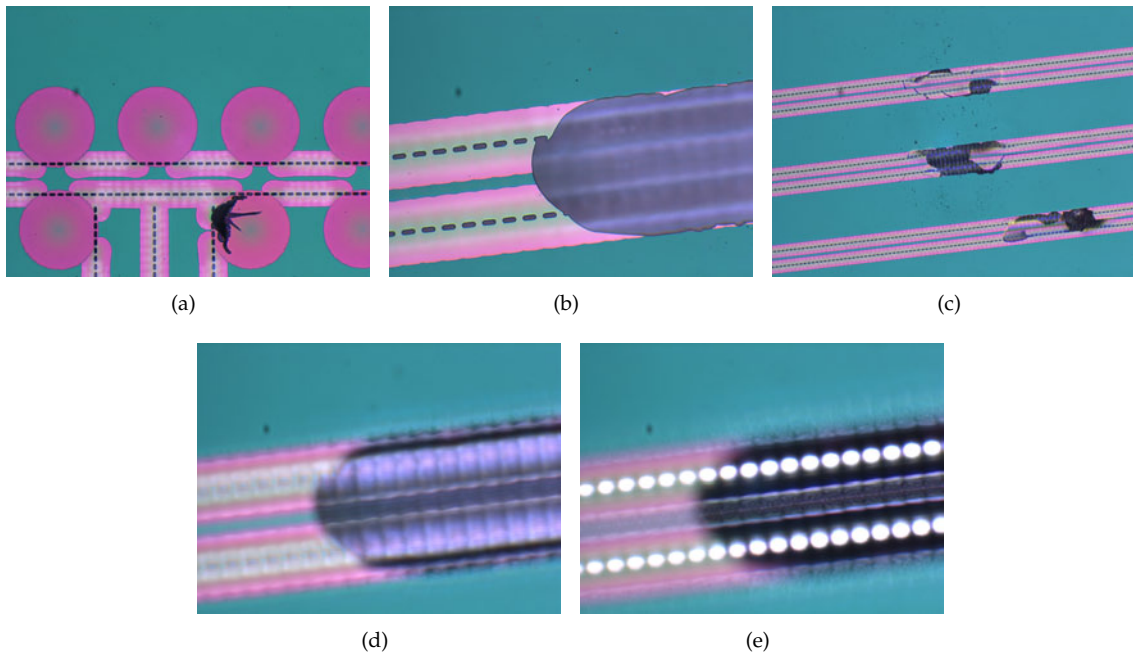
Figure 5.4: A cross-section of D5 which shows a double buried channel.

The removal of the photoresist was done in 20 minutes with the Tepla barrel etcher in an oxygen plasma. The oxygen plasma also removed a part of the chromium from the wafers and not only the photoresist. The amount of chromium etched was wafer position dependent. As the chromium had to be removed in chromium etchant the plasma stripping of the chromium would result in a reduced etch time, but the opposite was true. The oxygen plasma had created a chromiumoxide which had a very low etch rate in the chromium etchant. After 24 hours soaking in the etchant a thin layer of chromium was still left. Aqua regia was used for opening up the layer structure but after a hour the etch rate dropped to zero. Another soak in the chromium etch for an 8 hours was needed to completely remove the chromiumoxide.

Inspection after the cleaning shows that the access-hole are etched under an angle which is placed dependent. This can clearly be seen as the channel slits have an overlap with some of the access-holes which differs per chip. The semi-isotropic etching also increased the final size of the slits. The TEOS layer beneath the slits increased the slit diameter in the worst case with a factor of 1.5 during the etching to a size of 2.83  $\mu\text{m}$  which can be seen in figure 5.5. The TEOS layer acted as a reflector which scattered the incoming ions towards the side walls during the etching. Unfortunately the whole process was not defect free as some channel roofs were collapsed as can be seen in figure 5.6.



**Figure 5.5:** Normal etch channels slits look like (a) and the worst example of slits that can be found look like the marked section in (b).



**Figure 5.6:** In (a) a broken lid over an access-hole is shown. The complete cap is removed in (b) where can be seen that the channels are internally connected to each other. Not only do the broken caps fall from the wafer but also in the channels as shown in (c). In (d) is shown that the channels are build out of sections (grey) of 10 µm long which creates a ripple in the channel. In (e) can be seen that etching creates a focal spot (white spot) at the bottom of the channel which even can be seen through the top of the cap.

The structure of the channels reveal also another problem: the capillary action of the channels will keep the fluid trapped until the wafer is spun in a spin-dryer. This creates the problem that after the spinning the wafer has dirty spots. A solution for this problem is using the semitool batch dryer after cleaning in the quickdump rinser. The semitool batch dryer rinses the wafers with demi-water while they are spinning, in this way everything that comes out of the channels is rinsed away and by using this method twice the best result is obtained. After this cleaning step the wafers go overnight for 16 hours into a drying oven at 85°C to evaporate the fluid that was still left in the channels. Unfortunately after drying there are still drying spots of the residue at the channel openings and defects.

The channels were closed by growing 1696 µm of SiRN in a 6 hour and 17 minutes run which gives

a channel wall thickness of 1.4  $\mu\text{m}$ .

## 5.5 Core by KOH etching

KOH etching is used for thinning out the bulk of the core and definition of the breaking grooves. The KOH will etch under an angle of  $54.7^\circ$  along the silicon crystal structure and is stopped at a depth of 280  $\mu\text{m}$  which leaves a bulk of 100  $\mu\text{m}$  thick. KOH etches silicon with 1  $\mu\text{m}/\text{min}$  but also  $\text{SiO}_2$  with 180nm/min and SiRN with  $<0.6\text{nm}/\text{hour}$ . The SiRN will be used as masking layer for the KOH etch due to its slow etch rate. Before that can happen the SiRN on the backside of the wafer has to be patterned with a photoresist and then removed with the DRIE-etching process "Beuken with Robert". The photoresist has also to seal the access-holes that are located on the back side of the wafer to protect the SiRN that is coating the sidewalls and bottoms of these holes.

### 5.5.1 MX5020 Lithography

A normal resist could be used which is applied with spincoating on the wafer however the backside has holes with a width of 50  $\mu\text{m}$  which will fill with the liquid resist. Once in the access-holes the resist would flow into the channels which would result with a positive resist in a solid substance that fills all internal channels of the wafer after the pre-exposure bake. A negative resist would stay liquid inside the channels but this would also require extensive rinsing in demi water. There is also a risk that at the edge of holes the resist will be thinner than at the flat surface as it keeps flowing into the channels until it is baked on a hotplate. In the case that the edge is significant thinner, the underlying SiRN can be exposed during the etching as the etchant also etches the photoresist at a low rate.

An alternative for liquid photoresist would be using a polymer based resist film like the Dupont MX5020 which is in storage but there are also others on the market. The polymer is applied by means of a transfer foil on to the wafer where it will adhere to the surface. The film will span the gaps of the access-holes and with this method no resist will come into the channels. This polymer is resistant against dry and wet etching which makes it suitable as process step for the chip. A new process flow has to be developed as the process is new to the process database of the Mesa<sup>+</sup> Nanolab.

The MX5020 is a negative 20  $\mu\text{m}$  thick photoresist which at exposure of UV-light hardens to a dark-blue coating. Non-exposed areas can be removed by a developer that is based on  $\text{KCO}_3$  or  $\text{NaCO}_3$  in which the carbonate is the working component. After development it can be used as protective film for dry and wet etching.

Applying of the foil to the wafer is the most difficult part as air-pockets can be easily trapped below the foil. As result of these air-bubbles the polymer does not adhere to the surface and is removed during the development of the film. This happens even with micro-bubbles which have a diameter smaller than 50  $\mu\text{m}$ , initially these bubbles cannot be seen with the transfer foil on top of it. The air in these micro-bubbles will expand during the bake sessions which will stretch the polymer film. The results of large air-pockets can be seen in figure 5.7.

A manner to reduce the large bubbles to only micro-bubbles is by cleaning the roller with a tissue with iso-propanol to remove any large particles that could leave an impression in the polymer during the rolling. The foil has to lay flat on the wafer and the rolling is started on the foil next to the wafer, this requires that the sheet of foil is bigger than the wafer it self. While applying force on the roller, the foil has to be pulled back along the surface of the roller but to much tension will cause ripples in the foil during the rolling. By slowly rolling the foil onto the wafer the foil can be applied with very few visible air pockets another session with the roller can further improve adherence to the wafer. In the case of wrinkles in the foil it is better to completely remove the foil and to use a new piece, otherwise the wrinkles will stay in the polymer layer by reapplying the foil. The process of applying the foil was also tried in a laminar flow bench with the wafer on a  $90^\circ\text{C}$  hotplate. The airflow in the bench hinders a wrinkle free applying of the film and when the polymer touches the heated wafer is instantly sticks to the surface which makes it impossible to roll out any air bubbles.



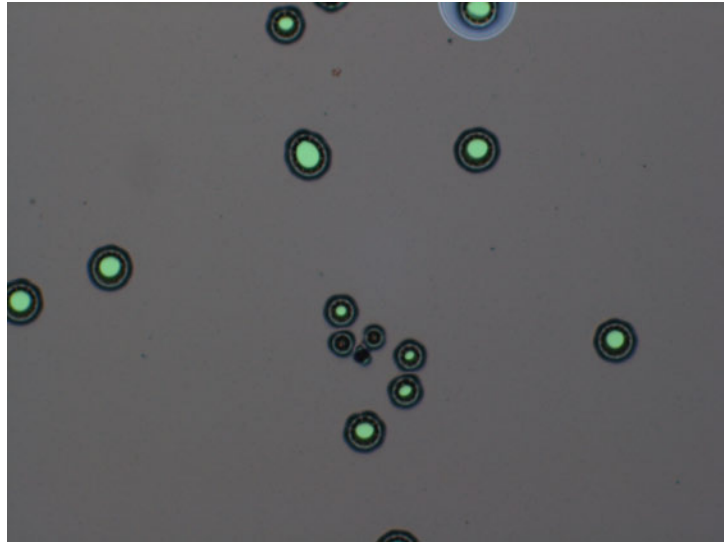


Figure 5.7: Holes in the polymer film caused by trapped air pockets.

After the film is applied, the wafer is folded inside a sheet of cleanroom paper and the package of paper and wafer is guided in the laminator that is set on 90°C at speed 2. The easiest is to start with the wafer on the paper before applying the transfer foil. The increased temperature of the laminator adheres the polymer to the wafer and paper, which requires cutting the wafer from the paper with a scalpel for further processing. An important sidenote is that the foil has to be cut close to the edge as the surplus of polymer will harden at the UV-exposure and will produce slivers. These will release inside the waferbox and during transport from the load-lock to the processing chamber in the case of dry-etching.

An extra pre-bake of 45 seconds on a hotplate at 95°C is required for better adhesion of the polymer. After the bake the lithography can be done on the EV620. This machine has an UV-lamp with an intensity of 12 mJ/cm<sup>2</sup>, the manufacturer of the polymer film advises an exposure dose of 35-105 mW for a proper polymer linkage, which gives an exposure time of 3-8 seconds. Tests show that an exposure time of 5-8 seconds will resist 1 minute of development time, a lower exposure time will result in underetching at the boundaries of the exposed polymer. Each 30 seconds of extra development time will require an extra second exposure time, an 8 second exposure polymer is hard to remove with the developer but eventually lift-off will occur. The protective transfer foil has stay on the polymer otherwise the wafer will stick to the mask at even soft-contact mode. The best results are obtain with an exposure of 8 seconds and therefore the further flow will specified for this exposure time. During exposure and baking the film turns blue which makes it difficult to distinguish the features of the cross-hair aligners that were already patterned in the underlying layer of SiRN. This forced the use of front to back alignment.

The next step after the lithography is the post-exposure bake which is divided into two baking step. The best results are achieved when the wafer first goes for 45 seconds on the 95°C hotplate. After this bake the protective transfer foil that is still on the wafer is removed and the wafer goes for 45 seconds on the 120°C hotplate. This baking step ensures an even better adhesion of the polymer on the wafer, without this step there is clear underetching at the boundaries of the polymer area's which can be seen in figure 5.8. A bake time of 90 seconds on only the 95°C hotplate gives also an underetch. Increasing of the bake time at 120°C results in a few µm of polymer reflow which is shown as a slope at the boundaries.

The developer is composed of 15 g NaCO<sub>3</sub> solved in 1.5 (10g/L) litre of demi-water. This is kept at 32°C with a stirrer at the bottom with a speed of 24%. The development time is concentration dependent but it takes between the 70-80 seconds to solve large area's, this change is also visible to the eye. Feature sizes in the pattern of the film with difference of a factor of 1000 (5mm - 5µm) introduce further difficulties in the process of development. The development time mentioned here above is valid for a feature size with a factor of 100 (5mm - 50µm). Smaller feature sizes which were located in the cross-hair aligners of the mask showed deformation and underetching. As this mask was the last on the back side of the

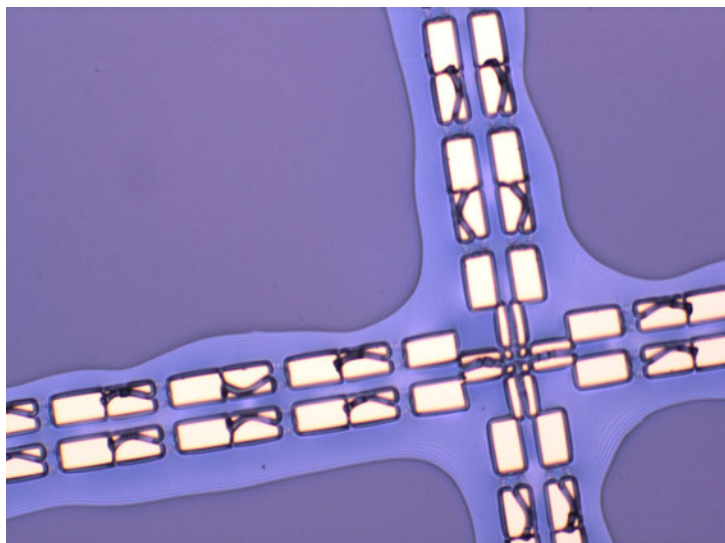


Figure 5.8: Underetching of the polymer due to not proper adhesion without extra post-bake step.

wafer there were no consequences for future alignments and was seen as an acceptable loss.

After the development and rinsing/drying there is a possibility to do an extra hard-bake of 45 seconds at  $120^\circ$ . The extra hard-bake creates no visible difference in the reflow of the patterns or the micro-bubbles and further tests have to turn out if this bake promotes further polymer linkage. The final polymer layer of the photoresist has a height of an  $18.8\text{ }\mu\text{m}$ .

Inspection with an optical microscope revealed that 50% of the access-holes were open after the processing which indicates that the polymer is less suitable for spanning the airpockets created by the access-holes. Everything indicates that the air inside the channels of the chip expands during the baking of the polymer, as was the case with the micro-bubbles, which causes the destruction of the polymer cap over the gaps. The places where the polymer stayed intact could indicate a leakage in the connected channel. The coverage of the access-holes could only be tested with the production wafers so we continued with the polymer as masking layer for the SiRN etch and the open access-holes were covered with pieces of Kapton tape. The complete process flow is given in table 5.2.

### 5.5.2 SiRN etching

The process for etching a  $2.2\text{ }\mu\text{m}$  thick layer of SiRN is normally done on the Adixen 100SE with the process "Beuken with Robert" but at the required moment the Adixen was offline. As alternative to the Adixen the Oxford Plasmalab 100 "cathy" was used. The difference between the process "Beuken with Robert" and the Oxford is that "Beuken with Robert" etches only the SiRN and the Oxford will etch the SiRN and the underlying silicon.

With the Dupont MX5020 polymer as etching mask the SiRN was etched. The etching was done at a temperature of  $20^\circ\text{C}$  with gasflow of 25 sccm  $\text{SF}_6$  at an ICP of 600W, CCP of 150 Watt full-scale, a pressure of 10 mTorr and a helium pressure of 10 mBar. After 11 minutes the centre of the wafer was stripped of nitride but the rest of the wafer had still a parabolic distributed layer of SiRN with at the rim still 150 nm left. The removal of this thin film was done with the RIE etcher Tetske with a recipe that had a high selectivity between SiRN and Si. The etching was done at a temperature of  $20^\circ\text{C}$  with a gasflow of 25 sccm  $\text{CHF}_3$  and 5 sccm  $\text{O}_2$  at a power of 60 Watt, a pressure of 10 mTorr and a bias of 489 VDC. The etching of the SiRN took 7-8 minutes. Inspection with an optical microscope revealed that the polymer which covert the gaps was still intact which can be seen in figure 5.9.

The processing in Tetske revealed also another phenomenon: redeposition of the etched polymer onto the bare silicon surface which can be seen in figure 5.10.

The removal of the polymer was done in Piranha ( $\text{H}_2\text{SO}_4\text{:H}_2\text{O}_2$  3:1) but the Kapton which was not removed stayed on the wafer as the silicon adhesive and plastic tape which are used for the Kapton are



Dupont MX5020 process flow	
Step	Description
1	Place wafer on a sheet of cleanroom paper. Clean the roller with a tissue with IPA.
2	Cut the foil to 1.5 times the size of the wafer. Put a piece of tape at both sides of a corner of the foil and pull with the tape the protective foil of one side of the polymer. Dust of the wafer and foil with the N <sub>2</sub> gun.
3	Lay the foil over the wafer and place the roller at the base of the foil that is on the paper. While applying a downwards pressure pull back the foil along surface of the roller and slowly roll the foil on the wafer. In the case of wrinkles remove the foil and use a new piece.
4	Set the laminator at 90°C and speed 2. Fold the paper over the wafer and guide the package through the laminator. Cut the wafer from the paper with a scalpel as close as possible to the rim.
5	Pre-exposure bake 45 seconds on the 95°C hotplate.
6	Alignment and exposure for 8 seconds on the EV620.
7	Post-exposure bake 45 seconds on the 95°C hotplate. Remove the protective foil. Post-exposure bake 45 seconds on the 120°C hotplate.
8	Develop in NaCO <sub>3</sub> or KCO <sub>3</sub> (10 g/l) for 70-80 seconds. Quick dump rinse and spin drying.
9	Optional hard bake 45 seconds on the 120°C hotplate.
10	Removal of the polymer can be done with Piranha

Table 5.2: The process-flow for the MX5020 foil.

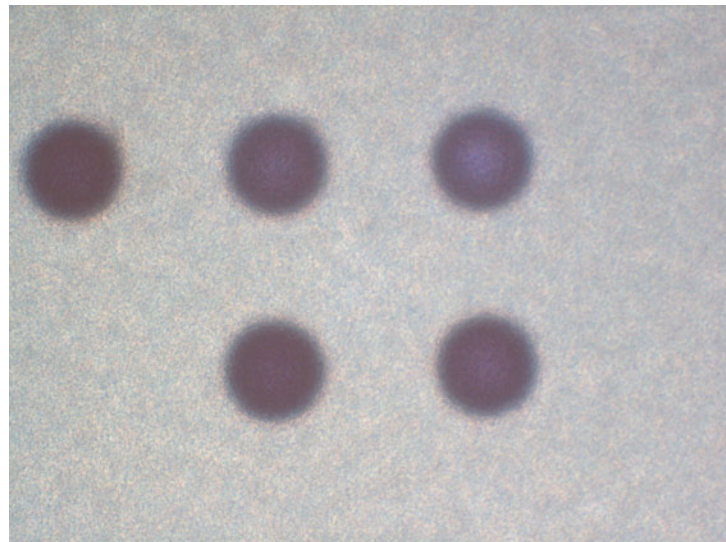


Figure 5.9: Polymer over the gaps after etching with Cathy and Tetske

poorly solvable in Piranha. The silicon adhesive could only be released from the wafer by scratching the top plastic layer of the wafer with a wafer-tweezer, cleaning with acetone and a cleanroom tissue removed the silicon adhesive. It was a mistake to not remove the Kapton tape mechanical before the cleaning with Piranha.

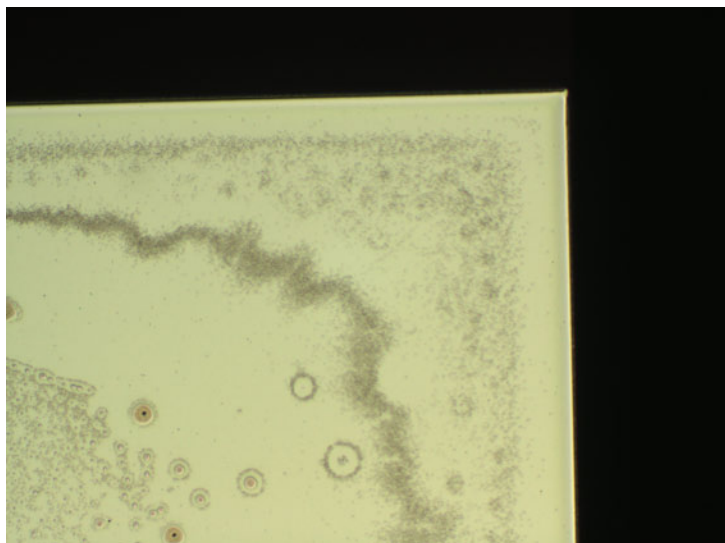


Figure 5.10: Redeposition of the polymer onto the bare silicon after etching in Tetske.

### 5.5.3 KOH pit

The KOH etch started with a hydrofluoric (HF) acid 1% etch to remove the native oxide on the wafer. The KOH etchant etched the silicon to a depth of  $280.32\ \mu\text{m}$ . After RCA-cleaning the wafer had to dry in the oven overnight before the deposition of TEOS in the KOH pit. A layer of  $1100\ \text{nm}$  TEOS was grown on the wafer and was stripped from the frontside of the wafer by a buffered hydrofluoric (BHF) acid. With the naked eye dark spots could be distinguished on the surface. Inspection with an optical microscope revealed that at the defects in the channel roofs the TEOS layer was harder to remove which is shown in figure 5.11, removal of these spots required some extra BHF etch time. We assume that the spots are residual fluids which came out of the channels during the run in the TEOS oven.

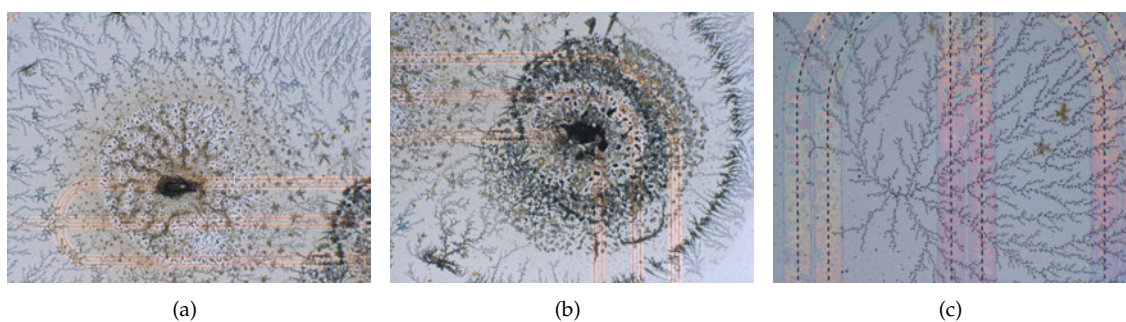


Figure 5.11: Spots near the defects after the TEOS etching in BHF are shown in (a), (b) and (c).

An inspection of all the chips on the wafers after the TEOS strip gave the yield that is shown in table 5.3. From the 104 chips on the 4 production-wafers only 11 are without defects, 25 are deemed repairable by closing of parallel channels with epoxy glue and 68 are defect. The middle horizontal rows on the wafers have the most defect-free chips. There was an increase in the amount of defects at the inspection after the polymer process with KOH etching than before the process and we suspect that the force of the roller is responsible for the extra defects.

	19   1R,3B	20   4B	21   4B	22   1R,3B	
1   2R,2B	2   1G,1R,2B	3   2R,2B	4   1R,3B	5   1G,3B	6   2R,2B
7   1G,1R,2B	8   1G,2R,1B	9   1G,3B	10   1G,1R,2B	11   1G,1R,2B	12   2R,2B
13   2R,2B	14   2R,2B	15   4R	16   1G,3B	17   1G,3B	18   1G,3B
	27   1G,3B	28   4B	29   4B	30   4B	

Table 5.3: Yield of 4 production wafers. Coding: Chip number | amount G=Good, R=Repairable, B=Bad |

## 5.6 Platinum on SiRN

The process for adhering platinum without an adhesion layer on SiRN was only done in the old clean-room and never repeated in the Mesa+ Nanolab. Therefore a new process has to be developed which has as base the processing done in the past by Tiggelaar [54, 55, 56]. The tests with the process of Tiggelaar are described as first and thereafter we will describe the new process.

The SiRN was roughened to promote the adhesion of the platinum to the SiRN. This was done in Tetske with a gasflow of 30 sccm  $\text{SF}_6$  and 5 sccm  $\text{O}_2$  at a pressure of 7 mTorr with a power of 40W for a time of 30 seconds. On the rough surface a layer of 150 nm platinum was sputtered with Sputterke, this was done with an 148 sccm argon flow at a pressure of  $6.6 \cdot 10^{-3}$  mBar with a power of 200 watt. The platinum layer was spin-coated with a layer of HMDS primer and an  $1.7 \mu\text{m}$  layer of OiR 907-17 photoresist. The photoresist was exposed in the mask aligner with the metal mask and developed. The platinum that was exposed was oxidized in Tetske with a gasflow of 20 sccm  $\text{O}_2$  at 10mTorr with a power of 32 Watt (VDC 400V) for a time of 60 seconds. This oxidation created a patterned layer of platinumdioxide ( $\text{PtO}_2$ ) and by removal of the photoresist with  $\text{HNO}_3$  the pure platinum was revealed. The  $\text{PtO}_2$  covered a 10-20 nm layer on top of 130 nm platinum and protects the underlying platinum against the etchant. The platinum was etch in aqua regia ( $\text{H}_2\text{O}:\text{HCl}:\text{HNO}_3$ , 8:7:1) for 4.5 minutes at  $80^\circ\text{C}$ .

The etching of platinum introduces some difficulties: the etch is non-uniform over the wafer. With 3.5 minutes of etching a rim of 5 cm is cleared of platinum but there is still platinum in the centre of the wafer but after 4.5 the centre of the wafer is free of platinum and the rim is cleared of  $\text{PtO}_2$ . The whole wafer contains metal features which makes the non-uniformity not acceptable. Inspection with an optical microscope showed that the  $\text{PtO}_2$  features first got thinner in the width and then lost their protective  $\text{PtO}_2$  layer after which the platinum get thinner in height. The  $\text{PtO}_2$  layer was not selective enough for the needed etch time. The results from different etch times can be seen in figure 5.12.

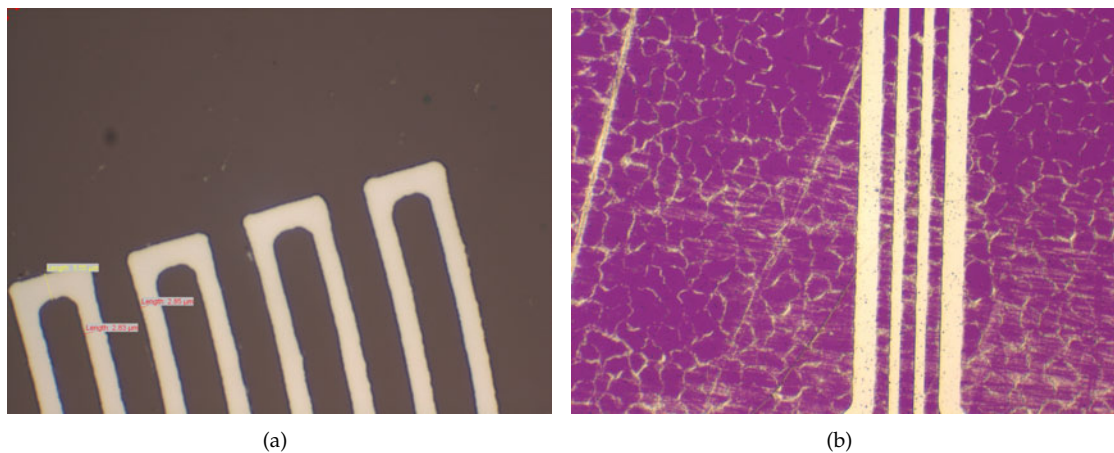


Figure 5.12: The samples in (a) and (b) are etched for 4.5 minutes in aqua regia but the difference in location on the wafer gives also a difference in the progress of etching.

For improving the selectivity of the PtO<sub>2</sub> variations in process pressure of the oxidation were tested. An increase in pressure reduced the DC-bias which results in a less intensive ion bombardment and more chemical reactions which increase the oxide layer on the surface but this could also result in a less thick layer of PtO<sub>2</sub> as the ions penetrate not as far as before. As pressure steps 10, 20, 40 and 80 mTorr were chosen where 10mTorr acted as reference, after the oxidation all the samples were etched in the same batch to ensure the same etch time. All the wafer did show the same result which was indifferent from the reference. To ensure that the non-uniformity was not caused by the temperature gradient in the etchant a quarter piece of wafer was taped in the centre of a bare wafer. This bare wafer was horizontal placed in the etchant which ensured an uniform temperature in the centre of the wafer over the quarter piece. The quarter piece of wafer etched in a gradient from the circular rim to the 90° angle point of the wafer which is normally the centre of a full wafer. The non-uniformity in the etching is caused by the parabolic layer thickness of the sputtered platinum which resulted in the longer etch time in the centre of the wafer. The layer of platinumoxide stayed on the wafer during a Scotch-tape test.

Another test is done with heating of the platinum samples in an oven at 600°C. After a hour at 600°C an optical inspection revealed the forming of grains in the platinum structure. The adhesion of the layer was still the same. All the etch test were done on a roughened SiRN wafer and a clean SiRN wafer with fresh SiRN and it turned out that the platinum on clean SiRN needs no roughing as it adhere with the same strength as on the roughened SiRN.

To solve the problem caused by the non-uniformity another way of metal layer removal was tried: lift-off. Starting with a non-roughened, non-clean SiRN wafer we patterned with the metal mask an 1.7 µm layer of OiR 907-17 without a hard-bake. After development of the patterns a layer of platinum was sputtered on top of the photoresist and bare SiRN. The photoresist was solved with acetone which also releases the layer of platinum on top of the photoresist. With this method we obtain a clear pattern of platinum on the SiRN but as the SiRN was not roughened or fresh the platinum could be peeled of with Scotch-tape.

With this information we can make a new process-flow for adhering platinum to SiRN. The process is started with a SiRN layer which is patterned with the metal mask in an 1.7 µm layer of OiR 907-17 without a hard-bake. After development of the patterns the exposed SiRN is roughened in Tetske with a gas flow of 30 sccm SF<sub>6</sub> and 5 sccm O<sub>2</sub> at a pressure of 7 mTorr with a power of 40W for a time of 30 seconds. The photoresist will also etch by the exposure to the plasma which will result in a thinner layer and wider features. Directly after the roughening a layer of platinum is sputtered on top of the photoresist and bare SiRN. The photoresist is solved with acetone which also releases the layer of platinum on top of the photoresist. To minimize the variation in characteristic of the platinum heaters, due to ageing in operating mode at high temperatures, the platinum is oxidized in Tetske with a gasflow of 20 sccm O<sub>2</sub> at 10mTorr with a power of 32 Watt (Vdc 400V) for a time of 60 seconds. This flow is also described in table 5.4.

## 5.7 Release etch

The patterning for the release etch still experimental and is done by the 'Haneveld' method of using a double layer of 908-35. The etch rate of the resist is structure dependent, the etch rate is determined by heat transfer as hot spots will etch faster than cooler spots. The release etch is done by semi-isotropic etching in the Adixen 100SE. As the processing has not come so far we cannot share any experience on this topic.

## 5.8 Conclusion

The mask fabrication in the cleanroom showed that it is hard to achieve channel slits with the in-house mask writer that are within the design specifications. The way of measuring the width of the slits should also be a point of discussing. The slits are measured by a camera on a microscope which is connected

Platinum lift-off process flow	
Step	Description
1	Priming surface with HMDS at 4000RPM for 30 seconds
2	Spin coating olin OiR 907-17 at 4000RPM for 30 seconds. Pre-exposure bake: 90 seconds at 95°C
3	Alignment and exposure for 4 seconds on the EV620.
4	Post-exposure bake 60 seconds at 120°C. Development in OPD4262 60 seconds. Quick dump rinse and spin drying.
5	SiRN roughing with Tetske. 30 sccm SF <sub>6</sub> , 5 sscm O <sub>2</sub> , pressure 7 mTorr, power 40W, time 30 seconds.
6	Deposition Pt with Sputterke ~25nm/min
7	Ultrasonic lift-off of resist with Aceton 20 minutes and IPA 20 minutes
8	Oxidation Pt with Tetske. 20 sccm O <sub>2</sub> , pressure 10mTorr, power 32 Watt (Vdc 400V), time 60 seconds.

Table 5.4: The process-flow for the platinum process.

to computer. The pixels of the image are translated to the measured size but it is to the judgement of the researcher which pixels are the actual slit and which are just the gradient in the  $\sim 0.3 \mu\text{m}$  transition from the slits to the chromium layer. The researcher has to measure systematic in the same region of this transition from slit to mask to avoid a huge deviation in the measurements, however even with the systematic measurements there is still a standard deviation which is based on a few pixels.

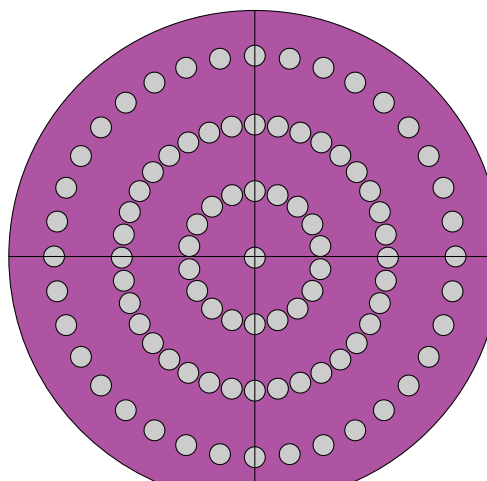
The different fabricated masks showed that using an intensity of  $18\text{mJ}/\text{cm}^2$  gives the best uniformity. Using a designed channel pattern with a width of  $1.5 \mu\text{m}$  will give channel slits that are within specifications, however this mask has still a non-uniformity between the horizontal and vertical slits. From this we can conclude that a combination of both masks could give the best results for producing the perfect channel slits. The deviation in the uniformity was also discussed with the cleanroom mask-maker which suggests that the calibration of the two laser in mask writer could have an off-set. A check revealed that the intensity curves of the spectra of both lasers had an off-set which could be a cause for the resulting non-uniformity. Another option for obtaining better masks is ordering externally, these are produced on other mask making machines with higher accuracy.

The amount of overlap between the access-holes and channel slits was more than expected which was caused by two factors: position dependent angled etching by the DRIE Bosch process and the size of the notching. The position dependent angled etching has never been charted before but this could be done with a simple double side polished SiRN coated test wafer on which radial hole patterns are drawn as is shown in figure 5.13. The etched holes that run through the wafer under an angle will have an increased or decrease distance between the each other at the backside of the wafer. This position dependent angle could be automatically or by hand compensated in the mask designing software.

The size of the notching under the SiRN layer can be reduced by further fine-tuning of the etch time for the access-holes. The DRIE Bosch etching was done in 34 minutes where at 32.5 minutes the opening at the backside had already a size of  $6\text{--}10 \mu\text{m}$ . A reduction of 30 seconds etch time could make the difference and could result in less overlap with the channel-slits.

The process step of removing the photoresist after the semi-isotropic channel etch with the Tepla barrel etcher for 20 minutes has to be replaced. An etch for 5 minutes in the Tepla barrel etcher removes the hardened layer of photoresist after which HNO<sub>3</sub> will remove the rest of the resist. The complete stripping of the resist and part of the chromium was no time saver due to the formed chromiumoxide which took one and a half day to remove.





**Figure 5.13:** A method for measuring the position dependent angle of the DRIE Bosch etching. The distance between the etch holes will increase or decrease when the holes are etched under an angle to the other side.

During the development of a process for the Dupont MX5020 polymer it showed that the polymer was not the perfect solution for covering of the access-holes. The best way for applying the film would be using a heated wafer which is pressed under vacuum conditions against a perfect flat piece of polymer foil to prevent any air bubbles getting trapped. As the channels are connected to the access-holes this would mean that the vacuum in the channels would pull in the foil when it is exposed to the normal air pressure, however a bake of the foil under vacuum conditions could harden it enough to survive this pressure difference. The main reason for not choosing this foil for our process would be the use of the roller as this caused most of the structural damage to the channels and the lacking ability for spanning gaps. There are also other polymer films on the market which may be easier to apply and are more suitable for spanning gaps.

Another alternative would be using a thick photoresist like SU-8 100 with dynamic spinning which flows into the access-holes but which is viscous enough to stop half way the access-hole as the wafer goes on the hotplate to harden and fix the resist. The downside of using the resist would be the intensive cleaning required to remove all the SU-8 out of the access-holes and channels.

The optical microscope inspections which were done to assess the yield of the wafers revealed that the double and triple buried channels are the most sensitive to destruction caused by layer stress and external forces. Almost all the single buried channels were intact from which we can conclude that it is better to split all the double buried channels into two single channels. The exhaust which is composed of a triple channels should also be replaced with three single channels. The combustion channels with the mixer structures had less defects in comparison with the triple channels without the mixers as the pillars give extra support to the channels. A new triple channels design would be building them with pillar support in the centre of the channel like the mixer in figure 4.8.

The adjusting of the process for platinum on SiRN without an adhesion layer has shown that a combination of lift-off with roughing is a new way that has to be tested. The original process developed by Tiggelaar was not usable due to the non-uniform layer thickness of platinum over the wafer. A discussion with Tiggelaar revealed that he had no problems with the PtO<sub>2</sub> selectivity as all his metal features were located in the centre of a smaller wafer. If the layer thickness had been uniform the Tiggelaar method would have worked. He also acknowledged that lift-off with roughing would be a good solution. He had dismissed the lift-off in his research as in that stage the roughing was not included in his processing, which resulted in no adhesion of the platinum on the SiRN.

An approach for reducing the processing time would be leaving the core wafer thickness and adjusting the holder of the chip for extra clearance at the bottom of the core. This removes the KOH etching step

but requires a wafer through DRIE etching of the isolation trench over the thickness of the wafer. The TEOS run proofs that after 16 hours of drying the channels are still not empty. By using dry etching the amount of contact with liquids after the channel formation is minimized.

Using  $\text{XeF}_2$  to etch semi-isotropical channels and the release etch is preferred over  $\text{SF}_6$  plasma as it is more safe for the structures on the wafer. There is less thermal loading and there is a better chuck for holding the wafer but this method is not used as it creates rough features. However the process of etching with  $\text{XeF}_2$  is just at its starting point and futher process development could give smooth walls. At that point the processing should switch to  $\text{XeF}_2$ .





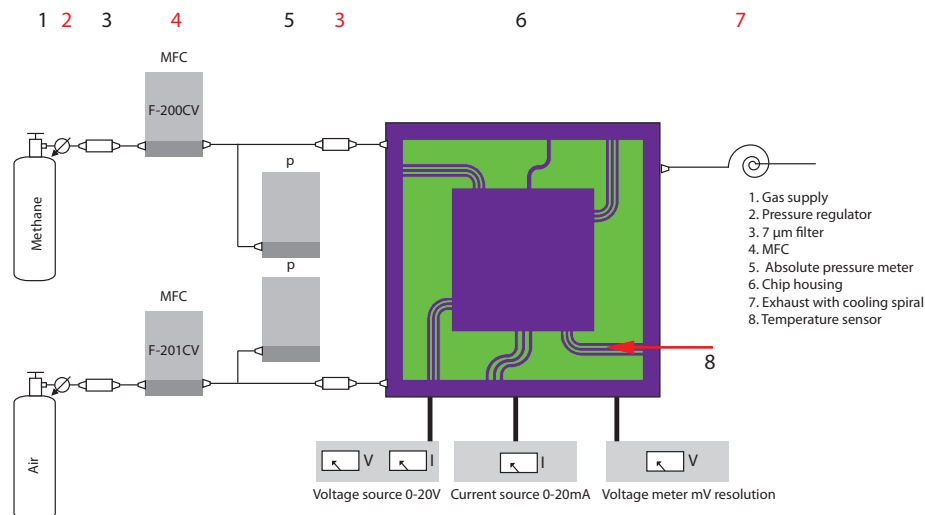
## Chapter 6

# Measurement set-up

In this chapter the realisation of a measurement set-up is discussed. This set-up enables the steering of the heaters and the measuring of the temperature sensors which are located on top of the chip. By following the measurement protocol the characteristics of the calorific sensor can be determined and calibrated. With these characterisation the calorific value and Wobbe-index can be calculated.

### 6.1 Set-up

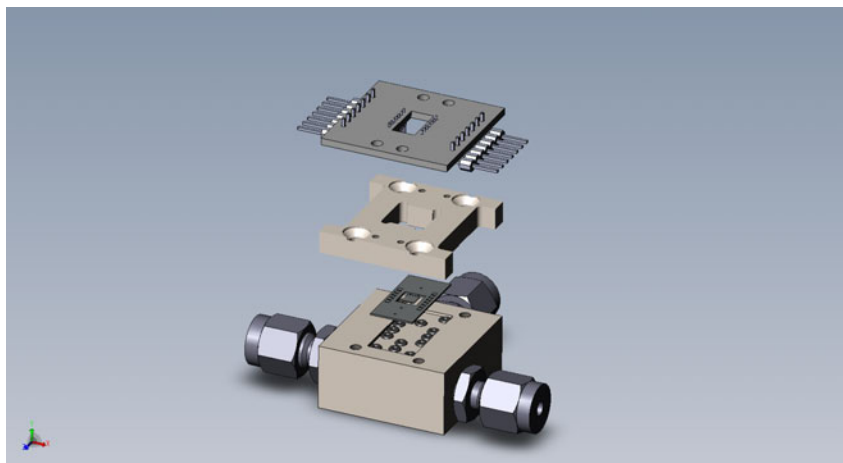
The measurement set-up (figure 6.1) is fed with gasses supplied from bottles with pressure regulators. Two mass flow controllers, the Bronkhorst F-200-CV and F-201CV, are used for the regulation of air (1-0.2 g/h) and methane (0.1-0.02 g/h) flow with a 2 bar pressure-drop by the controller and a working range of 2-5 bar for the device.



**Figure 6.1:** The measurement set-up with the flow controllers, pressure meters, filters and chip.

The chip is mounted in an aluminium holder on top of o-rings with clamping from the top with another aluminium block. The aluminium holder acts as a heatsink with its good heat conducting properties and its natural oxide layer which makes it practical inert to the gasses. Thermal past is applied between the aluminium and the chip for optimal thermal contact. The holder with clamp is shown in figure 6.2.

The gasses supplied to and from the MFC's are inline filtered with a 7 µm filter and are connected to the holder with #10-32 thread gasket sealed connectors. It is also possible to use Upchurch connectors



**Figure 6.2:** The holder for the chip in an exploded view. From bottom to top: the holder with o-rings, the chip, the clamp and the pcb with spring-loaded pens.

with internal sealing at ferrule. These connector require stricter drilling specifications for the threads in the holder which increase the production costs but decrease the packaging size. A pressure sensor is placed in front of the filter to the block to measure the pressure drop over the chip. The holder routes internally the gasses to the in-/outlets of the chip which are sealed with o-rings. The filters are used to prevent the clogging of the chip with particles.

The gas flows are in the range of 0.1-1 gram per hour or its equivalent 3-13 millilitre per minute which requires using 1/16" piping to reduce the internal volume of the piping. For the issue of safety we use stainless steel as the material for the piping which makes the piping also suitable to be used at the exhaust side of the chip holder. A heat exchanger can be made out of the tubing by creating a spiral tube at the exhaust to safely dispose the combustion gasses.

The bond-pads of the heaters and temperature sensors on the chip are connected by spring-loaded pens to a pcb (figure 6.3) and can carry a current up to 3 ampère which is far more than a single bond-wire. The temperature sensors are measured with a 4-point measurement where the current source is set on 1 mA and the resulting voltage will be measured with a resolution of 1 mV. The heaters are connected to a voltage source with current limiting capabilities.

The pcb with the spring-loaded pens will be mounted on top of the clamp. The chip has a margin of 0.5mm to each side of the holder and needs to be aligned in the centre of the holder and this ensures that the gas connections are also correctly aligned. The spring-loaded pens can be finely aligned as the screw-holes on the pcb have a margin of 0.3mm to each side. The clamping block has extra spacing for the spring-loaded pens to allow movement of the pcb. The clamping block covers as much as possible from the top of the chip and was limited through the platinum tracks that lay on top of the chip. The chip is mounted in the holder with enough pressure from the clamp for a gas-tight connection. The holder, clamp and pcb are all made to order by the specifications given in the blueprints in appendix D. By using a construction with spring-loaded pens a flexible test environment is created and in the case that a chip is destroyed it can easily be swapped. The signals from the spring-loaded pens are routed over the pcb to headers which are mounted on the side. The total package chip is shown in figure 6.4.

## 6.2 Measurement protocol

The final goal of the proof-of-concept is to measure a value that is related to the caloric-value of the gas. The easiest way for calibration would be using a calibrated thermal-imaging device but such a device is currently not available.

The combustion energy can be determined in two ways: discrete flow and continuous flow. Measuring with a discrete flow means that the combustion energy is found by filling the combustion chamber

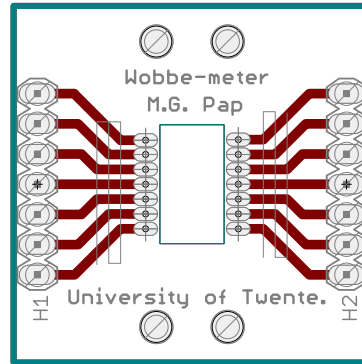


Figure 6.3: The pcb for the electrical connections to the chip. The dimension can be found in figure D.5

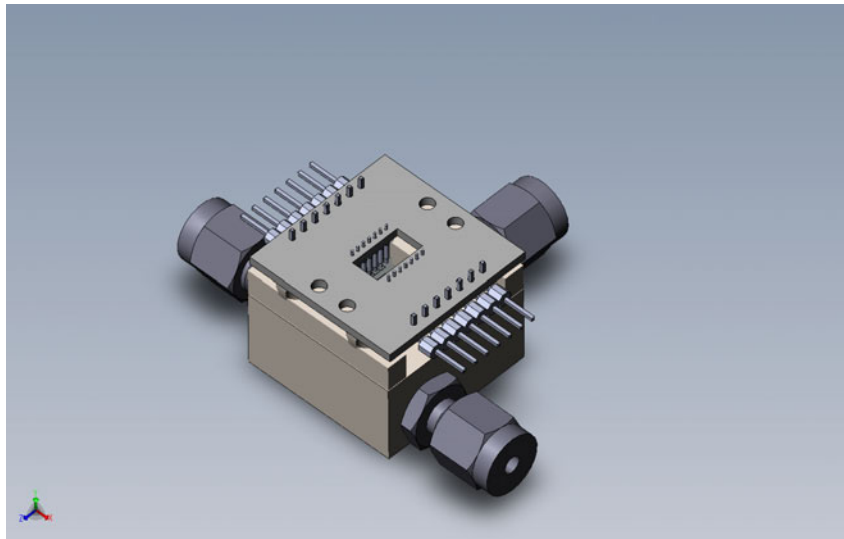


Figure 6.4: The packaged chip in an imploded view.

in the chip with an oxidizer and fuel, by stopping the flow diffusion mixing happens in the chamber and after a set time the mixture is ignited with the core heater. This method only ignites the mixture that is available in the chamber. The combustion energy is the temperature increase of the core which is generated on top of the temperature of the core heater. The final core temperature should be compensated for the thermal losses. Measuring with a continuous flow gives the possibility to measure with a thermal balance. A flow of oxidizer and fuel enter the combustion chamber and auto-ignited due to the pre-heat. The combustion energy heats the core and by extra heating can be done with the core heater until the wanted core temperature is achieved. In this way the amount of power fed to the heater can be related to the combustion energy.

The design of the chip is optimized for measuring with a continuous flow. The following steps can be used for characterisation of the chip. As initial calibration gas industrial methane is used, after successful testing with the calibration gas other mixtures with different calorific values such as a methane/nitrogen blend can be used for further calibration and to test the linearity of the sensor.

First the temperature sensing elements that are located on the beams need to be tested with a simple test: the voltage at room-temperature is measured and then the elements are heated with a heat-gun at set temperatures to observe a voltage increase which are related to the set temperatures.

Second the heater on top of the core is used, beginning at a power of 10 mW which is increased in steps of 10 mW to 100 mW. Every step a measurement is taken with temperature sensing element. We expect an almost linear relation between the power and measured voltage at these low power levels. If

the produced square core in the chip is near the specifications of the design we can expect with  $1.49 \cdot 10^{-3} \text{ J/K}$  and a power increase of 10-100mW a core temperature increase of 6.7K-67K which correspond to a  $\Delta V$  of  $0.45 \cdot (6.7-67) \text{ mV}$ . After the low power measurements a sweep is done from 100mW to 1W in 100mW steps to obtain a better fitting of the convection and radiative losses. With the found values we can do "reverse calorimetry" by calculating the specific heat capacity of the bulk as  $C_p = \Delta Q / (\Delta T \cdot m)$ . The non-linearity is caused by the loss factors of the convection and radiation. Measuring in vacuum surroundings would be preferable as this eliminates the convective term in the thermal losses.

Third the convective and conductive heat transfer is tested from each gas-heater to the core which uses in the first test no gas and in the second test compressed air at a fixed flow. This is done at a power of 10-100 mW which increased in 10 mW steps where the  $\Delta V$  of the sensing elements is measured. The difference between the temperatures of the tests gives the convective heat transfer to the core. In the case that the conduction through the SiRN is much bigger both tests will give the same results. The temperature of the exhaust gas should be measured to obtain the thermal loss of heat through the exhaust with this the convective transfer to the core can be calculated.

Fourth the combustion is tested by applying the lowest setting of the MFC's with the correct mixing ratio's while igniting the flows with the heaters at fixed maximum power. The stoichiometric flow is stepwise increased to obtain the relation between the temperature increase per time unit and the flow. In case the gas does not ignite the methane flow is fixed at 1/50 of the nominal flow of the MFC and the air flow is swept to obtain a combustion. With the characterisation of the chip the calorific-value can be calculated and compared with the real calorific-value of the calibration gas. The calorific-value can be calculated by inserting the measured temperature in equation 6.1. The term  $\Delta Q$  has to be compensated with the found relation in the second step for the convection and radiative losses and the pre-heat energy of  $\int_{T_0}^{T_{pre-heat}} C_p dt$ .

$$\begin{aligned}
 T_{core} &= \frac{\frac{V}{1.07 \cdot 10^{-3}} - 0.55 \cdot T_{base}}{0.45} [K] \\
 \Delta Q_{combustion} &= \frac{T_{core-end}(t) - T_{core-begin}(t)}{dt} \frac{1}{\rho_{core} \cdot V_{core} \cdot C_{p,core}} + Q_{losses} [J/s] \\
 \phi_V &= \frac{\frac{\phi_m [g/h]}{1000 \cdot 3600}}{\rho_{methane}} [m^3/s] \\
 \text{Calorific value} &= \phi_V \cdot \frac{\Delta Q}{\Delta t} - \frac{\phi_m [g/h]}{1000 \cdot 3600} \int_{T_0}^{T_{pre-heat}} C_p dT [J/m^3] \quad (6.1)
 \end{aligned}$$

As fifth the creation of a thermal balance is be tested by setting the flow for the combustion at its lowest setting and heating with the core heater to achieve a final temperature measured with the temperature sensors on the beams. Stepwise the combustion heat is increase by regulating the gas flow and the power to the core heater while maintaining an equilibrium in temperature. The relation between the power and calorific value of the combustion can be calibrated by using the pre-measured calorific value of the calibration gas. Future calorific-values of the gasses can be calculated with the relation obtained by the measured power to combustion heat ratio. In the case that physical properties of the losses and heaters do not change the heater power to calorific-value can be found with equation 6.2 with  $C$  as the calibration constant.

Obtaining the  $C_p$  of the unknown gas cannot be done without an extra thermal flow sensor with known characteristics in front of the calorific sensor. The  $C_p$  can be calculated out of the measured heat transfer in the thermal flow sensor, the preheat-energy can be calculated by combining these measurements with the mass-flow measured in the micro-coriolis and the temperature of the heater. These thermal flow sensors which are also based on the micro-coriolis technology are currently in development and could be integrated in the chip. For the purpose of calibration the  $C_p$  of the calibration gas is used for calculating the pre-heat energy.

The Wobbe-index can be calculated by combining (6.2) and (3.22). The Wobbe-index (higher heating value) of the industrial calibration gas is  $50.72 \text{ MJ/m}^3$ , a subtraction of  $4.86 \text{ MJ/m}^3$  gives the lower heating value of  $45.86 \text{ MJ/m}^3$  which can be compared with the measured value of the calorific sensor.

$$\begin{aligned}
T_{core} &= \frac{\frac{V}{1.07 \cdot 10^{-3}} - 0.55 \cdot T_{base}}{0.45} [K] \\
Q_{heater} &= \frac{T_{core}}{dt} (\rho_{core} \cdot V_{core} \cdot C_{p,core}) - Q_{combustion} + Q_{losses} [J/s] \\
\phi_V &= \frac{\frac{\phi_m [g/h]}{1000 \cdot 3600}}{\rho_{methane}} [m^3/s] \\
Calorific\ value &= \phi_V \cdot C \cdot Q_{heater} - \frac{\phi_m [g/h]}{1000 \cdot 3600} \int_{T_0}^{T_{pre-heat}} C_p dT [J/m^3] \tag{6.2}
\end{aligned}$$

In the case that the gas does not ignite an external concentrated light source can be used for heating up the core to start the combustion. The heat added with the light source can be measured with the temperature sensors. If this fails the gas can be pre-mixed in a long capillary for obtaining an ignition with the heaters or light source.

For estimation of the stresses in the chip during heating a mechanical characterization of the chip could be done by measuring the deflection of the beams and core with a laser-vibrometer.

### 6.3 Conclusion

The measurement set-up described in this chapter provides a flexible testing environment for characterisation of the calorific sensor. An extra addition of a thermal flow sensor to the set-up was not mentioned earlier in the report but is required to measure the  $C_p$  of unknown gasses for determining the pre-heat energy. For the purpose of calibration the  $C_p$  of the calibration gas can be used. At the moment of writing the fabrication of the chip in the cleanroom was not completed. This did not enable us to make any measurements which were needed to verify the working of the proof-of-concept.



## Chapter 7

# Conclusion

With help of MEMS technology a new approach was created for the realization of an on-chip Wobbe-index metering solution. The use of MEMS technology for a metering solution gives a reduction in size and costs which can be a huge benefit for the (bio-)gas industry. The on-chip implementation would require measuring of the calorific value, the mass flow and the relative density. There is already an on-chip solution for measurement of the relative density and mass flow within the department of Transducer Science and Technology (TST) at the University of Twente: the micro-coriolis flow sensor. The goal of this project was to do a feasibility study for a proof-of-concept of an on-chip calorific sensor which can be integrated with the micro-coriolis flow sensor. The result of this integration gives a sensor with which the Wobbe-index of a gas can be derived.

The literature research revealed that the process of laminar diffusion flow combustion inside micro-channels is still unknown. This complicated the designing of the calorific sensor and forced the use of assumptions about the process of the combustion. Four different combustion chambers were created for research into combustion in micro-channels, which were implemented in two different chip designs. These combustion chambers are based on a new method for creation of buried channel micro-mixers.

For testing the chips a measurement set-up was realised which enables making gas connections to the chip while thermal cooling is provided during the measurements. This enables doing measurements to determine the calorific value of industrial methane which is used as calibration gas.

The development of the chip in the cleanroom has delivered two new processing flows, where the first describes the usage of the Dupont MX5020 polymer foil for lithography on wafers with topography and the second describes the process of adhering platinum onto silicon-rich nitride which makes it suitable to use in high temperature micro-heaters.

Creating the access-holes and buried channels are proven methods for creating fluid channels in the wafer. Using of the polymer foil had an impact on the yield of the wafers which reduces the yield with 90%, however there are more polymer foils or photoresists on the market with more suitable properties which can form an alternative. The platinum on silicon-rich nitride with adhesion layer had some minor glitches but the new proposed process flow can be the solution. It is wise to use only dry processing steps after the creation of the channel as the capillary working of the channels can create some difficulties. For completion of the chip in the cleanroom the fabrication steps of the platinum heaters based on the lift-off and the isolation of the core have to be done. Solutions were found for all the encountered problems and led to alternative processing steps for future processing. Creating of a calorific sensor with the current technology is deemed feasible. After completion of the production the chip should be characterised and calibrated to verify the working of the proof-of-concept.

The realisation of the proof-of-concept is near to its completion with a complete cleanroom process flow which was tailor-made for the integration of the calorific sensor and the micro-coriolis sensor into one device: the Wobbe-meter.





## Chapter 8

# Recommendations

The production of the almost complete chip should be finished for the verification of the proof-of-concept.

The calculations for the losses are based on the assumption that the rim of the chip is kept at room temperature through the holder but for verification a temperature sensor should be included in the new design on the rim of the chip.

Further research should be done to see if the length of the combustion chamber influences the complete combustion or that the reaction creates a steady flamelet at the point of the colliding flows as was stated in [42]. Insight in the combustion location would give better guidelines for the chip design.

Testing has to prove the reliability of the heaters. In case of electro-migration the metal patterns on the chip should be redesigned. In the new design the error in the spacing of the bondpads could also be fixed.

The integration of thermal flow sensors on the Wobbe-meter is needed to add capabilities for measuring the  $C_p$  which is required for determining the pre-heat energy.

The density, thermal capacity, thermal conductivity and the surface emissivity of the low stress SiRN out of the G3 tube have to be measured for better accuracy of the models.

Research could be done into the use of the Dupont MX5020 for other applications and some tests could be done to determine the influence of a hard-bake on the promotion of further polymer linkage.

The process of DRIE Bosch etching in the Adixen SE100 creates a position dependent angle of the access-holes. The characterisation of this problem could help avoiding the overlap of channel slits and access-holes in the future.

Research could be done into useful applications for the buried channels micro-mixers.



# Appendices



# Appendix A

## Material properties

Gas	Molar mass [g/mol]	Collision diameter [Å]
Air	28.95	3.617
O <sub>2</sub>	31.9988	3.433
CH <sub>4</sub>	16.043	3.746
H <sub>2</sub> O	18.01528	2.75
CO <sub>2</sub>	44.01	3.996

**Table A.1:** Molar mass and collision diameter of gasses.

Material	Poisson ratio $\nu$	$\alpha_T$	$E$ [GPa]	$k$ [W/m.K]	$\rho$ [kg/m <sup>3</sup> ]	$C_p$ [J/kg·K]
Platinum (Pt)	0.39	$8.8 \cdot 10^{-6}$	168	148	21400	132
SiRN	0.27	$8.8 \cdot 10^{-6}$	290	27	3310	711
Si	0.22	$2.2 \cdot 10^{-6}$	165	148	2330	713

**Table A.2:** Material properties

	CH <sub>4</sub>	O <sub>2</sub>	CO <sub>2</sub>	H <sub>2</sub> O(g)	Air
Density ( $\rho$ ) [kg/m <sup>3</sup> ]	0.656	1.308	1.799	0.9970 k	1.20
Heat capacity $C_p$ [ $\frac{J}{kg \cdot K}$ ]	2237	918	850	1865.11	1010.00
Heat capacity $C_v$ [ $\frac{J}{kg \cdot K}$ ]	1714	659	657	1412	719
Molar mass (g/mol)	16.043	31.999	44.010	18.015	28.95

**Table A.3:** Chemical components 25°C, 101.325 kPa.



## Appendix B

# Clewin scripts

Here below the LUA scripts are defined which are used in Clewin for the patterning of the channel-slits.

**Listing B.1:** Internal clewin script

```
1 pattern = {}
2
3 --[[
4 pattern_length = 16
5 pattern[1] = {1,1,1,1,1,1,0,0,0,0,1,1,1,1,1}
6 pattern[2] = {1,1,0,0,0,0,0,1,1,0,0,0,0,0,1}
7 pattern[3] = {0,0,0,1,1,1,1,1,1,1,1,1,1,1,0}
8 ]]--
9 --[[
10 pattern_length = 20
11 pattern[1] = {1,1,1,1,1,1,1,0,0,0,0,1,1,1,1,1,1}
12 pattern[2] = {1,1,1,0,0,0,0,0,1,1,1,1,0,0,0,0,1,1}
13 pattern[3] = {0,0,0,1,1,1,1,1,1,1,1,1,1,1,1,1,0,0}
14 ]]--
15 --[[
16 pattern_length = 24
17 pattern[1] = {1,1,1,1,1,1,1,1,1,0,0,0,0,1,1,1,1,1,1,1}
18 pattern[2] = {1,1,1,1,0,0,0,0,0,1,1,1,1,1,1,0,0,0,0,1,1}
19 pattern[3] = {0,0,0,1,1,1,1,1,1,1,1,1,1,1,1,1,1,1,1,0,0}
20 ]]--
21
22 --[[
23 pattern_length = 28
24 pattern[1] = {1,1,1,1,1,1,1,1,1,1,1,0,0,0,0,1,1,1,1,1,1,1,1,1,1}
25 pattern[2] = {1,1,1,1,1,0,0,0,0,0,1,1,1,1,1,1,1,1,0,0,0,0,1,1,1,1}
26 pattern[3] = {0,0,0,1,1,1,1,1,1,1,1,1,1,1,1,1,1,1,1,1,1,1,1,1,0}
27 ]]--
28
29
30 pattern_length = 32
31 pattern[1] = {1,1,1,1,1,1,1,1,1,1,1,1,1,0,0,0,0,1,1,1,1,1,1,1,1,1,1,1}
32 pattern[2] = {1,1,1,1,1,1,0,0,0,0,0,1,1,1,1,1,1,1,1,1,0,0,0,0,1,1,1,1}
33 pattern[3] = {0,0,0,1,1,1,1,1,1,1,1,1,1,1,1,1,1,1,1,1,1,1,1,1,1,1,0,0}
34
35 --[[
36 pattern_length = 2
37 pattern[1] = {1,1}
38 pattern[2] = {1,1}
39 pattern[3] = {1,1}
40 ]]--
41
42
43 pattern_counter = 1
44 CHANNEL_H =5
45 CHANNEL_W =1.5
46 SPACING =3
47
48 LANES = 3
49 BEND_RADIUS =80
50 ETCH_WIDTH = 40
51 SERPENTINE = 4
52 START_LENGTH = 1200
53 TOTAL_LENGTH = 0
```

---

```

54 INTERCHANNEL_SPACING = 30
55 CHANNEL_SPACING = 180 +(2*INTERCHANNEL_SPACING)
56 NO_PATTERN = TRUE
57
58 dofile("wobbe.lua")
59 —dofile("testpatterns.lua")
60 —dofile("single_serpentine.lua")
61
62 —dofile("multi_serpentine.lua")
63
64 endx, endy = straight_multi(0,0,1976,90)
65 endx, endy = arc_multi(endx, endy, 4, "CW", 56)
66 endx, endy = arc_multi(endx, endy, 2, "CCW", 56)

```

---

Listing B.2: Wobbe.lua

```

1 function arc(startx, starty, quadrant, direction, radius)
2   TOTAL_LENGTH = TOTAL_LENGTH + (math.pi/2)*radius
3   setlayer(1)
4   cornerLength = (math.pi/2)*radius
5   elements = math.floor(cornerLength/(CHANNEL_H+SPACING))
6   elementAngle = ((math.pi/2)/elements)
7
8   —top_right = 1, bottom_right = 2, bottom_left = 3, top_left = 4
9   if quadrant ==1 then
10    if direction == "CCW" then
11      for j=0,elements,1 do
12        x = startx + math.cos(elementAngle*j)*radius - radius
13        y = (starty + math.sin(elementAngle*j)*radius) + (CHANNEL_H/2)
14        setlayer(1)
15        box(x,y,CHANNEL_W, CHANNEL_H,(90/elements)*j)
16        endv = j
17        setlayer(2)
18        circle(x,y,ETCH_WIDTH/2)
19      end
20      endx = startx + math.cos(elementAngle*endv)*radius - radius - (CHANNEL_H/2) - SPACING
21      endy = (starty + math.sin(elementAngle*endv)*radius) + (CHANNEL_H/2)
22    else
23      for j=elements,0,-1 do
24        x = startx + (CHANNEL_H/2) + math.cos(elementAngle*j)*radius
25        y = (starty + math.sin(elementAngle*j)*radius) - radius
26        setlayer(1)
27        box(x,y,CHANNEL_W, CHANNEL_H,(90/elements)*j)
28        endv = j
29        setlayer(2)
30        circle(x,y,ETCH_WIDTH/2)
31      end
32      endx = startx + (CHANNEL_H/2) + math.cos(elementAngle*endv)*radius
33      endy = (starty + math.sin(elementAngle*endv)*radius) - radius - (CHANNEL_H/2) - SPACING
34    end
35  elseif quadrant ==2 then
36    if direction == "CCW" then
37      for j=elements,0,-1 do
38        x = startx + math.cos(elementAngle*-j)*radius + (CHANNEL_H/2)
39        y = (starty + math.sin(elementAngle*-j)*radius)+radius
40        setlayer(1)
41        box(x,y,CHANNEL_W, CHANNEL_H,(90/elements)*-j)
42        endv = -j
43        setlayer(2)
44        circle(x,y,ETCH_WIDTH/2)
45      end
46      endx = startx + math.cos(elementAngle*endv)*radius + (CHANNEL_H/2)
47      endy = (starty + math.sin(elementAngle*endv)*radius)+radius + (CHANNEL_H/2) + SPACING
48    else
49      for j=0,elements,1 do
50        x = startx + math.cos(elementAngle*-j)*radius - radius
51        y = (starty + math.sin(elementAngle*-j)*radius) - (CHANNEL_H/2)
52        setlayer(1)
53        box(x,y,CHANNEL_W, CHANNEL_H,(90/elements)*-j)
54        endv = -j
55        setlayer(2)
56        circle(x,y,ETCH_WIDTH/2)
57      end
58      endx = startx + math.cos(elementAngle*endv)*radius -radius - (CHANNEL_H/2) - SPACING
59      endy = (starty + math.sin(elementAngle*endv)*radius) - (CHANNEL_H/2)
60    end
61  elseif quadrant ==3 then
62    if direction == "CCW" then

```

---



```
63     for j=0,elements,1 do
64         x = startx - math.cos(elementAngle*j)*radius + radius
65         y = (starty - math.sin(elementAngle*j)*radius)-(CHANNEL_H/2)
66         setlayer(1)
67         box(x,y,CHANNEL_W, CHANNEL_H,(90/elements)*j)
68         endv = j
69         setlayer(2)
70         circle(x,y,ETCH_WIDTH/2)
71     end
72     endx = startx - math.cos(elementAngle*endv)*radius + radius + (CHANNEL_H/2)+ SPACING
73     endy = (starty - math.sin(elementAngle*endv)*radius) - (CHANNEL_H/2)
74 else
75     for j=elements,0,-1 do
76         x = startx - math.cos(elementAngle*j)*radius - (CHANNEL_H/2)
77         y = (starty - math.sin(elementAngle*j)*radius + radius)
78         setlayer(1)
79         box(x,y,CHANNEL_W, CHANNEL_H,(90/elements)*j)
80         endv = j
81         setlayer(2)
82         circle(x,y,ETCH_WIDTH/2)
83     end
84     endx = startx - math.cos(elementAngle*endv)*radius - (CHANNEL_H/2)
85     endy = (starty - math.sin(elementAngle*endv)*radius + radius) + (CHANNEL_H/2) +SPACING
86 end
87 elseif quadrant ==4 then
88     if direction == "CCW" then
89         for j=elements,0,-1 do
90             x = startx - math.cos(elementAngle*-j)*radius - (CHANNEL_H/2)
91             y = (starty - math.sin(elementAngle*-j)*radius) -radius
92             setlayer(1)
93             box(x,y,CHANNEL_W, CHANNEL_H,(90/elements)*-j)
94             endv = -j
95             setlayer(2)
96             circle(x,y, ETCH_WIDTH/2)
97         end
98         endx = startx - math.cos(elementAngle*endv)*radius - (CHANNEL_H /2)
99         endy = (starty - math.sin(elementAngle*endv)*radius) -radius -SPACING - (CHANNEL_H /2)
100     else
101         for j=0,elements,1 do
102             x = startx - math.cos(elementAngle*-j)*radius + radius
103             y = (starty - math.sin(elementAngle*-j)*radius + (CHANNEL_H/2) )
104             setlayer(1)
105             box(x,y,CHANNEL_W, CHANNEL_H,(90/elements)*-j)
106             endv = -j
107             setlayer(2)
108             circle(x,y,ETCH_WIDTH/2)
109         end
110         endx = startx - math.cos(elementAngle*endv)*radius + (CHANNEL_H/2) + radius +SPACING
111         endy = (starty - math.sin(elementAngle*endv)*radius ) + (CHANNEL_H/2)
112     end
113 end
114
115 return endx, endy
116 end
117
118 function straight(startx, starty, length, angle)
119 C_angle = math.cos((2*math.pi*angle)/360)
120 S_angle = math.sin((2*math.pi*angle)/360)
121 TOTAL_LENGTH = TOTAL_LENGTH + length
122 if length == 0 then
123     return startx, starty
124 end
125 N_elements = math.floor(length/(CHANNEL_H+SPACING))
126 for i=0,N_elements-1,1 do
127     x = startx + C_angle*(CHANNEL_H/2) + C_angle*i*(CHANNEL_H+SPACING)
128     y = starty + S_angle*(CHANNEL_H/2) + S_angle*i*(CHANNEL_H+SPACING)
129     setlayer(1)
130     box(x,y, CHANNEL_W, CHANNEL_H, (angle+90))
131     setlayer(2)
132     circle(x,y,ETCH_WIDTH/2)
133     endv = i
134 end
135 endx = startx + C_angle*(CHANNEL_H+SPACING) + C_angle*(endv)*(CHANNEL_H+SPACING)
136 endy = starty + S_angle*(CHANNEL_H+SPACING) + S_angle*(endv)*(CHANNEL_H+SPACING)
137
138 return endx, endy
139 end
140
```

---

```

141 function straight_multi(startx, starty, length, angle)
142   C_angle = math.cos((2*math.pi*angle)/360)
143   S_angle = math.sin((2*math.pi*angle)/360)
144   C_angle2 = math.cos((2*math.pi*(90-angle))/360)
145   S_angle2 = math.sin((2*math.pi*(90-angle))/360)
146   x={}
147   y={}
148   TOTAL_LENGTH = TOTAL_LENGTH + length
149
150   if length == 0 then
151     return startx, starty
152   end
153   odd_even = LANES % 2
154   lower = -math.floor(LANES/2)
155
156   N_elements = math.floor(length/(CHANNEL_H+SPACING))
157   for i=0,N_elements-1,1 do
158
159     if odd_even ==1 then
160       for k=1,LANES,1 do
161         x[k] = startx - C_angle2*(lower+(k-1))*INTERCHANNEL_SPACING + C_angle*(
162           CHANNEL_H/2) + C_angle*i*(CHANNEL_H+SPACING)
163         y[k] = starty + S_angle2*(lower+(k-1))*INTERCHANNEL_SPACING + S_angle*(
164           CHANNEL_H/2) + S_angle*i*(CHANNEL_H+SPACING)
165       end
166     else
167       for k=1,LANES,1 do
168         x[k] = startx - C_angle2*((lower+(k-1))+0.5)*INTERCHANNEL_SPACING + C_angle
169           *(CHANNEL_H/2) + C_angle*i*(CHANNEL_H+SPACING)
170         y[k] = starty + S_angle2*((lower+(k-1))+0.5)*INTERCHANNEL_SPACING + S_angle
171           *(CHANNEL_H/2) + S_angle*i*(CHANNEL_H+SPACING)
172       end
173     end
174
175     for j=1,LANES,1 do
176       if pattern[j][pattern_counter] == 1 or NO_PATTERN then
177         setlayer(1)
178         box(x[j],y[j], CHANNEL_W, CHANNEL_H, (angle+90))
179         setlayer(2)
180         circle(x[j],y[j],ETCH_WIDTH/2)
181       end
182     end
183
184     if not NO_PATTERN then
185       pattern_counter = pattern_counter +1
186       if pattern_counter > pattern_length then
187         pattern_counter = 1
188       end
189     end
190
191   end
192
193   endx = startx + C_angle*(CHANNEL_H+SPACING) + C_angle*(N_elements-1)*(CHANNEL_H+SPACING)
194   endy = starty + S_angle*(CHANNEL_H+SPACING) + S_angle*(N_elements-1)*(CHANNEL_H+SPACING)
195
196   return endx, endy
197 end
198
199 function arc_multi(startx, starty, quadrant, direction, radius_bend)
200   TOTAL_LENGTH = TOTAL_LENGTH + (math.pi/2)*radius_bend
201   odd_even = LANES % 2
202   lower = -math.floor(LANES/2)
203   radius = {}
204   elements = {}
205   elementAngle = {}
206
207   if odd_even == 1 then
208     for i=1,LANES,1 do
209       radius[i] = (radius_bend+(lower+(i-1))*INTERCHANNEL_SPACING)
210       elements[i] = math.floor(((math.pi/2)*radius[i])/(CHANNEL_H+SPACING))
211       elementAngle[i] = ((math.pi/2)/elements[i])
212     end
213   else
214     for i=1,LANES,1 do
215       radius[i] = (radius_bend+(lower+(i-1))+0.5)*INTERCHANNEL_SPACING)
216       elements[i] = math.floor(((math.pi/2)*radius[i])/(CHANNEL_H+SPACING))
217       elementAngle[i] = ((math.pi/2)/elements[i])
218     end
219   end
220
221   —top_right = 1 , bottom_right = 2, bottom_left = 3, top_left = 4

```

---

```
215     if quadrant ==1 then
216         if direction == "CCW" then
217             for k=1,LANES,1 do
218                 for j=0,elements[k],1 do
219                     x= startx + math.cos(elementAngle[k]*j)*radius[k] - radius_bend
220                     y= (starty + math.sin(elementAngle[k]*j)*radius[k]) + (CHANNEL_H/2)
221                     setlayer(1)
222                     box(x,y,CHANNEL_W, CHANNEL_H*(90/elements[k])*j)
223                     setlayer(2)
224                     circle(x,y,ETCH_WIDTH/2)
225                 end
226             end
227             endx = startx + math.cos(math.pi/2)*radius_bend - radius_bend - (CHANNEL_H/2) - SPACING
228             endy = starty + math.sin(math.pi/2)*radius_bend + (CHANNEL_H/2)
229         else
230             for k=1,LANES,1 do
231                 for j=elements[k],0,-1 do
232                     x = startx + (CHANNEL_H/2) + math.cos(elementAngle[k]*j)*radius[k]
233                     y = starty + math.sin(elementAngle[k]*j)*radius[k] - radius_bend
234
235                     setlayer(1)
236                     box(x,y,CHANNEL_W, CHANNEL_H*(90/elements[k])*j)
237                     setlayer(2)
238                     circle(x,y,ETCH_WIDTH/2)
239                 end
240             end
241             endx = startx + math.cos(0)*radius_bend + (CHANNEL_H/2)
242             endy = starty + math.sin(0)*radius_bend - radius_bend - (CHANNEL_H/2) - SPACING
243         end
244     elseif quadrant ==2 then
245         if direction == "CCW" then
246             for k=1,LANES,1 do
247                 for j=elements[k],0,-1 do
248                     x = startx + math.cos(elementAngle[k]*-j)*radius[k] + (CHANNEL_H/2)
249                     y = (starty + math.sin(elementAngle[k]*-j)*radius[k]) + radius_bend
250                     setlayer(1)
251                     box(x,y,CHANNEL_W, CHANNEL_H*(90/elements[k])*-j)
252                     setlayer(2)
253                     circle(x,y,ETCH_WIDTH/2)
254                 end
255             end
256             endx = startx + math.cos(0)*radius_bend + (CHANNEL_H/2)
257             endy = starty + math.sin(0)*radius_bend + radius_bend + (CHANNEL_H/2) + SPACING
258         else
259             for k=1,LANES,1 do
260                 for j=0,elements[k],1 do
261                     x = startx + math.cos(elementAngle[k]*-j)*radius[k] - radius_bend
262                     y = (starty + math.sin(elementAngle[k]*-j)*radius[k] - (CHANNEL_H/2))
263                     setlayer(1)
264                     box(x,y,CHANNEL_W, CHANNEL_H*(90/elements[k])*-j)
265                     setlayer(2)
266                     circle(x,y, ETCH_WIDTH/2)
267                 end
268             end
269             endx = startx + math.cos(-math.pi/2)*radius_bend - radius_bend - (CHANNEL_H/2) - SPACING
270             endy = starty + math.sin(-math.pi/2)*radius_bend - (CHANNEL_H/2)
271         end
272     elseif quadrant ==3 then
273         if direction == "CCW" then
274             for k=1,LANES,1 do
275                 for j=0,elements[k],1 do
276                     x = startx - math.cos(elementAngle[k]*j)*radius[k] + radius_bend
277                     y = starty - math.sin(elementAngle[k]*j)*radius[k] - (CHANNEL_H/2)
278                     setlayer(1)
279                     box(x,y,CHANNEL_W, CHANNEL_H*(90/elements[k])*j)
280                     setlayer(2)
281                     circle(x,y,ETCH_WIDTH/2)
282                 end
283             end
284
285             endx = startx - math.cos(math.pi/2)*radius_bend + radius_bend + (CHANNEL_H/2)+ SPACING
286             endy = starty - math.sin(math.pi/2)*radius_bend - (CHANNEL_H/2)
287         else
288             for k=1,LANES,1 do
289                 for j=elements[k],0,-1 do
290                     x = startx - math.cos(elementAngle[k]*j)*radius[k] - (CHANNEL_H/2)
291                     y = starty - math.sin(elementAngle[k]*j)*radius[k] + radius_bend
292                     setlayer(1)
```

---

```

293         box(x,y,CHANNEL_W, CHANNEL_H,(90 / elements[k])*j)
294         setlayer(2)
295         circle(x,y,ETCH_WIDTH/2)
296     end
297 end
298
299     endx = startx - math.cos(0)*radius_bend - (CHANNEL_H/2)
300     endy = starty - math.sin(0)*radius_bend + radius_bend + (CHANNEL_H/2) +SPACING
301 end
302 elseif quadrant ==4 then
303     if direction == "CCW" then
304         for k=1,LANES,1 do
305             for j=elements[k],0,-1 do
306                 x = startx - math.cos(elementAngle[k]*-j)*radius[k] - (CHANNEL_H/2)
307                 y = starty - math.sin(elementAngle[k]*-j)*radius[k] -radius_bend
308                 setlayer(1)
309                 box(x,y,CHANNEL_W, CHANNEL_H,(90 / elements[k])*-j)
310                 setlayer(2)
311                 circle(x,y, ETCH_WIDTH/2)
312             end
313         end
314
315         endx = startx - math.cos(0)*radius_bend - (CHANNEL_H /2)
316         endy = starty - math.sin(0)*radius_bend - radius_bend -SPACING - (CHANNEL_H /2)
317     else
318         for k=1,LANES,1 do
319             for j=0,elements[k],1 do
320                 x = startx - math.cos(elementAngle[k]*-j)*radius[k] + radius_bend
321                 y = starty - math.sin(elementAngle[k]*-j)*radius[k] + (CHANNEL_H/2)
322                 setlayer(1)
323                 box(x,y,CHANNEL_W, CHANNEL_H,(90 / elements[k])*-j)
324                 setlayer(2)
325                 circle(x,y,ETCH_WIDTH/2)
326             end
327         end
328         endx = startx - math.cos(-math.pi/2)*radius_bend + radius_bend + (CHANNEL_H/2) +SPACING
329         endy = starty - math.sin(-math.pi/2)*radius_bend + (CHANNEL_H/2)
330     end
331 end
332 return endx, endy
333 end

```

---

Listing B.3: multi-serpentine.lua

```

1  — multi serpentine
2
3  if 2*BEND_RADIUS >= CHANNEL_SPACING then
4      spacer = 0
5  else
6      spacer = CHANNEL_SPACING - (2*BEND_RADIUS)
7  end
8
9  j=1
10 endx = 0
11 endy = 0
12
13 start = true
14 for i=1,SERPENTINE,1 do
15     if start then
16         endx, endy = straight_multi(-(CHANNEL_SPACING+2*BEND_RADIUS) / 2, -1200,800,90)
17         endx, endy = arc_multi(endx,endy,4,"CW",BEND_RADIUS)
18         endx, endy = straight_multi(endx,endy,150,0) —top
19         endx, endy = arc_multi(endx,endy,1,"CW",BEND_RADIUS)
20         endx, endy = straight_multi(endx,endy,spacer+((i-1)*CHANNEL_SPACING)+START_LENGTH,270)
21         endx, endy = arc_multi(endx,endy,3,"CCW",BEND_RADIUS)
22         NO_PATTERN = true
23         endx, endy = straight_multi(endx,endy,spacer,0) —bottom
24         NO_PATTERN = false
25         endx, endy = arc_multi(endx,endy,2,"CCW",BEND_RADIUS)
26
27
28     start = false
29 else
30
31     if j == 1 then
32         endx, endy = straight_multi(endx,endy,spacer+((i-1)*CHANNEL_SPACING)+START_LENGTH,90)
33         endx, endy = arc_multi(endx,endy,4,"CW",BEND_RADIUS)
34         endx, endy = straight_multi(endx,endy,spacer+(((2*i)-1)*CHANNEL_SPACING),0) —top

```

---

```

35     endx, endy = arc_multi(endx, endy, 1, "CW", BEND_RADIUS)
36     endx, endy = straight_multi(endx, endy, spacer + ((i - 1) * CHANNEL_SPACING) + START_LENGTH, 270)
37     endx, endy = arc_multi(endx, endy, 3, "CCW", BEND_RADIUS)
38     NO_PATTERN = true
39     endx, endy = straight_multi(endx, endy, spacer, 0)    ---bottom
40     NO_PATTERN = false
41     endx, endy = arc_multi(endx, endy, 2, "CCW", BEND_RADIUS)
42     else
43         endx, endy = straight_multi(endx, endy, spacer + ((i - 1) * CHANNEL_SPACING) + START_LENGTH, 90)
44         endx, endy = arc_multi(endx, endy, 1, "CCW", BEND_RADIUS)
45         endx, endy = straight_multi(endx, endy, spacer + (((2 * i) - 1) * CHANNEL_SPACING), 180)    ---top
46         endx, endy = arc_multi(endx, endy, 4, "CCW", BEND_RADIUS)
47         endx, endy = straight_multi(endx, endy, spacer + ((i - 1) * CHANNEL_SPACING) + START_LENGTH, 270)
48         endx, endy = arc_multi(endx, endy, 2, "CW", BEND_RADIUS)
49         NO_PATTERN = true
50         endx, endy = straight_multi(endx, endy, spacer, 180)    ---bottom
51         NO_PATTERN = false
52         endx, endy = arc_multi(endx, endy, 3, "CW", BEND_RADIUS)
53     end
54     end
55     j = -j
56     endk = i
57 end
58
59
60 if j == 1 then
61     endx, endy = straight_multi(endx, endy, spacer + (endk * CHANNEL_SPACING) + START_LENGTH, 90)
62     endx, endy = arc_multi(endx, endy, 4, "CW", BEND_RADIUS)
63     endx, endy = straight_multi(endx, endy, -(CHANNEL_SPACING + BEND_RADIUS) / 2, -endx, 0)
64     endx, endy = arc_multi(endx, endy, 2, "CCW", BEND_RADIUS)
65     endx, endy = straight_multi(endx, endy, 168, 90)
66 else
67     endx, endy = straight_multi(endx, endy, spacer + (endk * CHANNEL_SPACING) + START_LENGTH, 90)
68     endx, endy = arc_multi(endx, endy, 1, "CCW", BEND_RADIUS)
69     endx, endy = straight_multi(endx, endy, endx - (CHANNEL_SPACING + BEND_RADIUS) / 2, 180)
70     endx, endy = arc_multi(endx, endy, 3, "CW", BEND_RADIUS)
71 end
72
73 ---setlayer(13)
74 ---text(TOTAL_LENGTH, {-2500, 2200})

```

---



# Appendix C

## Processing

### C.1 Process flow

Step	Process	Comment
<b>Access-holes fabrication</b>		
1	<b>Substrate Silicon &lt;100&gt; DSP(#subs119)</b> NL-CLR-Not standard available Test wafers for stress measurement LPCVD Orientation: <100> Diameter: 100mm Thickness: 385µm Polished: double side polished Resistivity: 1-10 Type: N	380 um thick N-type, chosen for the thickness and not for the doping
2	<b>Measurement of wafer thickness (#metro112)</b> NL-CLR-HeidenHahn	Needed for determination of the etching times for the DRIE etch.
3	<b>Clean HNO3-1 (#clean102)</b> NL-CLR-WB14 beaker 1: HNO <sub>3</sub> (99%) 5min	Do standard cleaning
4	<b>Clean HNO3-2 (#clean138)</b> NL-CLR-WB14 beaker 2 : HNO <sub>3</sub> (99%) 5min	
5	<b>Quick Dump Rinse (QDR)(#clean119)</b> NL-CLR-Wetbenches Rinse till the DI resistivity is > 10.5ΩM	
6	<b>Clean HNO3-3a/b (#clean 118)</b> NL-CR-WB14 beaker 3a/b: HNO <sub>3</sub> (69%), temp 95°C, time > 10min	
7	<b>Quick Dump Rinse (QDR) (#clean119)</b> NL-CLR-Wetbenches Rinse till the DI resistivity is > 10.5ΩM	
8	<b>Etching in HF 1% (metal free) (#etch127)</b> NL-CLR-WB15 use beaker HF 1% time variable native oxide strip: > 1 min or hydrofobic surface  etchrate: TEOS <b>H3 (new)</b> = 28 nm/min Si3N4 <b>H2 (new)</b> = 0.33 nm/min	1% HF dip to remove oxide for nitride layer
9	<b>Quick Dump Rinse (QDR) (#clean119)</b> NL-CLR-Wetbenches Rinse till the DI resistivity is > 10.5ΩM	
10	<b>Substrate drying (#clean120)</b> NL-CLR-WB Single wafer dryer speed: 2500 rpm, 60 sec with 30 sec N <sub>2</sub> flow	
11	<b>LPCVD of SiRN (50-100 Mpa) (#film102)</b> NL-CLR-LPCVD G3 Program: SiRN01 SiH <sub>2</sub> Cl <sub>2</sub> flow: 77,5 sccm NH <sub>3</sub> flow: 20 sccm temperature: 820/850/870°C pressure: 150 mTorr N <sub>2</sub> low: 250 sccm <b>deposition rate: ± 4 nm/min</b> N <sub>f</sub> : ± 2.18	Layer thickness: 500 nm -> 125min (MEMS2009 128min)
12	<b>Ellipsometer measurement (#metro107)</b> NL-CLR-Plasmos Ellipsometer	Measure SiRN film thickness
13	<b>Inspection by optical microscope (#metro101)</b> NL-CLR-Nikon Microscope dedicated microscope for lithography inspection	Check also with floodlight for particle deposition
14	<b>Dehydration bake SU-8 (#lith162)</b> NL-CLR-WB24 Dehydration bake Hotplate: temp 120°C, 10min	Processing on backside of the wafer

15	<b>Coating SU-8 2005 (#lith176)</b> NL-CLR-WB24 SüssMicroTec Spinner Delta 20 Microchem NANO SU-8 2005 TST Bottle Experimental Results: Spin program rpm Thickness ( $\mu\text{m}$ ) 1 1000 13.6 2 1500 8.4 3 2000 7.4 4 2500 6.0 5 3000 5.2 6 3500 4.6 7 4000 4.1	Program 5
16	<b>Softbake SU-8 2005 (#lith177)</b> NL-CLR-WB24 Hotplate 1 min @ 65 °C ramp up to 95°C 2 min @ 95 °C cooldown on hotplate to 25°C	
17	<b>Alignment &amp; Exposure SU-8 2005(#lith178)</b> NL-CLR-EVG 620 Electronic Vision Group 620 Mask Aligner Exposure time 10sec Hardcontact	Mask: Back access-holes
18	<b>Post Exposure Bake SU-8 2005(#lith179)</b> NL-CLR-WB24 Hotplate apply immediatly after exposure! Start @ 65 °C Ramp to 95 °C Cooldown to 25°C and leave the wafer on the hotplate Total process time ca. 90 min	
19	<b>Development SU-8 2005 (#lith175)</b> NL-CLR-WB24TCO Spray Developer Developer: PGMEA (RER600, ARCH Chemicals) Spray develop 5 cycles x 30sec Rinse with RER600 Rinse with IPA Spin dry Check result and perform extra cycles if not complete Check Micro-Chem site for more process information <a href="http://www.microchem.com/products/su_eight.htm">http://www.microchem.com/products/su_eight.htm</a>	Rinse 5 seconds with the RER600 and IPA bottle
20	<b>Hard bake SU-8 (#lith168)</b> NL-CLR-WB24 Hotplate 2hr @ 120 °C	
21	<b>Inspection by optical microscope (#metro101)</b> NL-CLR-Nikon Microscope dedicated microscope for lithography inspection	
22	<b>Surface profile measurement (#metro105)</b> NL-CLR-Veeco Dektak 8	Dummy 1. Check SU-8 thickness, > 5 $\mu\text{m}$
23	<b>DRIE of multilayers (#etch174)</b> NL-CLR-Adixen SE Application: directional etch of SiRN or SiO <sub>2</sub> Nickname: "Roberts:" process <b>Parameters Value</b> Argon (sccm) 100 CHF <sub>3</sub> (sccm) 100 APC % 100 ICP (Watt) 1200 CCP (Watt) Rf 150 (Vde=580V) SH (mm) 200 Electrode temp. -100 +20 °C He (bar) 10 Etch rate Oir resist 160 nm/min v Etch rate SiO <sub>2</sub> 250 nm/min Etch rate silicon 70-80 nm/min Etch rate SU-8 150 nm/min Etchrate SiRN 300 nm/min	Thickness step 12. ~500nm -> 300nm/min +10% = 110 sec, took 130 seconds
24	<b>Plasma etching of Si A-pulsed-CHF<sub>3</sub> (#etch169)</b> NL-CLR-Adixen SE Application: Silicon pillars/Si high load/ trenches, wafer through Starting recipe <b>Parameters Etch Deposition(pulsed) Gas</b> SF <sub>6</sub> CHF <sub>3</sub> Flow (sccm) 400 200 Time (sec) 4 0.5 Priority 2 1 APC % 15 15 ICP (Watt) 2500 2500 CCP (Watt) nvt 20 Pulsed (msec) nvt 20on/180off SH (mm) 110 110 Electrode temp. -120 ... -100 -120 ... -100 He (bar) 10 10 Olin 907-17, 120°C, 60 min postbake 15 nm/min	Test with dummy 1-3. Etch through the wafer till nitride layer: 385um Recipe: Pulsed CHF <sub>3</sub> - Goan Time: 34 minutes
25	<b>Inspection by optical microscopic (#metro102)</b> NL-CLR- 6 microscopes olympus Microscope (4) leica Microscope (2)	Use dummy 1. Check profile, check wafer through etch



26	<b>Stripping resist/cleaning in piranha private use (#lith195)</b> NL-CLR-WB09 Application: stripping of resist and cleaning of substrates Mixture: H <sub>2</sub> SO <sub>4</sub> :H <sub>2</sub> O <sub>2</sub> (3:1) vol% add H <sub>2</sub> O <sub>2</sub> slowly! to H <sub>2</sub> SO <sub>4</sub> exothermic process!! due to mixing the temperature will increase to .....130°C adjust the hotplate at 85 °C, temperature: 130°C time: depends in application ( 10- 30min)	Apply 100% strip of SU-8 layer, time depends on thickness 15 min. Be carefull for the excessive development of gas. For thick SU-8 layers clean only one wafer/solution !
27	<b>Quick Dump Rinse (QDR)(#clean119)</b> NL-CLR-Wetbenches Rinse till the DI resistivity is > 10.5ΩM	standard cleaning
28	<b>Substrate drying (#clean120)</b> NL-CLR-WB Single wafer dryer speed: 2500 rpm, 60 sec with 30 sec N <sub>2</sub> flow	
29	<b>Clean HNO<sub>3</sub>-1 (#clean102)</b> NL-CLR-WB14 beaker 1: HNO <sub>3</sub> (99%) 5min	
30	<b>Clean HNO<sub>3</sub>-2 (#clean138)</b> NL-CLR-WB14 beaker 2 : HNO <sub>3</sub> (99%) 5min	
31	<b>Quick Dump Rinse (QDR)(#clean119)</b> NL-CLR-Wetbenches Rinse till the DI resistivity is > 10.5ΩM	
32	<b>Clean HNO<sub>3</sub>-3a/b(#clean 118)</b> NL-CR-WB14 beaker 3a/b: HNO <sub>3</sub> (69%), temp 95°C, time > 10min	
33	<b>Quick Dump Rinse (QDR)(#clean119)</b> NL-CLR-Wet benches Rinse till the DI resistivity is > 10.5ΩM	
34	<b>Substrate drying (#clean120)</b> NL-CLR-WB Single wafer dryer speed: 2500 rpm, 60 sec with 30 sec N <sub>2</sub> flow	
35	<b>Substrate rinsing/drying Semitool (#clean121)</b> NL-CLR-Wet Benches Semitool spin rinser dryer Use dedicated wafer carrier of rinser dryer	
36	<b>Dry Oxidation of silicon at 800°C (#film126)</b> NL-CLR-Furnace B3 Standby temperature: 800°C Program: DOX-800 Temp.: 800°C Gas: O <sub>2</sub> Flow: 2 l/min	Removal of FC film for the Bosch etching. Time 30 min
37	<b>Etching in HF 1% (metal free)(#etch127)</b> NL-CLR-WB15 use beaker HF 1% time variable native oxide strip: > 1 min or hydrofobic surface etchrate: TEOS H3 (new) = 28 nm/minSi <sub>3</sub> N <sub>4</sub> H2 (new) = 0.33 nm/min	Removal of oxide and FC residue. Time 10 min.
38	<b>Quick Dump Rinse (QDR)(#clean119)</b> NL-CLR-Wetbenches Rinse till the DI resistivity is > 10.5ΩM	
39	<b>Substrate drying (#clean120)</b> NL-CLR-WB Single wafer dryer speed: 2500 rpm, 60 sec with 30 sec N <sub>2</sub> flow	
40	<b>Clean HNO<sub>3</sub>-1 (#clean102)</b> NL-CLR-WB14 beaker 1: HNO <sub>3</sub> (99%) 5min	Standard cleaning
41	<b>Clean HNO<sub>3</sub>-2 (#clean138)</b> NL-CLR-WB14 beaker 2 : HNO <sub>3</sub> (99%) 5min	
42	<b>Quick Dump Rinse (QDR)(#clean119)</b> NL-CLR-Wetbenches Rinse till the DI resistivity is > 10.5ΩM	
43	<b>Clean HNO<sub>3</sub>-3a/b(#clean 118)</b> NL-CR-WB14 beaker 3a/b: HNO <sub>3</sub> (69%), temp 95°C, time > 10min	
44	<b>Quick Dump Rinse (QDR)(#clean119)</b> NL-CLR-Wetbenches Rinse till the DI resistivity is > 10.5ΩM	
45	<b>Substrate drying (#clean120)</b> NL-CLR-WB Single wafer dryer speed: 2500 rpm, 60 sec with 30 sec N <sub>2</sub> flow	
46	<b>Substrate rinsing/drying Semitool (#clean121)</b> NL-CLR-WetBenches Semitool spin rinser dryer	
47	<b>LPCVD of SiO<sub>2</sub> (TEOS)(#film158)</b> NL-CLR-LPCVD H3 Program: N2 TEOS flow: 40 sccm Bubbler N2 : 30 sccm temperature: 710 °C (Z1), 725°C (Z2), 740°C (Z3) pressure: 400 mTorr Stress: 282 ± 13 MPa (after anneal @1150°C, 3hr) deposition rate: 8.1 nm/min (1100 nm) wafer non-uniformity: 3.6 % boat non-uniformity: 1.0 % N <sub>f</sub> : 1.434	grow 1100nm. 3 wafer spacing gives 1050 nm in 112 min (Christian Brunnink)
48	<b>Ellipsometer measurement(#metro107)</b> NL-CLR-Plasmos Ellipsometer	Dummy 2. Measure TEOS layer on the frontside for the etch

49	<b>UV dicing foil (Adwill D-210)(#back104)</b> NL-CLR- Dicing foil Information: Thickness: 125um Material: 100um PET + 25um Acrylic (adhesive) Adhesion before UV: 2000 mN/25mm Adhesion after UV : 15 mN/25mm UV irradiation : Luminance > 120mW/cm <sup>2</sup> and Quality > 70mj/cm <sup>2</sup> (wave length: 365nm)	Apply dicing foil on the backside of the wafer with roller
50	<b>Etching in BHF (1:7) metal free(#etch124)</b> NL-CLR-WB15 Use dedicated beaker BHF (1:7) temp.: 20°C. Etchrates: Thermal SiO <sub>2</sub> :60-80nm/min PECVD SiO <sub>2</sub> :125/nm/min TEOS-old SiO <sub>2</sub> :180/nm/min TEOS H3 (new):242 nm/min Si <sub>3</sub> N <sub>4</sub> -H2: 0,64 nm/min	Test with dummy 2. Remove TEOS on frontside. Etch speed 242 nm/min, layer thickness 1050nm (step 48) -> 260 sec +10% overetch = 286 sec
51	<b>Quick Dump Rinse (QDR)(#clean119)</b> NL-CLR-Wetbenches Rinse till the DI resistivity is > 10.5ΩM	
52	<b>Substrate drying (#clean120)</b> NL-CLR-WB Single wafer dryer speed: 2500 rpm, 60 sec with 30 sec N <sub>2</sub> flow	
53	Removal dicing foil	
54	<b>Inspection by optical microscopic (#metro102)</b> NL-CLR- 6 microscopes olympus Microscope (4) leica Microscope (2)	
55	<b>Clean HNO<sub>3</sub>-1 (#clean102)</b> NL-CLR-WB14 beaker 1: HNO <sub>3</sub> (99%) 5min	Standard cleaning
56	<b>Clean HNO<sub>3</sub>-2 (#clean138)</b> NL-CLR-WB14 beaker 2 : HNO <sub>3</sub> (99%) 5min	
57	<b>Quick Dump Rinse (QDR)(#clean119)</b> NL-CLR-Wetbenches Rinse till the DI resistivity is > 10.5ΩM	
58	<b>Clean HNO<sub>3</sub>-3a/b(#clean 118)</b> NL-CLR-WB14 beaker 3a/b: HNO <sub>3</sub> (69%), temp 95°C, time > 10min	
59	<b>Quick Dump Rinse (QDR)(#clean119)</b> NL-CLR-Wet benches Rinse till the DI resistivity is > 10.5ΩM	
60	<b>Substrate drying (#clean120)</b> NL-CLR-WB Single wafer dryer speed: 2500 rpm, 60 sec with 30 sec N <sub>2</sub> flow	
61	<b>Substrate rinsing/drying Semitool (#clean121)</b> NL-CLR-Wet Benches Semitool spin rinser dryer	
<b>Channel fabrication</b>		
62	<b>Sputtering of Cr (#film117)</b> NL-CLR-Sputterke Eq.Nr. 37 Cr Target (gun #: see mis logbook) Use Ar flow to adjust process pressure. Base pressure: < 1.0 e-6mbar Sputter pressure: 6.6 e-3mbar power: 200W Depositionrate = 15 nm/min	50 nm layer on frontside, deposition rate 15 nm/min -> 200 sec
63	<b>Dehydration bake(#lith102)</b> NL-CLR-WB21/22 dehydration bake at hotplate temp. 120°C time: 5min	Bake: 5 min. Continue immediatly with priming the step!
64	<b>Priming (liquid)(#lith101)</b> NL-CLR-WB21/22 Primer: HexaMethylDiSilazane (HMDS) use spincoater: program: 4000 (4000rpm, 30sec)	
65	<b>Coating Olin Oir 907-17 (#lith105)</b> NL-CLR-WB21 Coating: Primus spinner olin oir 907-17 spin Program: 4000 (4000rpm, 30sec) Prebake: hotplate time 90 sec temp 95 °C	
66	<b>Alignment &amp; Exposure Olin Oir 907-17(#lith121)</b> NL-CLR-EV620 Electronic Vision Group EV620 Mask Aligner Hg-lamp: 12 mW/cm <sup>2</sup> Exposure Time: 4sec	Mask: Channel -> Exposure time 3.5 sec Use vacuum contact for proper definition of 1.5 um line segments
67	<b>Development Olin Oir resist(#lith111)</b> NL-CLR-WB21 After exposure Bake : hotplate time 60sec temp 120°C development: developer: OPD4262 time: 30sec in beaker 1 time: 15-30sec in beaker 2	No hard-bake as it increases the size of the slits!
68	<b>Quick Dump Rinse (QDR)(#clean119)</b> NL-CLR-Wetbenches Rinse till the DI resistivity is > 10.5ΩM	
69	<b>Substrate drying (#clean120)</b> NL-CLR-WB Single wafer dryer speed: 2500 rpm, 60 sec with 30 sec N <sub>2</sub> flow	

71	<b>Inspection by optical microscope (#metro101)</b> NL-CLR-Nikon Microscope dedicated microscope for lithography inspection	Check width of the channel slits on all wafers =< 2.1 um
72	<b>Cleaning by UV/Ozone (#clean109)</b> NL-CLR-UV PR5 100 reactor To improve wetting for wet chemical etching of chromium and oxide layers coated with olin oir resist. Time: 300 sec	to improve wetting of chromium
73	<b>Etching of chromium(#etch134)</b> NL-CLR-WB6 Use dedicated beaker with chromium etch (standard) temp.:20°C Etchrates = 60nm/min,Check always the etchrate with dummy wafer!	Use dummy 2 for etch test. Prewet 60 seconds in DI, 40 sec etch time
74	<b>Quick Dump Rinse (QDR)(#clean119)</b> NL-CLR-Wetbenches Rinse till the DI resistivity is > 10.5ΩM	
75	<b>Substrate drying (#clean120)</b> NL-CLR-WB Single wafer dryer speed: 2500 rpm, 60 sec with 30 sec N <sub>2</sub> flow	
76	<b>Inspection by optical microscopic (#metro102)</b> NL-CLR- 6 microscopes olympus Microscope (4) leica Microscope (2)	Check slit width of the chromium =< 2.1 um
77	<b>DRIE of multilayers (#etch174)</b> NL-CLR-Adixen SE Application: directional etch of SiRN or SiO <sub>2</sub> Nickname: "Roberts:" process <b>Parameters Value</b> Argon (sccm) 100 CHF <sub>3</sub> (sccm) 100 APC % 100 ICP (Watt) 1200 CCP (Watt) Rf 150 (Vde=580V) SH (mm) 200 Electrode temp. -100 +20 °C He (bar) 10 Etch rate Oir resist 160 nm/min Etch rate SiO <sub>2</sub> 250 nm/min Etch rate silicon 70-80 nm/min Etch rate SU-8 150 nm/min Etchrate SiRN 300 nm/min	SiRN is measured in step 12. ~500nm SiRN: 300nm/min -> 100 sec + 10% = 110 sec
78	<b>Inspection by optical microscopic (#metro102)</b> NL-CLR- 6 microscopes olympus Microscope (4) leica Microscope (2)	Can be skipped if the previous and next step are done in 1 run.
79	<b>DRIE of silicon for semi-isotropic channels (SCT) (#etch163)</b> NL-CLR-Adixen AMS 100 SE Applications: semi-isotropic channels (SCT) Pre-etch step: same values, incl. CCP of 30 Watt, time 30 sec. <b>Parameters Value</b> SF <sub>6</sub> [sccm] 400 He-backside cooling [mbar] 10 ICP [watt] 2500 CCP On/Off [msec] 0 p [Pa] 10 APC position % 100 Electrode temperature [°C] 20 Substrate height [mm] 110 Etch rate SiO <sub>2</sub> [μm/min] Etch rate Olin 907 [μm/min] 0.250 Etch rate -Silicon (μm/min) 1.2 μm/min (for 2μm slits-SCT) Etch rate SiRN [nm/min] 25	Use dummy 2 and 3. Apply pre etch step incl. CCP of 30 Watt (time 30 sec) Depth: 30 um Width: 40 um P = 10 Pa APC position = 100% Etch rate silicon 1.2 um/min for 2 um slits Time 25-30 min
80	<b>Stripping of resist in oxygen plasma (#lith117)</b> NL-CLR- Tepla 300E Barrel Etcher (2.45 GHz) Multipurpose sytem O <sub>2</sub> flow: 200sccm (50%) Power: 500W Pressure: 1.2 mbar Values for olin oir resist: Time: 10 min for 1-3 wafers, 400 nm/min Time: 20 min for 4-10 wafers End point detection by visual inspection of the plasma color. Blue color means still photoresist on the wafer, purple means clean.	Complete stripping will oxidize the chromium. 5 minutes for photoresist and remove the rest with HNO <sub>3</sub> .
81	<b>Etching of chromium(#etch134)</b> NL-CLR-WB6 Use dedicated beaker with chromium etch (standard) temp.:20°C Etchrates = 60nm/min,Check always the etchrate with dummy wafer!	Wet the Cr layer in DI for 5 min and strip in Cr etchant for 10-30 min
82	<b>Quick Dump Rinse (QDR)(#clean119)</b> NL-CLR-Wetbenches Rinse till the DI resistivity is > 10.5ΩM	
83	<b>Substrate drying (#clean120)</b> NL-CLR-WB Single wafer dryer speed: 2500 rpm, 60 sec with 30 sec N <sub>2</sub> flow	
84	<b>Inspection by optical microscopic (#metro102)</b> NL-CLR- 6 microscopes olympus Microscope (4) leica Microscope (2)	Check Cr residue close to slit windows

85	<b>Etching in BHF (1:7) multipurpose(#etch191)</b> NL-CLR-WB6 use dedicated beaker BHF (1:7) quick Dump Rinse > 10.5 ΩM spin drying Etch rates: Thermal SiO <sub>2</sub> : 60-80 nm/min PECVD SiO <sub>2</sub> : 125 nm/min TEOS-old SiO <sub>2</sub> : 180 nm/min TEOS H3 (new): 242 nm/min Si <sub>3</sub> N <sub>4</sub> -H <sub>2</sub> : 0.64 nm/min	Open TEOS backside Etch rate 242 nm/min -> 260 sec + 10% = 286 sec
86	<b>Quick Dump Rinse (QDR)(#clean119)</b> NL-CLR-Wetbenches Rinse till the DI resistivity is > 10.5 ΩM	
87	<b>Substrate drying (#clean120)</b> NL-CLR-WB5 single wafer dryer speed: 2500 rpm, 60 sec with 30 sec N <sub>2</sub> flow	
88	<b>Inspection by optical microscope (#metro102)</b> NL-CLR- 6 microscopes olympus Microscope (4) leica Microscope (2)	Measure width of slits and calculate thickness for all wafer => time of SINR deposition Calculation: ((Slit width/2)/deposition speed) +20% = deposition time
89	<b>Clean HNO<sub>3</sub>-1 (#clean102)</b> NL-CLR-WB14 beaker 1: HNO <sub>3</sub> (99%) 5min	
90	<b>Clean HNO<sub>3</sub>-2 (#clean138)</b> NL-CLR-WB14 beaker 2: HNO <sub>3</sub> (99%) 5min	
91	<b>Quick Dump Rinse (QDR)(#clean119)</b> NL-CLR-Wetbenches Rinse till the DI resistivity is > 10.5 ΩM	
92	<b>Clean HNO<sub>3</sub>-3a/b(#clean 118)</b> NL-CLR-WB14 beaker 3a/b: HNO <sub>3</sub> (69%), temp 95°C, time > 10min	
93	<b>Quick Dump Rinse (QDR)(#clean119)</b> NL-CLR-Wetbenches Rinse till the DI resistivity is > 10.5 ΩM	
94	<b>Substrate drying (#clean120)</b> NL-CLR-WB Single wafer dryer speed: 2500 rpm, 60 sec with 30 sec N <sub>2</sub> flow	
95	<b>Substrate rinsing/drying Semitool (#clean121)</b> NL-CLR-WetBenches Semitool spin rinser dryer	
96	<b>Litho furnace(#new)</b> NL-CLR- Temperature 85°C, time 16 hours (over night, use sign with Process running)	Use furnace for drying and evaporation of the water out of the channels. Procedure: start at 25 degrees with target temperature of 85 degrees. During the ramp up the fluid will evaporate. 16 hours
97	<b>LPCVD of SiRN (50-100 Mpa)(#film102)</b> NL-CLR-LPCVD G3 Program: SiRN01 SiH <sub>2</sub> Cl <sub>2</sub> flow: 77,5 sccm NH <sub>3</sub> flow: 20 sccm temperature: 820/850/870°C pressure: 150 mTorr N <sub>2</sub> low: 250 sccm <b>deposition rate: ± 4 nm/min</b> N <sub>f</sub> : ± 2.18	For time see step 88 Unload boat/wafer with slow speed. goal = 1696 nm = 377 min, measured 1808nm
98	<b>Inspection by optical microscope (#metro101)</b> NL-CLR- Nikon Microscope dedicated microscope for lithography inspection	Dummy 3, check channel closure. Druplet test?
99	<b>Ellipsometer measurement(#metro107)</b> NL-CLR-Plasmos Ellipsometer	Dummy 3, measure SiRN thickness

Step	Process	Comment
<b>Core fabrication</b>		
1	<b>Dupont MX 5020 foil for litho (#NEW)</b> NL-CLR- Material: Dupont MX5020 foil Application: Structure coverage on wafer for dry etch protection Procedure: Cut foil to size remove plastic protection (has no color) from backside of the foil with scotch tape corners on both sides Apply the foil to the wafer with a roller, put a little tension on the foil so it is flat on the roller. Avoid air bubbles by applying with pressure on the roller (watch out! can break thin structures on the wafer). If large bubbles or lines are visible remove foil and use a new piece. Protect the foil by folding wafer in a sheet of cleanroom paper during laminating. Laminator: Temp 90°C, speed 2 Cut with knife the foil away around the wafer Pre-bake Hotplate: 95°C, 45 sec Litho on EV620, 8 seconds (soft-contact) Post-bake Hotplate: 95°C, 45 sec Remove protective foil Hotplate: 120°C, 45 sec for good adhesion Develop in NaCO <sub>3</sub> 10 g/L @ 32°C with stirrer QDR spin drying Hard-bake Hotplate: 120°C, 45 sec	MX5020 litho flow. Mask: back KOH

2.1	<b>DRIE of multilayers (#etch174)</b> NL-CLR-Adixen SE Application: directional etch of SiRN or SiO2 Nickname: "Roberts:" process <b>Parameters Value</b> Argon (sccm) 100 CHF3 (sccm) 100 APC % 100 ICP (Watt) 1200 CCP (Watt) Rf 150 (Vde=580V) SH (mm) 200 Electrode temp. -100 +20 °C He (bar) 10 Etch rate Oir resist 160 nm/min Etch rate SiO2 250 nm/min Etch rate silicon 70-80 nm/min Etch rate SU-8 150 nm/min Etchrate SiRN 300 nm/min	~2200nm SiRN: 300nm/min -> 440 sec. If the Adixen is not available step 2.2 and 2.3 can be used, otherwise these can be skipped.
2.2	<b>DRIE of SiRN (#NEW)</b> (NL-CLR-Oxford Plasmalab 100 ICP) Parameters of start recipe Temp: 20°C ICP: 600 Watt SF6: 25 sccm Pressure: 10 mTorr He pressure: 10mbar CCP: 150 watt , adjust scale from 30 to 300 Watt by turning the key XTerm: 200 VDC (Act 338 0 82 1920)	Time: 11 minutes (etching non-uniform across wafer: centre clean, at rim still 150nm).
2.3	<b>RIE CHF3/O2 (Tetske)(#etch193)</b> (NL-CLR-Tetske) Chamber: dirty chamber ! Do Not use the Quartz electrode !! Electrode: styros Temp: 20°C Power: 60 Watt CHF3: 25 sccm O2: 5sccm Pressure: 10 mTorr DC Bias: 489 VDC Time: 8 minutes (cleaning up the non-uniform etch)	
3(replaced by 2)	<b>DRIE of multilayers (#etch174)</b> NL-CLR-Adixen SE Application: directional etch of SiRN or SiO2 Nickname: "Roberts:" process <b>Parameters Value</b> Argon (sccm) 100 CHF3 (sccm) 100 APC % 100 ICP (Watt) 1200 CCP (Watt) Rf 150 (Vde=580V) SH (mm) 200 Electrode temp. -100 +20 °C He (bar) 10 Etch rate Oir resist 160 nm/min v Etch rate SiO2 250 nm/min Etch rate silicon 70-80 nm/min Etch rate SU-8 150 nm/min Etchrate SiRN 300 nm/min	Etch time dependent on layer thickness measured in step 99 of the Wobbe flow.
4	<b>Stripping resist/cleaning in piranha private use (#lith195)</b> NL-CLR-WB09 Application: stripping of polymer resist and cleaning of substrates Mixture: H2SO4:H2O2 (3:1) vol% add H2O2 slowly! to H2SO4 exothermic process!! due to mixing the temperature will increase to .....130°C adjust the hotplate at 85 °C, temperature: 130°C time: 10	MX5020 removal flow, polymer will release in 30 seconds and converts into a brown foam on top of the Piranha
5	<b>Etching in 1% HF multipurpose(#etch192)</b> NL-CLR-WB16 multipurposeuse dedicated beaker HF 1% temp.: 20 °C. time: depends on application	Removal native oxide
6	<b>Quick Dump Rinse (QDR)(#clean119)</b> NL-CLR-Wetbenches Rinse till the DI resistivity is > 10.5ΩM	
7	<b>Etching in KOH standard(#etch138)</b> NL-CLR-WB17 use dedicated beaker 1 or 2 25wt% KOH (standard recipe) temp.: 75°C use stirrer Etchrates:Si <100> = 1iEj m/min Si <111> = 12.5nm/min SiO2 (thermal) = 180nm/hrSiRN < 0.6nm/hr	280 um -> 280min

8	<b>Clean: rinsing in beaker(#clean128)</b> NL-CLR-Wetbench 9/10/17 Beaker 1 with DI: 5min Beaker 2 with DI: 5min refresh beaker 1,2, repeat several times	
9	<b>Quick Dump Rinse (QDR)(#clean119)</b> NL-CLR-Wetbenches Rinse till the DI resistivity is > 10.5ΩM	
10	<b>Cleaning RCA 2 megasonic (#clean116)</b> NL-CLR-WB-18 Mixture: HCL:H <sub>2</sub> O <sub>2</sub> :H <sub>2</sub> O (1:1:20) vol% Start fill; bath is filled with H <sub>2</sub> O and HCL, and heated When temp. is 55°C add the H <sub>2</sub> O <sub>2</sub> by pressing [Continue] set point max 55°C. time 15min	Workbench was not available, used WB09 for private use RCA-2.
11	<b>Quick Dump Rinse (QDR)(#clean119)</b> NL-CLR-Wetbenches Rinse till the DI resistivity is > 10.5ΩM	
12	<b>Substrate drying (#clean120)</b> NL-CLR-WB Single wafer dryer speed: 2500 rpm, 60 sec with 30 sec N <sub>2</sub> flow	
13	<b>Substrate rinsing/drying Semitool (#clean121)</b> NL-CLR-WetBenches Semitool spin rinser dryer	
14	<b>Inspection by optical microscopic (#metro102)</b> NL-CLR- 6 microscopes olympus Microscope (4) leica Microscope (2)	Use dummy 1. Check profile, check wafer through etch
15	<b>Surface profile measurement(#metro105)</b> NL-CLR-Veeco Dektak 8	Dummy 3. Verify the etched depth
16	<b>Litho furnace(#new)</b> NL-CLR- Temperature 85°C, time 16 hours (over night, use sign with Process running)	Use furnace for drying and evaporation of the water out of the channels. Procedure: start at 25 degrees with target temperature of 85 degrees. During the ramp up the fluid will evaporate. 16 hours
17	<b>LPCVD of SiO<sub>2</sub> (TEOS)(#film158)</b> NL-CLR-LPCVD H3 Program: N2 TEOS flow: 40 sccm Bubbler N2 : 30 sccm temperature: 710 °C (Z1), 725°C (Z2), 740°C (Z3) pressure: 400 mTorr Stress: 282 ± 13 MPa (after anneal @1150°C, 3hr) deposition rate: 8.1 nm/min (1100 nm) wafer non-uniformity: 3.6 % boat non-uniformity: 1.0 % N <sub>f</sub> : 1.434	grow 1100nm. 3 wafer spacing -> 112 min (Christian Brunink)
<b>Heater fabrication</b>		
18	<b>UV dicing foil (Adwill D-210)(#back104)</b> NL-CLR- Dicing foil Information: Thickness: 125um Material: 100um PET + 25um Acrylic (adhesive) Adhesion before UV: 2000 mN/25mm Adhesion after UV : 15 mN/25mm UV irradiation : Luminance > 120mW/cm <sup>2</sup> and Quality > 70mJ/cm <sup>2</sup> (wave length: 365nm)	Apply dicing foil on the backside of the wafer with roller
19	<b>Etching in BHF (1:7) multipurpose(#etch191)</b> NL-CLR-WB6 use dedicated beaker BHF (1:7) quick Dump Rinse >10.5 ΩM spin drying Etch rates: Thermal SiO <sub>2</sub> :60-80nm/min PECVD SiO <sub>2</sub> :125/nm/min TEOS-old SiO <sub>2</sub> :180/nm/min TEOS H3 (new):242 nm/min Si <sub>3</sub> N <sub>4</sub> -H <sub>2</sub> : 0.64 nm/min	242 nm/min -> 1um = 248 sec
20	Removal dicing foil	
21	<b>Clean HNO<sub>3</sub>-1 (#clean102)</b> NL-CLR-WB14 beaker 1: HNO <sub>3</sub> (99%) 5min	Standard cleaning
22	<b>Clean HN03-2 (#clean138)</b> NL-CLR-WB14 beaker 2 : HNO <sub>3</sub> (99%) 5min	
23	<b>Quick Dump Rinse (QDR)(#clean119)</b> NL-CLR-Wetbenches Rinse till the DI resistivity is > 10.5ΩM	
24	<b>Clean HNO<sub>3</sub>-3a/b(#clean118)</b> NL-CR-WB14 beaker 3a/b: HNO <sub>3</sub> (69%), temp 95°C, time > 10min	
25	<b>Quick Dump Rinse (QDR)(#clean119)</b> NL-CLR-Wetbenches Rinse till the DI resistivity is > 10.5ΩM	
26	<b>Substrate drying (#clean120)</b> NL-CLR-WB Single wafer dryer speed: 2500 rpm, 60 sec with 30 sec N <sub>2</sub> flow	
27	<b>Substrate rinsing/drying Semitool (#clean121)</b> NL-CLR-WetBenches Semitool spin rinser dryer	

28	<b>Litho furnace(#new)</b> NL-CLR- Temperature 85°C, time 16 hours (over night, use sign with Process running)	Use furnace for drying and evaporation of the water out of the channels. Procedure: start at 25 degrees with target temperature of 85 degrees. During the ramp up the fluid will evaporate. 16 hours
29.1	<b>Platinum lift-off flow</b>	Alternative for step 29-50
29.2	<b>Chamber clean by O2 plasma (Tetske) (#etch198)</b> NL-CLR-Tetske Select chamber for desired etch process Select electrode for desired etch process electrode temp.: 10°C pressure: 50 mTorr O2 gasflow: 50 sccm Power: 100 Watts Vdc: -600 Volts load: 65 ? Tune: 35 ? Time: 10 min Chamber is clean when plasma color is white	
30	<b>Plasma treatment for PT on SiRN (#etch172)</b> NL-CLR-Tetske Application: roughening of SiRN for Pt adhesion remarks: if silicon surface is exposed to plasma us a short etch time sputter directly after etching step Pt layer (maximum delay time 10 min) Dirty chamber Styros electrode Electrode : 10 °C SF <sub>6</sub> : 30 sccm O <sub>2</sub> : 5 sccm pressure: 40 mTorr <b>Power: 40 Watt</b> Time: 30 sec	
31	<b>Sputtering of Pt (#film118)</b> NL-CLR-nr. 37 / Sputterke Pt Target (gun #: see mis logbook) use Ar flow to adjust sputter pressure base pressure: < 1.0 e-6mbar sputter pressure: 6.6 e-3mbar power: 200W depositionrate = 22-27 nm/min	Use dummy 3. 200 nm = 480 sec, use dummy wafer for adherence of Pt layer (scotch-tape test)
32	<b>Priming (liquid)(#lith101)</b> NL-CLR-WB21/22 Primer: HexaMethylDiSilazane (HMDS) use spincoater: program: 4000 (4000rpm, 30sec)	
33	<b>Coating Olin Oir 907-17 (#lith105)</b> NL-CLR-WB21 Coating: Primus spinner olin oir 907-17 spin Program: 4000 (4000rpm, 30sec) Prebake: hotplate time 90 sec temp 95 °C	
34	<b>Alignment &amp; Exposure Olin OiR 907-17(#lith121)</b> NL-CLR-EV620 Electronic Vision Group EV620 Mask Aligner Hg-lamp: 12 mW/cm <sup>2</sup> Exposure Time: 4sec	Mask: front metal
35	<b>UV dicing foil (Adwill D-210)(#back104)</b> NI-CLR- Dicing foil Information: Thickness: 125um Material: 100um PET + 25um Acrylic (adhesive) Adhesion before UV: 2000 mN/25mm Adhesion after UV : 15 mN/25mm UV irradiation : Luminance > 120mW/cm <sup>2</sup> and Quality > 70mJ/cm <sup>2</sup> (wave length: 365nm)	Apply dicing foil on the backside of the wafer with roller on backside after bake of the next step
36	<b>Development Olin OiR resist(#lith111)</b> NL-CLR-WB21 After exposure Bake : hotplate time 60sec temp 120°C development: developer: OPD4262 time: 30sec in beaker 1 time: 15-30sec in beaker 2	
37	<b>Quick Dump Rinse (QDR)(#clean119)</b> NL-CLR-Wetbenches Rinse till the DI resistivity is > 10.5ΩM	
38	<b>Substrate drying (#clean120)</b> NL-CLR-WB Single wafer dryer speed: 2500 rpm, 60 sec with 30 sec N <sub>2</sub> flow	
38	<b>Substrate rinsing/drying Semitool (#clean121)</b> NL-CLR-WetBenches Semitool spin rinser dryer	
39	Remove dicing foil	
40	<b>Inspection by optical microscopic (#metro102)</b> NL-CLR- 6 microscopes olympus Microscope (4) leica Microscope (2)	Use dummy 1. Check profile, check wafer through etch

41	<b>Plasma etching of Pt (oxidation)(#etch173)</b> NL-CLR-Testke Application: oxidation of Pt <b>Do not use quartz electrode</b> styros electrode dirty chamber electrode temp.: 10°C 02: 20 sccm pressure: 10 mTorr <b>power: 32 Watt</b> time: 60 sec	Bias: 400Vdc
42	<b>Stripping resist in HNO<sub>3</sub> (99%) multipurpose (#lith194)</b> NL-CLR-WB-6 beaker : HNO <sub>3</sub> (99%) time: > 10 min, depends on the application	
43	<b>Quick Dump Rinse (QDR)(#clean119)</b> NL-CLR-Wetbenches Rinse till the DI resistivity is > 10.5ΩM	
44	<b>Substrate drying (#clean120)</b> NL-CLR-WB Single wafer dryer speed: 2500 rpm, 60 sec with 30 sec N <sub>2</sub> flow	
44	<b>Substrate rinsing/drying Semitool (#clean121)</b> NL-CLR-WetBenches Semitool spin rinser dryer	
45	<b>Inspection by optical microscopic (#metro102)</b> NL-CLR- 6 microscopes olympus Microscope (4) leica Microscope (2)	Use dummy 1. Check profile, check wafer through etch
46	<b>Etching of platinum (#etch152)</b> NL-CLR-WB10 Use private beaker for etching: HCl (32%) Selectipur, HNO <sub>3</sub> (69%) VLSI: H <sub>2</sub> O:HCl:HNO <sub>3</sub> (8:7:1) vol% (800 ml: 700ml:100ml) add HCl to H <sub>2</sub> O (when 60°C) add HNO <sub>3</sub> to mixture of H <sub>2</sub> O & HCl exothermic process! use stirrer temp.: 80°C (critical!) etchtime for 200nm : 4-6 minetchrate highly dependent on temperature of solution!!	Etch time: 4.5 min
47	<b>Quick Dump Rinse (QDR)(#clean119)</b> NL-CLR-Wetbenches Rinse till the DI resistivity is > 10.5ΩM	
48	<b>Substrate drying (#clean120)</b> NL-CLR-WB Single wafer dryer speed: 2500 rpm, 60 sec with 30 sec N <sub>2</sub> flow	
48	<b>Substrate rinsing/drying Semitool (#clean121)</b> NL-CLR-WetBenches Semitool spin rinser dryer	
49	<b>Inspection by optical microscopic (#metro102)</b> NL-CLR- 6 microscopes olympus Microscope (4) leica Microscope (2)	
50	<b>Surface profile measurement(#metro105)</b> NL-CLR-Veeco Dektak 8	Dummy 3 or 4. Measure Pt thickness.
51	<b>Litho furnace(#new)</b> NL-CLR- Temperature 85°C, time 16 hours (over night, use sign with Process running)	Use furnace for drying and evaporation of the water out of the channels. Procedure: start at 25 degrees with target temperature of 85 degrees. During the ramp up the fluid will evaporate. 16 hours
<b>Flow was tested until here, the coming section has still to be tested.</b>		
<b>Isolation of the core</b>		
52	<b>Dehydration bake(#lith102)</b> NL-CLR-WB21/22 dehydration bake at hotplate temp. 120°C time: 5min	Continue immediately with priming the step!
53	<b>Priming (liquid)(#lith101)</b> NL-CLR-WB21/22 Primer: Hexamethyldisilazane (HMDS) use spincoater: program: 4000 (4000rpm, 30sec)	
54	<b>Lithography - Coating Olin OiR 908-35(#lith106)</b> NL-CLR-WB21 Coating: Primus coater Olin OiR 908-35 Spin Program: 4000 (4000rpm, 30sec) Prebake: Hotplate Time 120s temp 95 °C	Use double layer of thick coating (2000RPM). Waiting time for evaporation before mask contact is required, info: Jeroen Haneveld
55	<b>Alignment &amp; Exposure Olin 908-35 (#lith122)</b> NL-CLR-EV620 Electronic Vision Group EV620 Mask Aligner Hg lamp: 12 mW/cm <sup>2</sup> Exposure Time: 9sec	Mask: front release SiRN
56	<b>UV dicing foil (Adwill D-210)(#back104)</b> NL-CLR- Dicing foil Information: Thickness: 125um Material: 100um PET + 25um Acrylic (adhesive) Adhesion before UV: 2000 mN/25mm Adhesion after UV : 15 mN/25mm UV irradiation : Luminance > 120mW/cm <sup>2</sup> and Quality > 70mJ/cm <sup>2</sup> (wave length: 365nm)	Apply dicing foil on the backside of the wafer with roller, apply after bake in next step



57	<b>Development Olin OiR resist(#lith111)</b> NL-CLR-WB21 After exposure Bake : hotplate time 60sec temp 120°C development: developer: OPD4262 time: 30sec in beaker 1 time: 15-30sec in beaker 2	
58	<b>Quick Dump Rinse (QDR)(#clean119)</b> NL-CLR-Wetbenches Rinse till the DI resistivity is > 10.5ΩM	
59	<b>Substrate drying (#clean120)</b> NL-CLR-WB Single wafer dryer speed: 2500 rpm, 60 sec with 30 sec N <sub>2</sub> flow	
59	<b>Substrate rinsing/drying Semitool (#clean121)</b> NL-CLR-WetBenches Semitool spin rinser dryer	
60	Removal dicing foil	
61	<b>Postbake Olin OiR resist(#lith109)</b> NL-CLR-WB21 postbake: Hotplate temp 120°C time 10min	
62	<b>Inspection by optical microscopic (#metro102)</b> NL-CLR- 6 microscopes olympus Microscope (4) leica Microscope (2)	Use dummy 1. Check profile, check wafer through etch
63	<b>Dupont MX 5020 foil for DRIE(#lith192)</b> NL-CLR- Material: Dupont MX5020 foil Application: wafer through etching using Adixen SE Procedure: applying MX5020 Start with the lithography process for etching mask remove plastic protection (has no color) from backside of the foil Apply the foil to the wafer with a roller Avoid air bubbles, retract the foil if bubbles are present Protect the photoresist mask with a blue tissue or bare silicon wafer during lami- nating Guide the wafer with foil by hand through the laminator, Temp 90°C, speed 2 Before DRIE etching remove the plastic protection foil! DRIE Adixen: Temperature range: -100°C up to 20 °C. Removal of MX5020 Start with O <sub>2</sub> plasma in Tepla 300 or 300E (metals are al- lowed) Continue with HN03 (99%) WB6 Use a piranha clean: private use (WB9)	Apply on backside of the wafer
64	<b>DRIE of multilayers (#etch174)</b> NL-CLR-Adixen SE Application: directional etch of SiRN or SiO <sub>2</sub> Nickname: "Roberts:" process <b>Parameters Value</b> Argon (sccm) 100 CHF <sub>3</sub> (sccm) 100 APC % 100 ICP (Watt) 1200 CCP (Watt) Rf 150 (Vde=580V) SH (mm) 200 Electrode temp. -100 +20 °C He (bar) 10 Etch rate OiR resist 160 nm/min Etch rate SiO <sub>2</sub> 250 nm/min Etch rate silicon 70-80 nm/min Etch rate SU-8 150 nm/min Etchrate SiRN 300 nm/min	Same etch time as in step 3
65	<b>DRIE of silicon SCT release(#etch176)</b> NL-CLR-Adixen AMS 100 SE Applications: release of SiRN channels (SCT) <b>Parameters Value</b> SF <sub>6</sub> [sccm] 350 He-backside cooling [mbar] 10 ICP [watt] 1400 -1800 CCP On/Off [msec] 0 p [Pa] 10 APC position % 15 Electrode temperature [°C] -100 Substrate height [mm] 200 Etch rate SiO <sub>2</sub> [μm/min] Etch rate Olin 907 [μm/min] Etchrate SU-8 Etch rate -Silicon (μm/min) Etch rate SiRN [nm/min] Channel release: 15 min 1800 Watt + 10 min 1400 Watt Add prestep for uniform etch : actiepunt Meint	This step or the next step as back-up. The etch rate is struc- ture and thermal conduction dependent!

66	<b>XeF2 SLE of polysilicon590(#etch189)</b> NL-CLR-Xactive etcher Always apply a pretreatment step to avoid extreme delay effects! Process for polysilicon590 layer: 1500 nm with an entrance hole of 10 um Pressure[Torr] Delay[cycles] Etchrate[um/cylce] CycleT[sec] 2 1.6 2.2 30 3 1.4 4.9 30 4 1.0 6.2 30 Ref: Christiaan Brunnink See also process report of Louis Visser	Back-up if the step before fails.
67 68	Removal MX5020 foil <b>Stripping of resist with acetone (#lith115)</b> NL-CLR-WB23 Spray methode start with technical acetone for 100% stripping time 60sec finish with VLSI isopropanol (IPA) spin drying visual microscopic inspection	Do not spin dry, fragile structures! MX5020 acetone resistant?
69	<b>Clean substrate by drying in air(#clean125)</b> NL-CLR-Wetbench 11 right side beaker IPA VLSI, time 10 min Substrate drying by air in wet bench	
70	<b>Etching SiO2 BHF (1:7)(#etch125)</b> NL-CLR-WB9 or 10 Use private beaker with BHF (1:7) temp.: 20°C Etchrates: thermal SiO2: 60-80nm/min PECVD SiO2: 125/nm/min TEOS SiO2: 180/nm/min TEOS H3 (new): 242 nm/min Pyrex #7740: 20nm/min Borofloat BF33: 20-25 nm/min Si3N4-H2: 0.64 nm/min	Layer thickness step 17. 242 nm/min -> 1um = 248 sec
71	<b>Clean by waterbrush(#clean127)</b> NL-CLR-Wetbenches spray substrate, time 2min both sides	
72	<b>Clean substrate by drying in air(#clean125)</b> NL-CLR-Wetbench 11 right side beaker IPA VLSI, time 10 min Substrate drying by air in wet bench	
73	<b>Litho furnace(#new)</b> NL-CLR- Temperature 85°C, time 16 hours (over night, use sign with Process running)	Use furnace for drying and evaporation of the water out of the channels. Procedure: start at 25 degrees with target temperature of 85 degrees. During the ramp up the fluid will evaporate. 16 hours
74	Breaking the chips apart	

## C.2 Wafer allocation

Step	process	Wafer ID												Remarks
		P1	P2	P3	P4	P5	P6	D1	D2	D3	D4	D5	D6	
11	SiRN deposition	X	X	X	X	X	X	X	X	X	X	X	X	
14	SU-8 with Mask access-holes	X	X	X	X	X	X	X	X	X	X	X	X	
23	DRIE back etch	X	X	X	X	X	X	X	X	X	X	X	X	Check etch profile by breaking of D1-3
36	TEOS deposition	X	X	X	X	X	X				X	X	X	Check layer thickness and test etchrate on D4
62	Cr sputtering	X	X	X		X	X				X	X	X	
63	OiR with Mask channel	X	X			X	X				X	X		Check slit width on all
73	Etch Cr	X	X			X	X				X	X		
79	DRIE channel	X	X			X	X				X	X		Check the channel definition by breaking D5
81	Cr etch/TEOS strip	X	X			X	X				X			
97	LPCVD SiRN	X	X			X	X				X			Check closure of channel and layer thickness
1	MX5020 with Mask KOH	X	X			X	X				X			Introduce extra SiRN dummies in the process
3	DRIE SiRN	X	X			X	X				X			
7	KOH etch	X	X			X	X				X			Check the etch width and grooves
17	TEOS deposition	X	X			X	X				X			
19	TEOS strip frontside	X	X			X	X				X			
29	Roughning SiRN	X	X			X	X				X			
31	Sputtering Pt	X	X			X	X				X			Check layer adhesion with scotch-tape
34	OiR with mask Front Metal	X	X			X	X				X			
41	Pt oxidation	X	X			X	X				X			
46	Pt etch	X	X			X	X				X			Check Pt thickness
55	OiR with mask Front SiRN	X	X			X	X				X			
64	DRIE SiRN	X	X			X	X				X			
65	DRIE isotropic Si	X	X			X	X				X			Test release process
70	TEOS stripping	X	X			X	X				X			
74	Breaking the chips	X	X			X	X				X			Do dummies first

**Figure C.1:** The usage of the wafers during the processing. Green means used for measurement and red means destroyed during processing.



## Appendix D

# Set-up blueprints

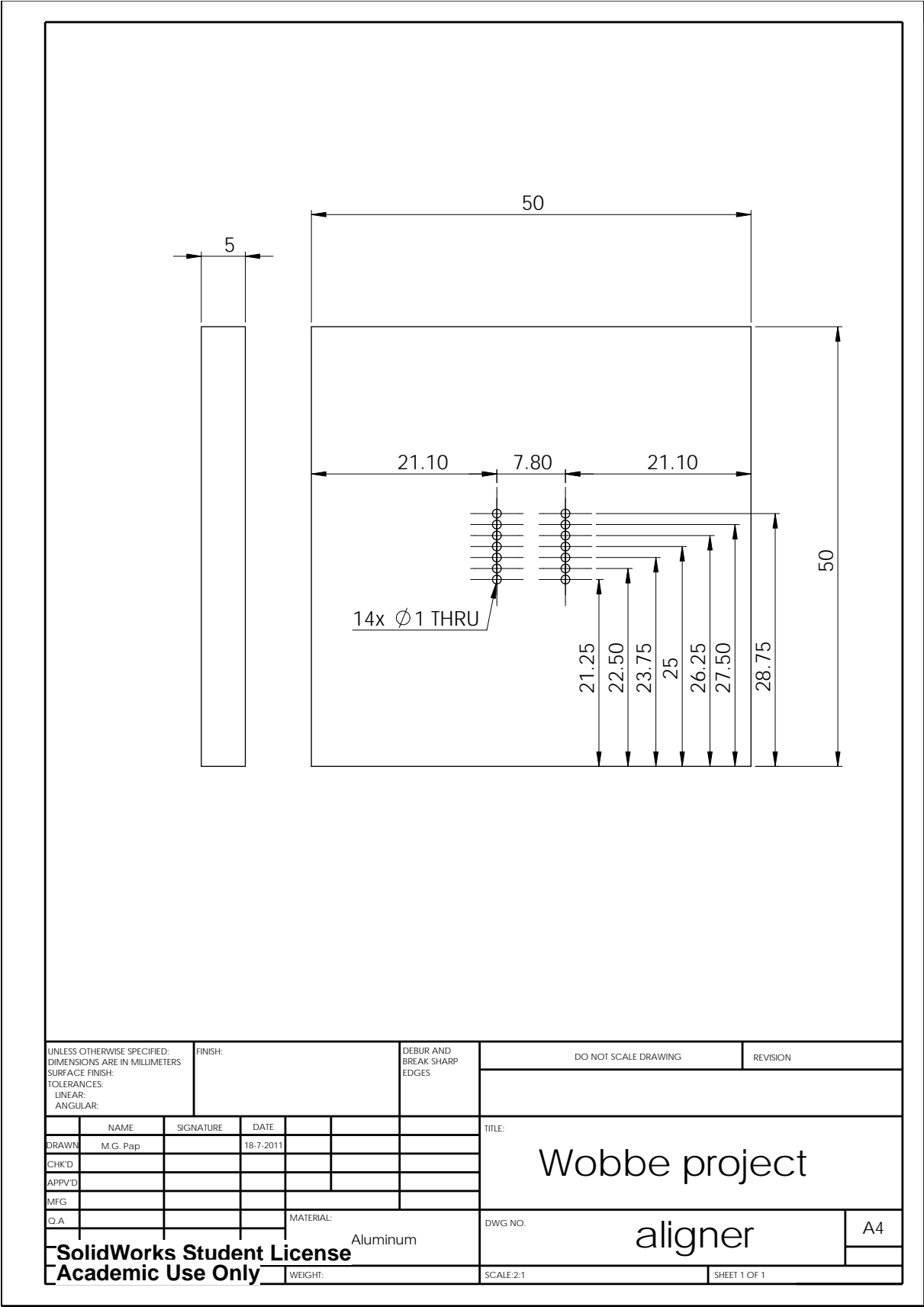


Figure D.1: The pin aligner block

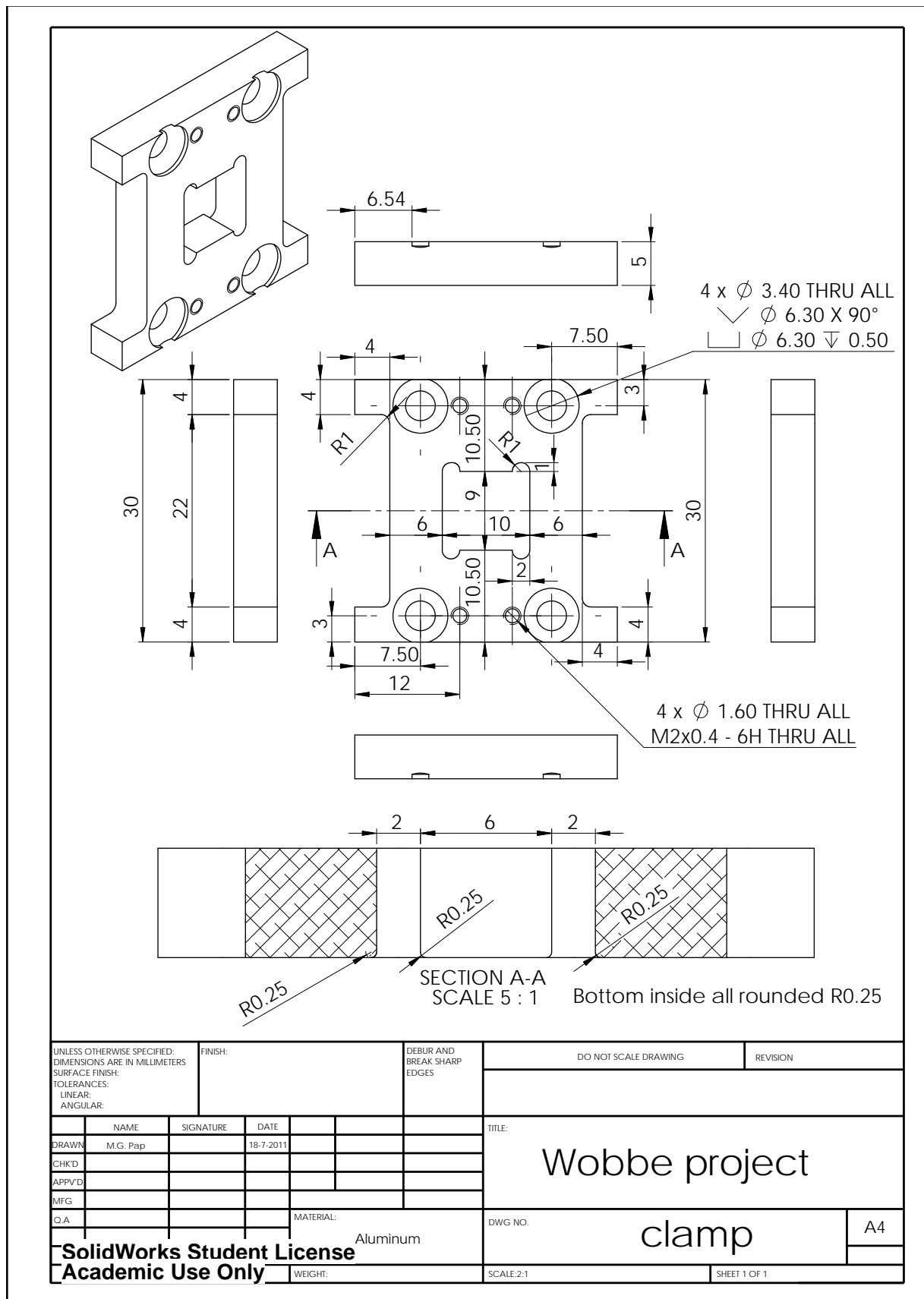


Figure D.2: The holder clamp

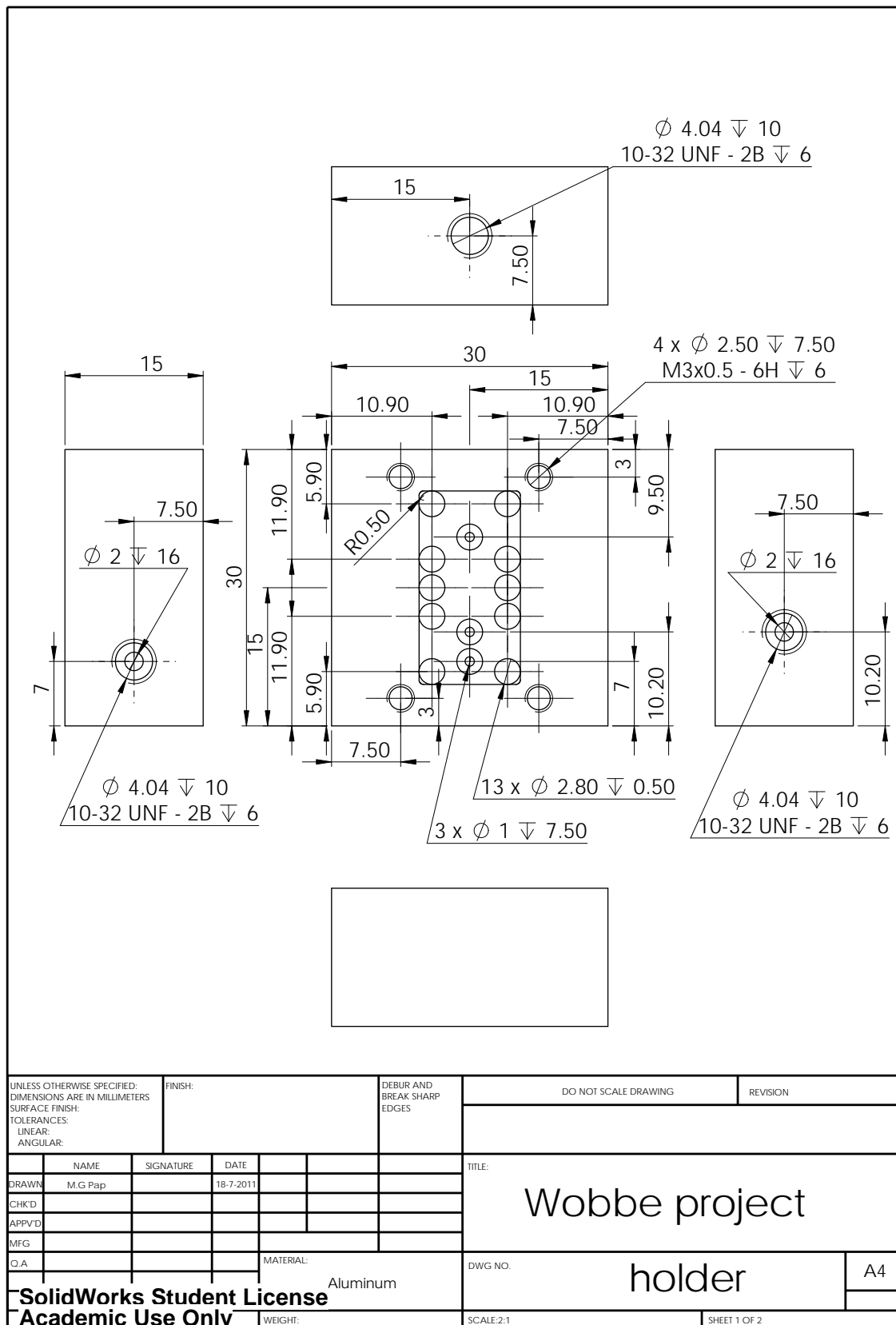


Figure D.3: The chip holder



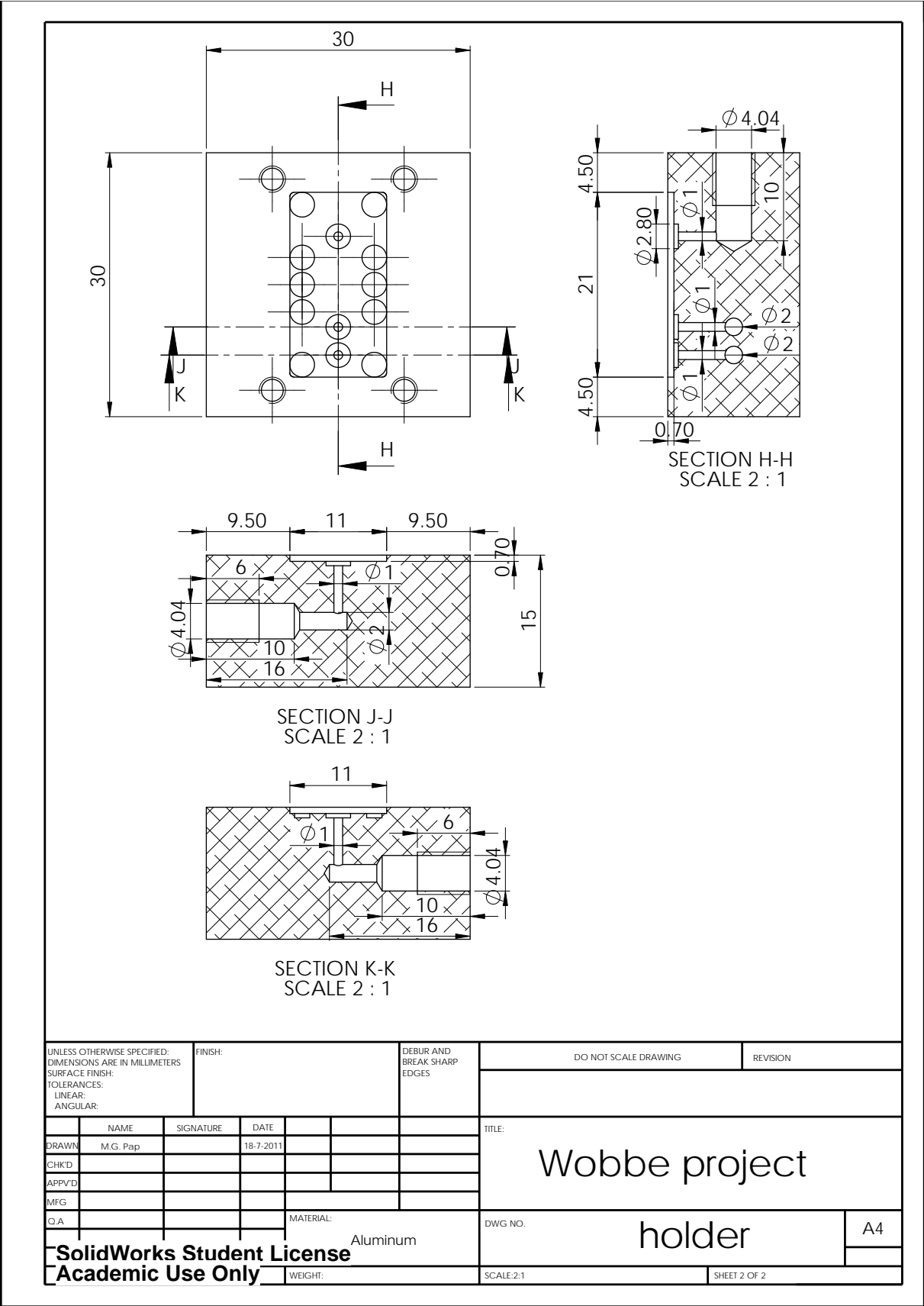


Figure D.4: The cross-sectional view of the chip holder

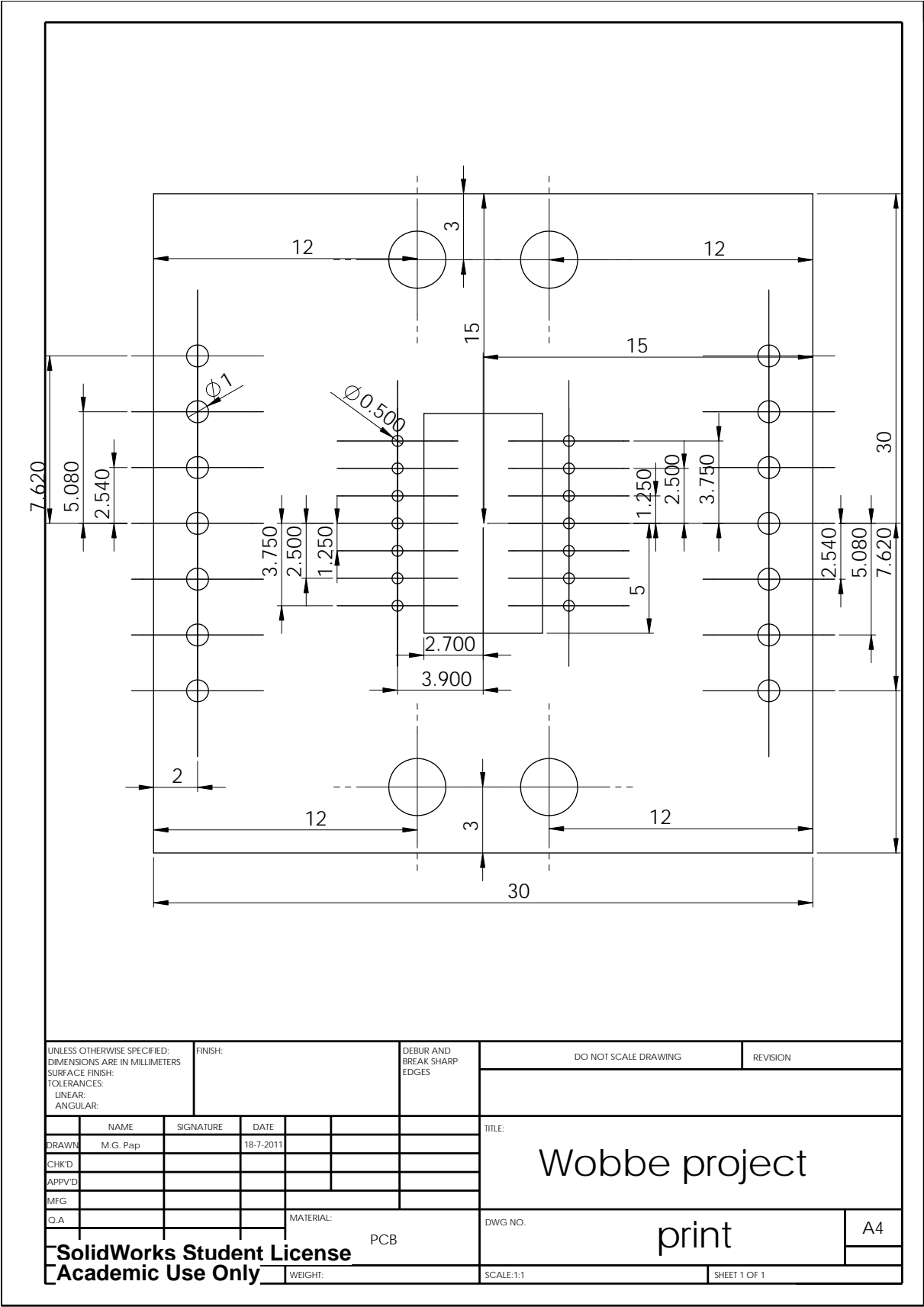


Figure D.5: The contact print.pdf

# Bibliography

- [1] Hemminger and Höhne, *Calorimetry: Fundamentals and Practice*. Verlag Chemie GmbH, 1984.
- [2] P. Ulbig and D. Hoburg, "Determination of the calorific value of natural gas by different methods," *Thermochimica Acta*, vol. 382, pp. 27–35, 2002.
- [3] H. instruments bv, "Wobbe-index meter." <http://www.hobre.com/images/stories/pdf/wim9900-incl-sg-cell.pdf>.
- [4] M. Hoppe, P. Schley, and M. Uhrig, "Metrological issues in energy measurement on biogas," *Accred Qual Assur*, vol. 14, pp. 677–683, 2009.
- [5] I. Schoemaker, "Aanvullende voorwaarden rnb groen gas invoeders." [http://www.enexis.nl/site/Images/voorlopige\\_aanvullende\\_voorwaarden\\_RNB\\_Groen\\_Gas\\_Invoeders\\_v14%5B1%5D.pdf](http://www.enexis.nl/site/Images/voorlopige_aanvullende_voorwaarden_RNB_Groen_Gas_Invoeders_v14%5B1%5D.pdf).
- [6] J. Haneveld, T. S. J. Lammerink, M. J. de Boer, R. G. P. Sanders, A. Mehendale, J. C. Lötters, M. A. Dijkstra, and R. J. Wiegerink, "Modeling, design, fabrication and characterization of a micro coriolis mass flow sensor," *Journal of micromechanics and microengineering*, vol. 20, p. 125001, September 2010.
- [7] International Organization for standardization, "Natural gas - calculation of calorific values, density, relative density and wobbe index from composition," *ISO 6976:1995/Cor.3:1999(E)*, 1999.
- [8] International Organization for standardization, "Natural gas - measurement of properties - calorific value and wobbe index," *ISO15971:2008*, 2008.
- [9] D. D. Systems, "Advanced bomb calorimeters." <http://cal2k.com>.
- [10] Preston. <http://abundantbrain.com/wp-content/uploads/2010/05/bombcal.jpg>, 2010.
- [11] Y. Aleksandrov *Thermochimica Acta*, vol. 382, 2002.
- [12] R. institute of petroleum industry, "Methane steam reforming." <http://www.ripi.ir/index.php?option=content&task=view&id=205>.
- [13] M. Barnes. [http://media.noria.com/sites/archive\\_images/backup\\_200207\\_GasChroma-Fig2.jpg](http://media.noria.com/sites/archive_images/backup_200207_GasChroma-Fig2.jpg), 2002.
- [14] Sommers et al., "Process and apparatus for the combustionless measurement and/or control of the amount of heat fed to gas consumption devices." US 4,384,792, May 1983.
- [15] Hammond et al., "Measurement of a gas characteristic." US 5,635,626, June 1997.
- [16] Froelich et al., "Device and method for directly measuring calorific energy contained in a fuel gas." US 6,536,946 B1, March 2003.
- [17] Cordier et al., "Method and device for evaluating a fuel gas wobbe index." US 6,893,152 B2, May 2005.
- [18] Ryser et al., "Gas viscosity sensor." US 7,730,766 B2, June 2010.
- [19] Thurston et al., "Method and apparatus for measuring the calorific value of a gas." US 6,442,996 B1, September 2002.
- [20] Driftmeier, "Method and apparatus for the measurement of the interchangeability of lpg/air mixtures with natural gas." US 6,539,775 B1, April 2003.
- [21] C. Slater, T. Maeder, and P. Ryser, "Portable ltcc gas viscometer for determining wobbe number," *Procedia Engineering*, vol. 5, pp. 307–310, 2010.
- [22] Haruta, "Combustion property of gas measuring apparatus." US 4,246,773, January 1981.
- [23] Hammond et al., "Apparatus for measuring a gas value." US 6,047,589, April 2000.
- [24] Van Wesenbeeck et al., "Method for measuring the quantity of heat present in fuel gas." US 6,446,487 B1, September 2002.
- [25] Hammond et al., "Measuring energy consumption." US 6,517,237 B1, Februari 2003.
- [26] K. Loubar, C. Rahmouni, O. L. Corre, and M. Tazrout, "A combustionless determination method for combustion properties of natural gases," *Fuel: The Science and Technology of Fuel and Energy*, vol. 86, pp. 2535–2544, 2007.
- [27] C. Rahmouni, O. L. Corre, and M. Tazrout, "Determination of the combustion properties of natural gases by pseudo-constituents," *Fuel: The Science and Technology of Fuel and Energy*, vol. 82, pp. 1399–1409, 2003.

- 
- [28] M. Jaeschke, "Thermodynamic research improves energy measurement of natural gas," *Thermochimica Acta*, vol. 382, pp. 37–45, 2002.
- [29] Ohata et al., "Apparatus for measuring calorific power of hydrocarbon compounds." US 3,934,139, January 1976.
- [30] Schley, "Method and device for determining the gas properties of a combustible gas." US 2002/0040590 A1, April 2002.
- [31] Antel et al., "Method, sensor and system for measuring lower heating value and wobble index of gaseous fuel." US 2007/0089485 A1, april 2007.
- [32] Knobloch et al., "Wobbe index sensor system." US 2009/000013759 A1, January 2009.
- [33] Hörnemann, "Method for determining the calorific value of a gas and/or the wobble index of a natural gas." US 5,807,749, September 1998.
- [34] Philippe, "Evaluation and regulation of the thermal power of a flow combustible gas; characterization of a thermal mass flowmeter." US 6,371,147 B1, April 2002.
- [35] Rahmouni et al., "Method for determining at least one energetic property of a gas fuel mixture by measuring physical properties of the gas mixture." US 7,091,509 B2, August 2006.
- [36] S. Udina, M. Carmona, G. Carles, J. Santander, L. Fonseca, and S. Marco, "A micromachined thermoelectric sensor for natural gas analysis: Thermal model and experimental results," *Sensors and Actuators B: Chemical*, vol. 134, pp. 551–558, 2008.
- [37] L. Dorojkine, "The non-catalytic thermal wave-based chemical gas sensor for methane and natural gas," *Sensor and Actuators B*, vol. 89, pp. 76–85, 2003.
- [38] J. Coulson and J. Richardson, *Chemical engineering 4th ed.*, vol. 1. Pergamon Press, 1990.
- [39] A. Humphreys, "Some thermophysical properties of components of natural gas and cognate fluids," *Groupe Européen de Recherches Gazières, Tech. Monograph*, no. GERG TPC/1, p. 43, 1986.
- [40] J. Hirschfelder, C. Curtiss, and R. Bird, *Molecular theory of gases and liquids*. John Wiley and Sons, INC., 1967.
- [41] dr. ir. P.C. Breedveld and prof dr. ir. J van Amerongen, *Dynamic systems: modelling and simulation with bondgraphs*. Open Universiteit, 2003.
- [42] T. Poinot and D. Veynante, *Theoretical and Numerical Combustion. Second Edition*. Edwards, 2005.
- [43] M. Pap, "Modelling of silicon nitride hairs," *Individual Research Assignment (IOO)*, 2010.
- [44] N. Environnement, "Biogas composition." [http://www.biogas-renewable-energy.info/biogas\\_composition.html](http://www.biogas-renewable-energy.info/biogas_composition.html).
- [45] U. D. of energy, "Hebeler corporation cng/lng composition." [http://www1.eere.energy.gov/cleancities/pdfs/hebeler\\_remote\\_gas\\_ngvtf\\_albany.pdf](http://www1.eere.energy.gov/cleancities/pdfs/hebeler_remote_gas_ngvtf_albany.pdf).
- [46] L. G. B. B.V., "Methane 2.5 chemical." <https://customer.linde.com/FIRSTspiritWeb/linde/LGNL/media/datasheets/EN-PIB-0327.pdf>.
- [47] G. P. Smith, D. M. Golden, M. Frenklach, N. W. Moriarty, B. Eiteneer, M. Goldenberg, C. T. Bowman, R. K. Hanson, S. Song, W. C. Gardiner, V. L. Jr., and Z. Qin, "Griem 3.0." <http://www.me.berkeley.edu/gri-mech/>.
- [48] J. Aguillon, "Calorimeter of the continuous and recording type for determining the calorific power of fluid combustibles," *Patent 1,435,783 Paris, France*, 1922.
- [49] N.-T. Nguyen and Z. Wu, "Micromixers a review," *Journal Micromechanical Microengineering*, vol. 15, pp. R1Ū–R16, 2005.
- [50] A. A. S. Bhagat, E. T. K. Peterson, and I. Papautsky, "A passive planar micromixer with obstructions for mixing at low reynolds numbers," *Journal Micromechanical Microengineering*, vol. 17, pp. 1017Ū–1024, 2007.
- [51] A. J. Chapman, *Heat transfer, third edition*. Collier Macmillan Publisher, 1974.
- [52] J. Spannhake, O. Schulz, A. Helwig, A. Krenkow, G. M. 1, and T. Doll, "High-temperature mems heater platforms: Long-term performance of metal and semiconductor heater materials," *Sensors*, vol. 6, pp. 405–419, 2006.
- [53] K.-N. Lee1, D.-S. Lee, S.-W. Jung, Y.-H. Jang, Y.-K. Kim, and W.-K. Seong, "A high-temperature mems heater using suspended silicon structures," *J. Micromech. Microeng.*, vol. 19, 2009.
- [54] R. Tiggelaar, *Silicon-technology based microreactors for high-temperature heterogeneous partial oxidation reactions*, Ph.D. thesis, University of Twente. Wöhrmann Print Service, Zutphen, The Netherlands, 2004.
- [55] R. M. Tiggelaar, J. W. Berenschot, J. H. de Boer, R. G. P. Sanders, J. G. E. Gardeniers, R. E. Oosterbroek, A. van den Berg, and M. C. Elwenspoek, "Fabrication and characterization of high-temperature microreactors with thin film heater and sensor patterns in silicon nitride tubes," *Lab Chip*, vol. 5, pp. 326–Ū336, 2005.
- [56] R. Tiggelaar, R. Sanders, A. Groenland, and J. Gardeniers, "Stability of thin platinum films implemented in high-temperature microdevices," *Sensors and Actuators A: Physical*, vol. 152, pp. 39–Ū47, 2009.
- [57] A. Gao, *Influence of nanoscale surface roughness on flow behaviour in fluidic microchannels*. University of Twente, Master thesis Nanotechnology, 2009–2010.
- [58] M. Vangbo and Y. Bäklund, "Precise mask alignment to the crystallographic orientation of silicon wafers using wet anisotropic etching," *Journal Micromechanical Microengineering*, vol. 6, pp. 279–284, 1996.
-